Optimized Human Head Array Design for 10.5T MRI

A THESIS
SUBMITTED TO THE FACULTY OF THE
UNIVERSITY OF MINNESOTA
BY

Myung Kyun Woo

IN PARTIAL FULFILLMENT OF THE
REQUIERMENTS
FOR THE DEGREE OF
DOCTOR OF PHOLOPSPHY

Prof. Dr. Kamil Ugurbil

Prof. Dr. Gregor Adriany

October 2020

Table of Contents

1. **Introduction**
   - 1.1 Physical principles of magnetic resonance imaging (MRI) · · · · · · · · · · · · ·
   - 1.2 Main magnet and Gradient coil ·
   - 1.3 Radiofrequency (RF) coil ·
   - 1.4 Radiative antenna for ultra-high-field (UHF) MRI ·
   - 1.5 High dielectric constant (HDC) materials for MR applications · · · · · · · · · ·
   - 1.6 Objective and Overview of this thesis ·
   - 1.7 References ·

2. **A 16-channel transceiver loop + dipole antennas head array for human head imaging at 10.5T**
   - 2.1 Introduction ·
   - 2.2 Methods ·
   - 2.3 Results ·
   - 2.4 Discussions ·
   - 2.5 Conclusions ·
   - 2.6 References ·

3. **Interleaved ^{31}P MRS imaging of human frontal and occipital lobes using dual RF coils in combination with single-channel transmitter–receiver and dynamic B_0 shimming**
   - 3.1 Introduction ·
   - 3.2 Methods ·
   - 3.3 Results ·
   - 3.4 Discussions ·
   - 3.5 Conclusions ·
   - 3.6 References ·

4. **Comparison of 16-channel human head mono-dipole arrays vs. 16-channel monopole + HDC dipole arrays (8-channel monopole arrays + 8-channel HDC dipole arrays) at 10.5T**
   - 4.1 Introduction ·
   - 4.2 Methods ·
   - 4.3 Results and Discussions· ·
   - 4.4 Conclusions ·
   - 4.5 References ·

5. **Improved B_1^+ efficiency of a dipole antenna equipped with high HDC materials at 10.5T**
    - 5.1 Introduction
    - 5.2 Methods
    - 5.3 Results and Discussions
    - 5.4 Conclusions
    - 5.5 References

6. **Floating asymmetric sleeve antenna array for magnetic resonance imaging**
    - 6.1 Introduction
    - 6.2 Methods
    - 6.3 Results
    - 6.4 Discussions
    - 6.5 Conclusions
    - 6.6 References

7. **Summary and General discussions**
    - 7.1 Summary
    - 7.2 General discussions

8. **Publications and Awards**

9. **Acknowledgements**

10. **Curriculum vitae**

11. **References**

Chapter 1. Introduction

1.1. Physical principles of magnetic resonance imaging (MRI)

1.2. Main magnet and Gradient coil

1.3. Radiofrequency (RF) coil
- 1.3.1 Transceiver coil and transmit and receive (T/R) switch
- 1.3.2 Transmit-only Receive-only (TORO) coil
- 1.3.3 S-parameters and decoupling technique for tuning a RF coil
- 1.3.4 Resonant frequency (ω_r) and quality (Q) factor

1.4. Radiative antenna for ultra-high-field (UHF) MRI

1.5. High dielectric constant (HDC) materials for MR applications

1.6. Objective and Overview of this thesis

1.7. References

Introduction

1.1 Physical principles of magnetic resonance imaging (MRI)

MRI is based on nuclear magnetic resonance (NMR) that was originally discovered by Bloch [24] and Purcell [25] in 1946. The present form of the MRI was introduced in the early 1970s by Lauterbur [26,27]. He proposed the use of gradients to distinguish between spatially localized signals. This technique, which can encode spatial information, led to the development of MRI as a medical device. In the mid 1970's, Richard Ernst [28,29] applied a 2D Fourier transform to the reconstruction of MR images. This method is a representative algorithm that is now used for MRI.

MRI is used in the clinic to diagnose and discover anatomical structures and physiological principles. The advantage of MRI is that it is a non-invasive imaging technique and therefore has an important role as a medical instrument. Unlike some other imaging modalities like x-rays and CTs, MRI does not require that the subject be exposed to ionizing radiation. MRI also provides more information than other imaging modalities with sensitive soft tissue contrast.

MRI is based on the quantum mechanical property of nuclear spin such as ^{1}H, ^{13}C, ^{19}F, ^{23}Na, and ^{31}P. This non-zero spin acts as a magnetic moment. The proton (^{1}H) is the default nuclear spin which has a 42.576 MHz/T gyromagnetic ratio for MRI. When spins are placed in an external magnetic field, they precess around an axis along the direction of the magnetic field. The relation between the external magnetic field and the Larmor precession frequency is given by:

$$\omega_0 = \Upsilon B_0 \tag{1.1}$$

where ω_0 is the Larmor frequency, Υ is the gyromagnetic ratio, and B_0 is the external magnetic field. Precession is described by the Bloch Equation, which is given as

$$\frac{dM_x(t)}{dt} = \Upsilon(M(t) \times B(t))_x - \frac{M_x(t)}{T_2} \tag{1.2}$$

$$\frac{dM_y(t)}{dt} = \Upsilon(M(t) \times B(t))_y - \frac{M_y(t)}{T_2} \tag{1.3}$$

$$\frac{dM_z(t)}{dt} = \Upsilon(M(t) \times B(t))_z - \frac{M_z(t) - M_0}{T_1} \tag{1.4}$$

where M_x, M_y, and M_z are vector components of the magnetization (M), T_1 is the longitudinal relaxation time, and T_2 is the transverse relaxation time. B (t) is composed of B_0 and B_1. The external magnetic field (B_0) generates precession of magnetization. The

B_1 field generated by RF coils creates a spin state to emit an MR signal. It also can be described as magnetized spins of a lower energy state being excited to a high energy state. After applying the B_1 field, the longitudinal component (M_z) recovers with the time constant T_1, and the transverse component (M_x and M_y) decays with the time constant T_2. The relaxation times T_1 and T_2 create various contrasts between the soft tissues with the MR sequence parameters.

1.2 Main magnet and Gradient coil

Three types of magnets are used for MRIs: permanent, electromagnetic and superconducting magnets. The permanent magnet is generally used for low tesla (<1 T) MRI and the superconducting magnet is used for high tesla (>1T) MRI. The superconducting magnet (figure 1a) can be equipped for high field strength from 1 T to beyond 11.7 T depending on the materials that are used in the construction of the magnet. Only a few superconducting materials such as niobium-titanium (NbTi), niobium-tin (Nb_3Sn) alloy and magnesium diboride (MgB_2) can be used to construct a superconducting magnet. The electrical current can flow without resistance after the magnet reaches a superconducting state. To maintain the system in a cooled state, this material needs to be maintained at a temperature of 4 K (-269 ˚C). Although superconducting magnets have high maintenance costs because expensive helium is used for cooling, the superconducting magnet is still the preferred type of instrumentation. As shown in figure 1b, a new technology for magnets has been developed in attempts to improve the economic benefit of such systems. MRIs with superconducting magnets provide extremely advanced SNR performance compared to the other magnet types that are used in MRI. For clinical usage and research, high-resolution imaging based on high SNR is very important in terms of reaching a precise diagnosis of a patient.

Three gradient coils are used to generate gradient fields in the x-, y-, and z-direction of the MRI scanner. Gradient coils encode spatial information, and provide three types of encoding which are slice selection encoding, phase encoding, and frequency encoding. The performance of a specialized imaging technique such as diffusion tensor imaging (DTI) and tractography can be highly affected by the performance of the gradient coil, such as the slew rate.

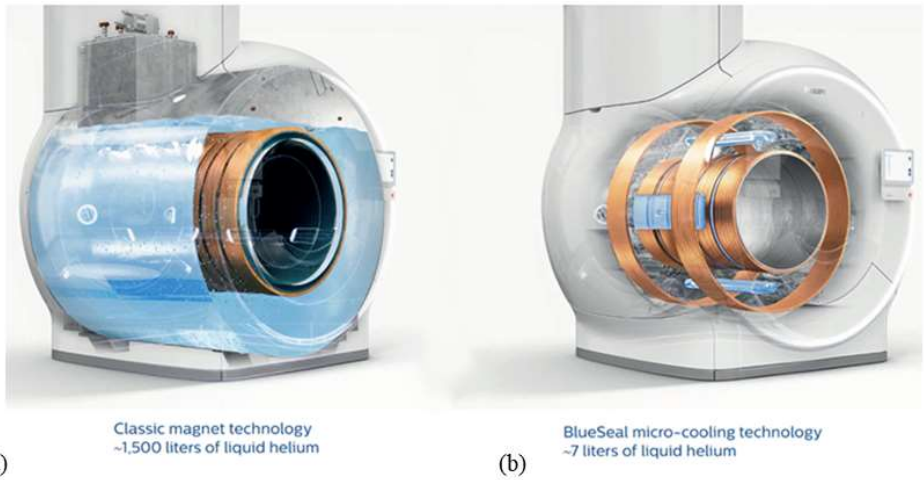

Figure 1. Classic magnet (a) and newly developed helium-free magnet by Phillips (b). (Image source: https://www.usa. philips.com/healthcare)

1.3 Radiofrequency (RF) coil

RF coils are essential components of MRI. The role of RF coils is to transmit and receive signals between the MRI system and the subject being imaged. To obtain high quality images, a uniform B_1 field and a high SNR are highly desired with RF coils. Specifically for transmitter coils, a uniform B_1^+ field with a high B_1^+ efficiency is strongly preferred for uniform imaging. For receiver coils, a high SNR with a high sensitivity is essential for efficiently acquiring the RF signal. In addition, the issue of the safety of RF coils must be considered in the design of RF coils.

Generally, RF coils can be classified into two types depending on the shape of the RF coils and current flowing in these coils. The first type of coil is a volume coil (figure 2a) such as a slotted tube resonator (STR), a Helmholtz coil and a birdcage coil. Birdcage coils are generally used for a transmitter coil based on a uniform B_1^+ field over a large volume of samples with a high B_1^+ efficiency as shown in figure 2b. These coils can be used for receiver coil depending on the application.

The other type of coil is a surface coil (figure 2c) which can be configured as a single or an array structure. Generally, the surface coil, which can be positioned close to the subject, shows a high SNR as shown in figure 2d. However, the surface coil has certain limitations including a shorter penetration depth for UHF. In chapters 2 through 6, this thesis provides information on the innovative development of surface coils with the goal of improving shortness at 10.5 T.

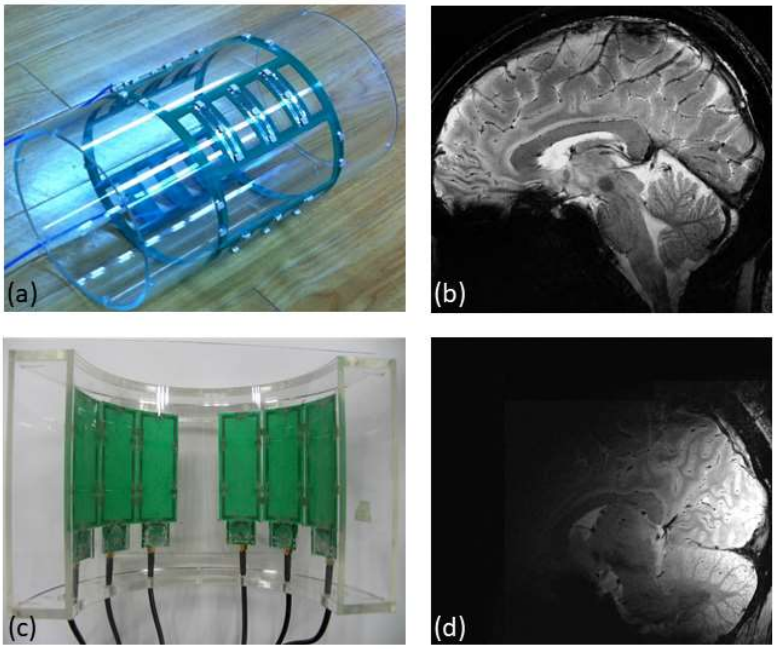

Figure 2. Photos of RF coils ((a) and (c)) corresponding images ((b) and (d)) of a human head coil at 7 T. A volume coil (a) and a surface array coil (c)

1.3.1 Transceiver coil and the transmit and receive (T/R) switch

RF coils can be divided into three fundamental types: transmitters, receivers and transceivers, “Transmitter” coils are tuned at a specific target Lamor frequency to excite nuclei on resonance. In MR experiments, this initial spin excitation is immediately followed by the reception of an MR signal during which the “receiver” coils pick up RF signals that are emitted by the nuclei at the resonant frequency. The magnetic field of the RF pulse generated by the transmit coils is referred to as the “B_1” field in the MR literature. The direction of the B_1 field is perpendicular to the direction of the main magnetic field which is called the “B_0” field. When the RF coils are applied for signal transmission and reception, such an RF coil which has the roles of both a transmitter and a receiver, this arrangement is called a “transceiver”. In the case, there is no interaction between a transmitter coil and a receiver coil for the transceiver coil. Since they have advantages in UHF applications in which a multi-channel transmit system is used, they are ideal antenna structures and this terminology will be used throughout this thesis.

Transceiver coils are operated with transmit and receive (T/R) switch circuitries that are in close proximity to one another, to allow the required separation between the high-power RF signal transmission and the reception. To utilize transceiver coils, T/R switches are essential parts for controlling the path between the RF power amplifier and the preamplifier. When T/R switches are functioning in the transmitting and receiving mode, a coil can be connected to RF power amplifiers as the transmitting mode and connected to preamplifiers as the receiving mode, respectively. A home-built T/R switch is shown in figure 3a. The T/R switch is composed of multiple PIN diodes and a low-pass filter, as shown in figure 3b. The isolation between transmitting and receiving mode usually be required to be below -40 dB to reduce the correlation between transmission and reception.

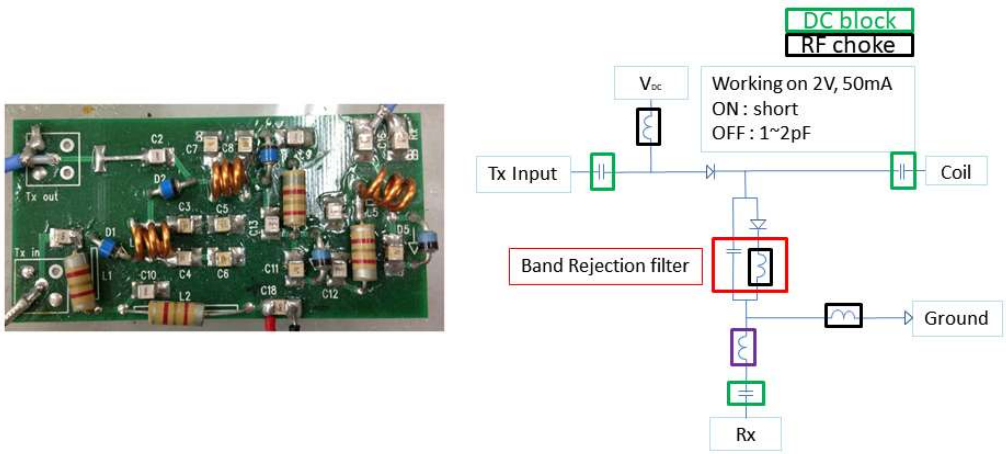

(a) (b)

Figure 3. A photo (a) and a schema (b) of a T/R switch

Figure 4 shows various types of the transceiver coils at 7 T [30]. A hybrid birdcage coil (figure 4a), a 4-channel capacitive decoupled loop coil (figure 4b), a 4-channel overlapped decoupled loop coil (figure 4c), a 6-channel overlapped decoupled loop coil (figure 4d) and a 8-channel overlapped decoupled loop coil (figure 4e) are shown. From figure 4a to 4e, the hybrid birdcage (figure 4a) is the only volume coil among those.

As indicated the matching circuit in figure 4a and 4b, the transceiver coils are generally tuned to 50 Ω matching in the smith chart. Transceiver coils are connected to 50 Ω systems (power amp and receiver system) using 50 Ω coaxial cables. The tuning of transceiver coils can change dramatically depending on the size and geometry of the coil as well as the object that is loaded.

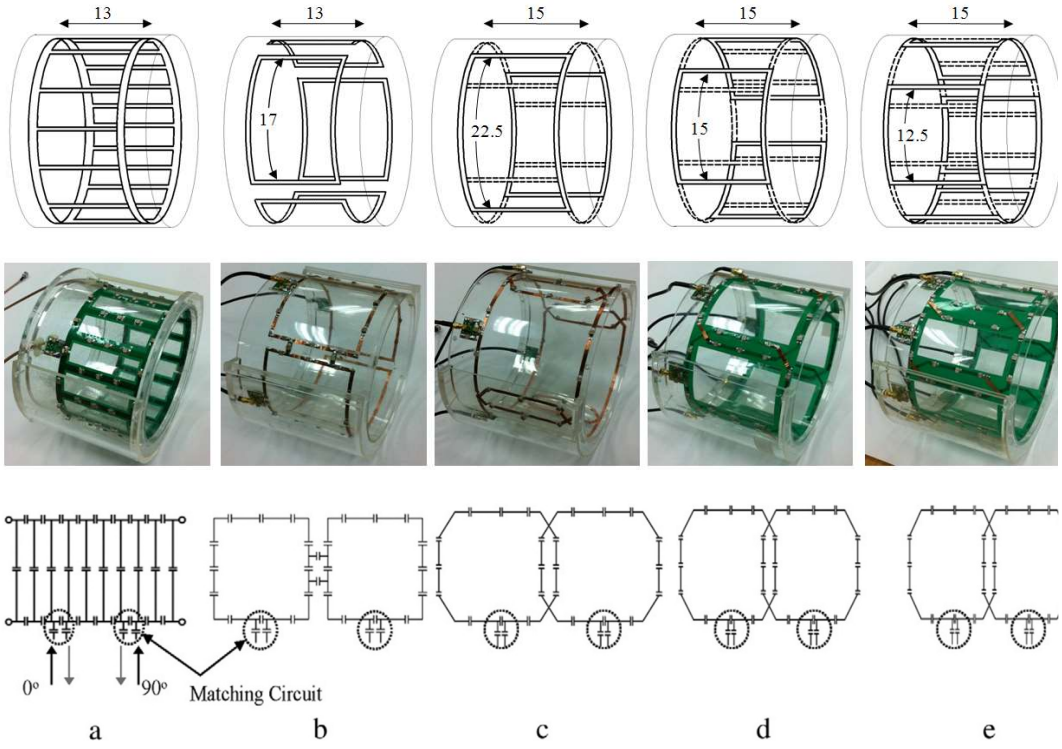

Figure 4. Photos and schema of transceiver coils for a human head coil at 7 T. The hybrid birdcage (a), the 4-channel capacitive decoupled loop coil (b), the 4-channel overlapped decoupled loop coil (c), the 6-channel overlapped decoupled loop coil and the 8-channel overlapped decoupled loop coil.

1.3.2 Transmit-only Receive-only (TORO) coil

The transmit-only Receive-only (TORO) coil is an RF coil type which is configured by a separate transmitter coil and a separate receiver coil [31]. This type of coil is used to maximize the SNR by setting a receiver coil close to the sample and to reduce SAR by setting a transmitter coil relatively further from the sample. To set up these two RF coils in parallel to the sample, transmitter coils are typically detuned during the reception so as to have minimal interaction.

As shown in figure 5, the receiver coil contains a bridge balanced to unbalanced (balun) matching network, which is generally composed of a capacitor, an inductor, and a PIN diode. When the PIN diode is turned on by a bias, an inductor and a capacitor are used to configure the tank circuit to block the RF signal within a certain targeted frequency. The major role of detuning the circuit is to minimize the degree of interference between a transmitter coil and a receiver coil. However, even if a detuning circuit is utilized, a small interaction between the transmitter coil and the receiver coil are still possible. This interaction between the transmitter coil and the receiver coil can then affect the B_1^+ efficiency or change the shape of the B_1^+ field of the transmitter coil.

Overlapped loop coils or gapped loop coils are generally used as a decoupling technique among multiple elements in a receiver coil array. The overlapped loop coil can minimize the extent of coupling between the nearest neighbors by minimizing the electrical current between adjacent coils. Figure 6 shows the optimal distance for the overlapping decoupling technique between two elements (figure 6a) and a multiple 2D array structure (figure 6b) [32]. For the gapped loop coils, the distance between elements can reduce the coupling between them. However, it can cause some null imaging areas

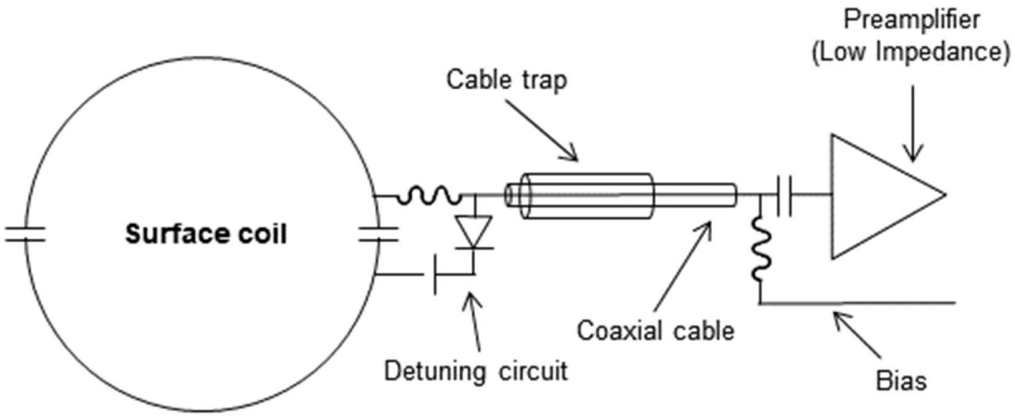

Figure 5. Schema of a surface receiver coil with the detuning circuit and a low input preamplifier.

between the gaps.

Adjustments in the overlapping distance do not guarantee decoupling between the next nearest neighbor. Preamplifier decoupling is generally used for the receiver coil to enhance the extent of decoupling between the next nearest neighbor elements. For decoupling among the next nearest neighbors, each single element can be connected to low input impedance preamplifiers by utilizing a preamplifier decoupling technique.

All detuning states and preamplifier decoupling are generally measured by using a network analyzer. To check the state of the detuning and preamplifier decoupling, a double probe with a minimum correlation between two probes (< -70 dB) can be used.

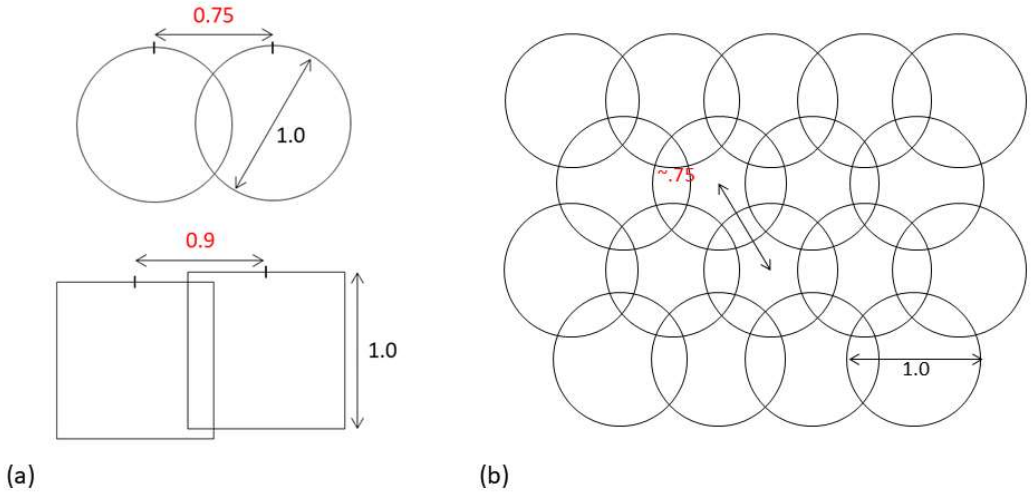

Figure 6. Optimal distance between two elements (a) and a 2D array structure (b) to equip the overlapping decoupling technique. Immediately adjacent coils are overlapped to set their mutual inductance to zero therefore eliminating the problem of splitting resonances for the nearest neighbors.

1.3.3. S-parameters and decoupling technique for tuning a RF coil

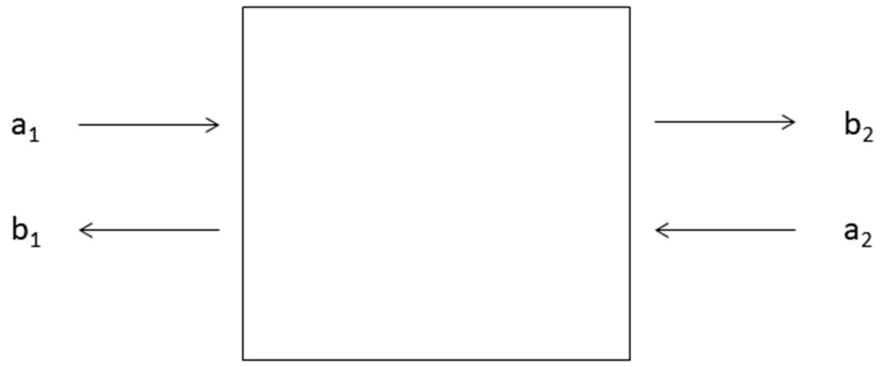

Figure 7. Block diagram of two port system

To evaluate the performance of RF coils, the scattering parameter (S-parameter) is measured with a network analyzer. Figure 7 shows a schematic of a two port system. S-parameter matrix for the two port system is given by:

$$\begin{matrix} b_1 \\ b_2 \end{matrix} = \begin{pmatrix} S_{11} & S_{12} \\ S_{21} & S_{22} \end{pmatrix} \begin{pmatrix} a_1 \\ a_2 \end{pmatrix} \quad (1.5)$$

Expanding the matrices into equations are given as:

$$b_1 = S_{11}a_1 + S_{21}a_2 \text{ and } b_2 = S_{21}a_1 + S_{22}a_2 \quad (1.6)$$

The equation gives the relationship between the reflected and incident power waves at each port in terms of S-parameters. When port 1(a_1) encounters an incident power wave, it may result in either port 1 (b_1) or port 2 (b_2). However, if port 2 is terminated in a load identical to the system impedance, then by the maximum power transfer theorem, b_2 will be completely absorbed making a_2 equal to zero. The S-parameters are given as:

$$S_{11} = \frac{b_1}{a_1} = \frac{V_1^-}{V_1^+} \text{ and } S_{21} = \frac{b_2}{a_1} = \frac{V_2^-}{V_1^+} \quad (1.7)$$

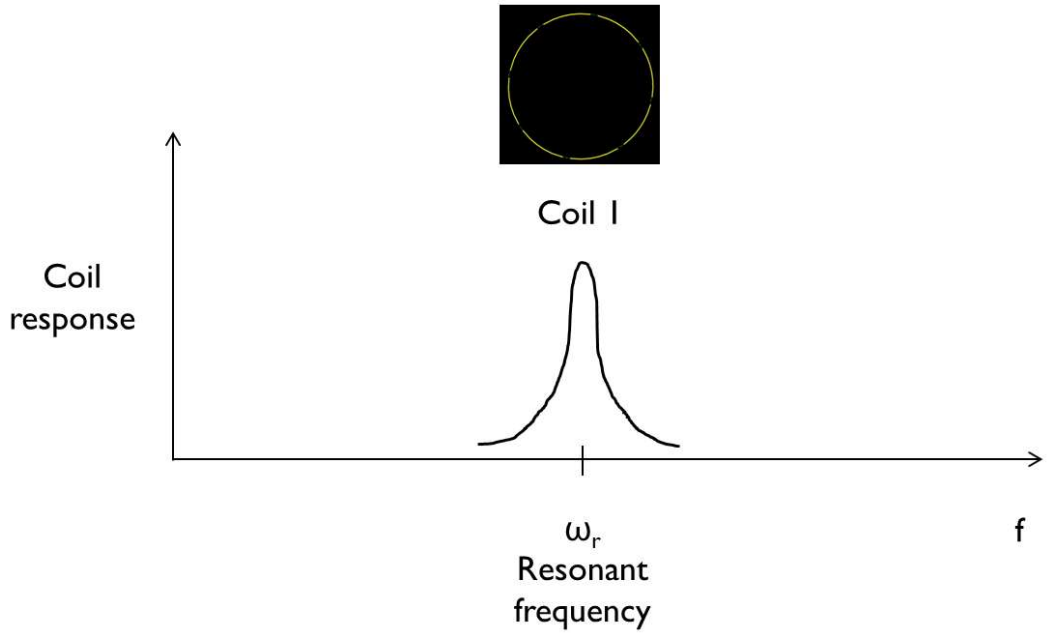

Figure 8. A tuned loop circuit on resonance.

If port 1 is terminated in the system impedance, then a_1 is zero.

$$S_{12} = \frac{b_1}{a_2} = \frac{V_1^-}{V_2^+} \text{ and } S_{22} = \frac{b_2}{a_2} = \frac{V_2^-}{V_2^+} \quad (1.8)$$

Each two port S-parameter has the following generic descriptions. S_{11} and S_{22} are the reflection coefficients (S_{11} is the input port voltage reflection coefficient and S_{22} is the output port voltage reflection coefficient). S_{12} and S_{21} are the coupling coefficients (S_{12} is the reverse voltage gain and S_{21} is the forward voltage gain). The value of S_{11} is used to adjust the performance of a single element, as shown in figure 8, and S_{21} and S_{12} are used to evaluate the coupling between multi-channel coils [32].

To design RF coils as an array, the mutual inductance from the arrayed surface coils can reduce the performance of the RF coils and split the resonance peak, as shown in figure 9. There are other methods available for reducing the coupling between the RF coils in addition to that which was discussed at the previous chapter. The other decoupling method involves capacitive decoupling and inductive decoupling methods that are generally used in transceiver array coils. The capacitive decoupling and inductive

decoupling methods are intended to decouple between the elements with specific values of capacitors and inductors, respectively.

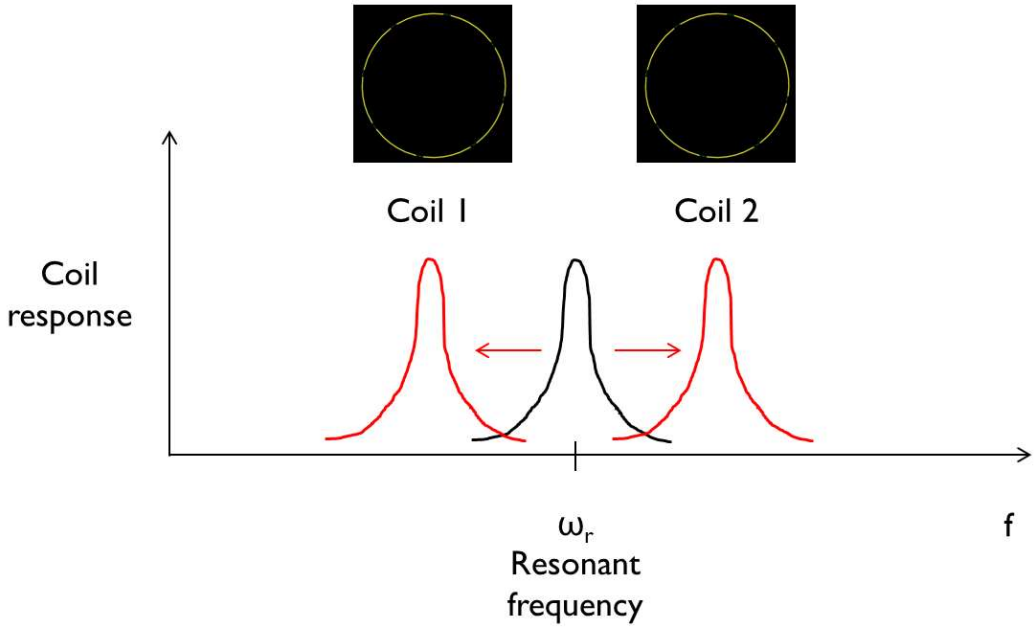

Figure 9. Response of two adjacent surface coils tuned to the same frequency (ω_r). The original resonances are split into two resonances and the sensitivity of the coils at frequency (f), is greatly reduced.

1.3.4 Resonant frequency (ω_r) and quality (Q) factor

To understand the concept of resonance and how the RF coil operates, we need to consider the RLC circuit. According to Kirchhoff's law, we obtain

$$\mathrm{RI} + \frac{-i}{\omega C} I + i\omega L I = V \tag{1.7}$$

where ω is angular frequency and i is imaginary number [33]. Hence, the current is given by

$$\mathrm{I} = \mathrm{V}\left(\mathrm{R} + \frac{-i}{\omega C} + i\omega L\right)^{-1} \tag{1.8}$$

If R is zero, current (I) can be

$$\begin{aligned} \mathrm{I} &= \mathrm{V}\left(\frac{-i}{\omega C} + i\omega L\right)^{-1} \\ &= \mathrm{V}\left[\frac{-L}{i\omega}\left(\omega^2 - \frac{1}{LC}\right)\right]^{-1} \end{aligned} \tag{1.9}$$

from which it is clear that current (I) will be infinite when

$$\omega = \omega_r = \frac{1}{\sqrt{LC}} \tag{1.10}$$

This is called the resonance, as shown in figure 8 (ω_r is referred to as the resonant frequency). Although R cannot be complete zero and the magnitude of I cannot be infinity, the maximum current flow is at ω_r.

When R is not zero, some energy will be dissipated in the circuit which results in a decrease in the efficiency of the circuit. To measure the efficiency of the circuit, the quality (Q) factor is defined as

$$\mathrm{Q} = \frac{1}{R}\sqrt{\frac{L}{C}} = \frac{\omega_r L}{R} = \frac{\omega_r}{\Delta\omega} \tag{1.11}$$

In a resonant circuit, ω_r is the square root of $\frac{1}{LC}$. It is difficult to measure R, L and C of the circuit in a complex circuit. The Q factor can be acquired experimentally by dividing the center frequency by the 3 dB bandwidth.

1.4 Radiative antenna for ultra-high-field (UHF) MRI

Radiative type antennas have been proposed as building blocks for such UHF transmit arrays and have recently shown promising performance particularly for applications related to the human torso, thus enabling improved transmit B_1 efficiency and minimized power deposition in the imaging target (i.e. SAR). Compared to the other RF coil types, i.e., loops or microstrip type structures, dipole antennas have more favorable Poynting vectors, and can achieve greater penetration depth. However, radiative antennas face greater challenges in minimizing the mutual coupling between neighboring elements. For applications to the human torso, this challenge is mitigated by positioning the antenna in close proximity to the body, thus promoting maximal coupling between the sample and the antenna. However, mutual coupling and radiation remain a significantly bigger problem for human head applications due to the relatively large and non-uniform gap between the head and the antenna array.

In the UHF regime, traveling wave behavior produces a significant amplitude and non-uniform phase over the sample for the electric and magnetic (B_1) fields associated with the RF leading to a non-uniform power deposition, image intensity, SNR and CNR. Figure 10 shows monopole antenna arrays which are one of the radiative type antennas with a λ/4 length [13]. Figure 10a shows the original monopole antenna array which has a λ/4 length antenna and separate ground plane. The monopole antenna array has been extended to accommodate human brain imaging, as shown in figure 10b. Figure 10c shows the upgraded version of the extended monopole antenna array (figure 10b) to reduce SAR and improve the uniformity of the B_1^+ and B_1^- fields.

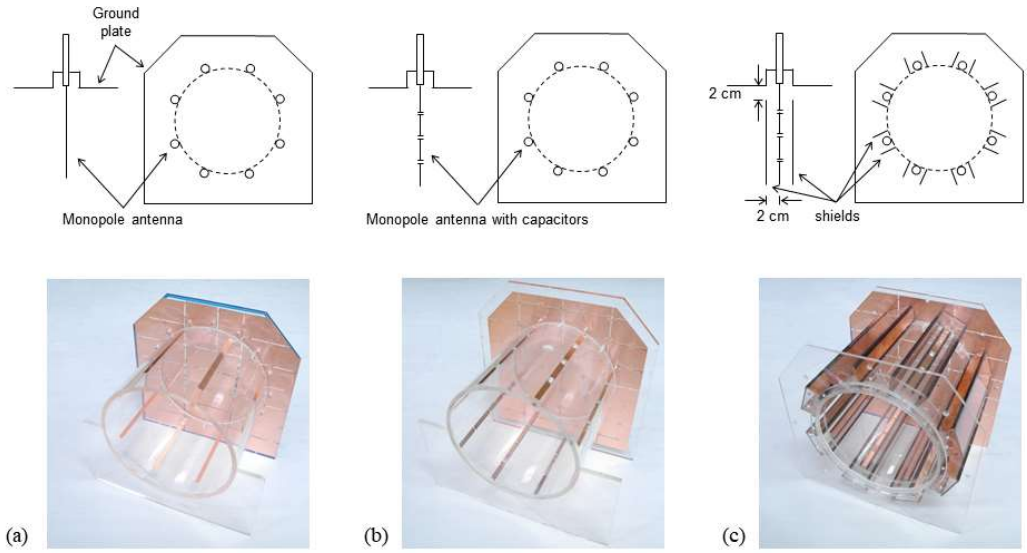

Figure 10. Schematic and structure of an 8-channel monopole antenna array (a), the 8-channel extended monopole antenna array (b) and (c) the 8-channel extended monopole antenna array with individual shields.

1.5 High dielectric constant (HDC) materials for MR applications

Nonconductive dielectric materials were originally equipped in an antenna as a dielectric resonator (DR) for the microwave or millimeter wave. The structure of the DR is configured with the dielectric material, the resonating antenna and the ground plane. Radio waves are introduced into the resonator material from the antenna, and they bounce back and forth between the resonator walls forming standing waves. The walls of the resonator are partially transparent to the radio waves, allowing the radio power to radiate into the space. To maximize the SNR, high dielectric constant (HDC) materials have been adapted for use in MRI. Slurried (ε=333) and solid (ε=100) types of HDC materials are generally used in MRI, as shown in figure 11. Various HDC materials have been examined in attempts to improve, not only of the SNR but also the transmit B_1^+ efficiency and B_1 field uniformity in imaging [34-36]. Imaging qualities in various clinical applications have been improved with HDC materials.

In typical MRI applications, HDC materials are positioned between the subject and the RF coil, and this has improved local B_1^+ and B_1^- fields for many UHF applications. The displacement current generated by the dielectric materials boosts the SNR and the B_1^+ efficiency near the HDC materials. However, there are some major hurdles associated with the use of heavy HDC materials. For example, the distances between the subjects and HDC materials should be aligned differentially depending on the size of the subject such as a human head or a body.

Figure 11. Slurried (a) and solid (b) types of HDC materials. The solid type of HDC materials are highly preferred for use in MR applications. The reason is that the solid type (σ = 0.0031 S/m) of HDC materials shows lower conductivity values compared to the slurry type (σ = 0.7 S/m) of HDC materials.

1.6 Objective and Overview of this thesis

Our major interest is in MRI of the human brain at UHF by utilizing the currently available highest human imaging MR field worldwide, which is 10.5 T. The aim of this thesis was to investigate three closely related problems, as follows: (1) how can we construct an RF coil with a high B_1^+ efficiency ($B_1^+/\sqrt{W}$), (2) how can we construct an RF coil with a low SAR and also achieve a higher SAR efficiency ($B_1^+/\sqrt{\text{peak } SAR_{10g}}$) and (3) from a practical standpoint, how can we produce a well decoupled dense array for deep brain imaging with the associated increased number of coaxial feed cables?

To address these issues, we designed novel transceiver arrays for human head imaging at 10.5 T and evaluated the performance both in EM simulations and experimentally. To create a benchmark for the new type of arrays, both simulations and experimental verifications indicated that the arrays show notable improvements in terms of B_1^+ efficiency, peak 10g SAR and SAR efficiency. Lower SAR and higher SAR efficiencies are particularly important issues associated with UHF imaging. Using some of the developed some arrays, porcine brain and human cadaver brain images were obtained to demonstrate the field of view (FOV) and performance for in-vivo human head imaging.

Chapter 2 describes the design of loop + dipole transceiver antenna array for use in imaging a human head at 447 MHz /10.5 T. This was achieved by a geometrically decoupled combination of a loop and a dipole antenna without inter-element decoupling circuitry. We made comparisons between an 8-channel loop only array, an 8-channel dipole only antenna array and a 16-channel loop + dipole combined antenna array through simulation using the finite difference time domain (FDTD) method and in MR imaging experiments.

In chapter 3 we show that in vivo ^{31}P magnetic resonance spectroscopy (MRS) provides a unique tool for the non-invasive study of brain energy metabolism and mitochondrial function. The assessment of bioenergetic impairment in different brain regions is essential in terms of understanding the pathophysiology and progression of human brain diseases. This study presents a simple and effective approach which allows the interleaved measurement of ^{31}P spectra and imaging from two distinct human brain regions of interest with dynamic B_0 shimming capability. A transistor–transistor logic controller was employed to actively switch the single-channel X-nuclear RF transmitter–receiver between two ^{31}P RF surface coils, thus enabling the interleaved acquisition of two ^{31}P free induction decays (FIDs) from human occipital and frontal lobes within the same repetition time. Linear gradients were incorporated into the RF pulse sequence to perform first-order dynamic shimming to further improve spectral resolution. The overall results demonstrate that the approach provides a cost-effective and time-efficient solution for obtaining reliable ^{31}P MRS measurements of cerebral phosphate metabolites and adenosine triphosphate (ATP) metabolic flux from two human brain regions with a high detection sensitivity and spectral quality at 7 T. The same design concept can be extended

to acquire multiple spectra from more than two brain regions or can be employed in other magnetic resonance applications beyond the ^{31}P spin.

In chapter 4, we evaluate the performance both in simulations and experiments of two 10.5 T head transceiver arrays. The first is a 16-channel monopole/dipole hybrid array (referred to as a mono-dipole array for brevity). The second is a 16-channel monopole/HDC disk dipole array. (A combination of two 8-channel arrays: a monopole array and a HDC disk dipole array). These novel coil designs were compared against a standard 16-channel stripline array to evaluate the relative benefits and drawbacks of these systems.

In chapter 5, we evaluated the performance of 10.5 T RF coils composed of dipole antennas and HDC ceramic materials that were placed in close proximity to the dipole antenna. We investigated the impact of the location of the HDC material relative to the dipole antenna. Both simulations and experimental findings indicate that a counterintuitive "Flipped" geometry in which the dipole is positioned between the HDC material and the sample results in notable improvement in terms of B_1^+ efficiency. We suggest that this new setup for UHF transmit arrays should be explored further.

In chapter 6, at the frequencies required for UHF MRI applications, multi-element transmit arrays with independently controllable transmit channels are essential for achieving acceptable B_1^+ field uniformity and to optimize transmit efficiency. Here we describe an asymmetric sleeve antenna array, which uses a novel antenna concept for UHF human head imaging. Unlike its symmetric counterpart, the asymmetric sleeve antenna uses a short floating cable trap which is shorter than the monopole antenna. To demonstrate the advantage of such an asymmetric sleeve antenna array, we compared it to a dipole antenna array with the same dimensions both in electromagnetic field simulations and experimentally at 10.5 T. The 16-channel asymmetric sleeve antenna array showed a higher B_1^+ efficiency compared to the 16-channel dipole antenna array in both the simulation and experimental results. Simulations of the sleeve antenna array indicate a lower SAR and a higher SAR efficiency at 10.5 T compared to the dipole antenna array with the same number of channels. High resolution human cadaver images were obtained with the 16-channel asymmetric sleeve antenna array at 10.5 T.

The final chapter provides a brief summary and general discussion of these findings. Our findings sit at the center of several broad debates that are currently underway in the fields of biomedical engineering and electrical engineering. As such, we anticipate it will have a high impact and gather broad interest towards both ultra-high resolution cortical and deep brain imaging.

1.7 References

1 Duyn, J. H. *et al.* High-field MRI of brain cortical substructure based on signal phase. *Proceedings of the National Academy of Sciences* **104**, 11796-11801 (2007).

2 Guérin, B. *et al.* The ultimate signal-to-noise ratio in realistic body models. *Magnetic resonance in medicine* **78**, 1969-1980 (2017).

3 Lattanzi, R. *et al.* Approaching ultimate intrinsic signal-to-noise ratio with loop and dipole antennas. *Magnetic resonance in medicine* **79**, 1789-1803 (2018).

4 Pohmann, R., Speck, O. & Scheffler, K. Signal-to-noise ratio and MR tissue parameters in human brain imaging at 3, 7, and 9.4 tesla using current receive coil arrays. *Magnetic resonance in medicine* **75**, 801-809 (2016).

5 Uğurbil, K. Magnetic resonance imaging at ultrahigh fields. *IEEE Transactions on Biomedical Engineering* **61**, 1364-1379 (2014).

6 Uğurbil, K. Imaging at ultrahigh magnetic fields: History, challenges, and solutions. *Neuroimage* **168**, 7-32 (2018).

7 Wiesinger, F. *et al.* Parallel imaging performance as a function of field strength—an experimental investigation using electrodynamic scaling. *Magnetic Resonance in Medicine: An Official Journal of the International Society for Magnetic Resonance in Medicine* **52**, 953-964 (2004).

8 Vaughan, J. T. *et al.* 7T vs. 4T: RF power, homogeneity, and signal-to-noise comparison in head images. *Magnetic Resonance in Medicine: An Official Journal of the International Society for Magnetic Resonance in Medicine* **46**, 24-30 (2001).

9 Yang, Q. X. *et al.* Analysis of wave behavior in lossy dielectric samples at high field. *Magnetic Resonance in Medicine: An Official Journal of the International Society for Magnetic Resonance in Medicine* **47**, 982-989 (2002).

10 Kang, C.-K., Kim, H.-K., Son, Y.-D., Yeong-Bae, L. & Woo, M.-K. (Google Patents, 2019).

11 Raaijmakers, A. *et al.* Design of a radiative surface coil array element at 7 T: the single-side adapted dipole antenna. *Magnetic resonance in medicine* **66**, 1488-1497 (2011).

12 Wiggins, G. C., Zhang, B., Lattanzi, R., Chen, G. & Sodickson, D. in *Proceedings of the 20th Annual Meeting of ISMRM, Melbourne, Australia.* 541.

13 Woo, M. K. *et al.* Extended monopole antenna array with individual shield (EMAS) coil: An improved monopole antenna design for brain imaging at 7 tesla MRI. *Magnetic resonance in medicine* **75**, 2566-2572 (2016).

14 Ertürk, M. A., Raaijmakers, A. J., Adriany, G., Uğurbil, K. & Metzger, G. J. A 16-channel combined loop-dipole transceiver array for 7 T esla body MRI. *Magnetic resonance in medicine* **77**, 884-894 (2017).

15 Woo, M. K. *et al.* in *2017 International Conference on Electromagnetics in Advanced Applications (Iceaa).* 1649-1652 (IEEE).

16 Adriany, G. *et al.* A 32-channel lattice transmission line array for parallel transmit and receive MRI at 7 tesla. *Magnetic Resonance in Medicine: An Official Journal of the International Society for Magnetic Resonance in Medicine* **63**, 1478-1485 (2010).

17 Adriany, G. *et al.* Transmit and receive transmission line arrays for 7 Tesla parallel imaging. *Magnetic Resonance in Medicine: An Official Journal of the International Society for Magnetic Resonance in Medicine* **53**, 434-445 (2005).

18 Avdievich, N. *et al.* Evaluation of transmit efficiency and SAR for a tight fit transceiver human head phased array at 9.4 T. *NMR in Biomedicine* **30**, e3680 (2017).

19 Connell, I. R. & Menon, R. S. Shape Optimization of an Electric Dipole Array for 7 Tesla Neuroimaging. *IEEE transactions on medical imaging* **38**, 2177-2187 (2019).

20 Lee, R. F., Giaquinto, R. O. & Hardy, C. J. Coupling and decoupling theory and its application to the MRI phased array. *Magnetic Resonance in Medicine: An Official Journal of the International Society for Magnetic Resonance in Medicine* **48**, 203-213 (2002).

21 Hill, D. & Wait, J. Coupling between a radiating coaxial cable and a dipole antenna. *IEEE Transactions on Communications* **23**, 1354-1357 (1975).

22 Wait, J. & Hill, D. Electromagnetic fields of a dielectric coated coaxial cable with an interrupted shield--Quasi-static approach. *IEEE Transactions on Antennas and Propagation* **23**, 679-682 (1975).

23 Yang, X., Zheng, T. & Fujita, H. in *ISMRM Fourteenth Scientific Meeting Weekend Syllabus.*

24 Bloch, F. Nuclear induction. *Physical review* **70**, 460 (1946).

25 Purcell, E. M., Torrey, H. C. & Pound, R. V. Resonance absorption by nuclear magnetic moments in a solid. *Physical review* **69**, 37 (1946).

26 Lauterbur, P. C. Image formation by induced local interactions: examples employing nuclear magnetic resonance. *nature* **242**, 190-191 (1973).

27 Lauterbur, P. G. & Lai, C.-M. Zeugmatography by reconstruction from projections. *IEEE Transactions on Nuclear Science* **27**, 1227-1231 (1980).

28 Ernst, R. R. & Anderson, W. A. Application of Fourier transform spectroscopy to magnetic resonance. *Review of Scientific Instruments* **37**, 93-102 (1966).
29 Ernst, R. R., Bodenhausen, G. & Wokaun, A. *Principles of nuclear magnetic resonance in one and two dimensions*. Vol. 14 (Clarendon press Oxford, 1987).
30 Kang, C.-K., Woo, M.-K., Hong, S.-M., Kim, Y.-B. & Cho, Z.-H. Intracranial microvascular imaging at 7 T MRI with transceiver RF coils. *Magnetic resonance imaging* **32**, 1133-1138 (2014).
31 Barberi, E. A., Gati, J. S., Rutt, B. K. & Menon, R. S. A transmit-only/receive-only (TORO) RF system for high-field MRI/MRS applications. *Magnetic Resonance in Medicine: An Official Journal of the International Society for Magnetic Resonance in Medicine* **43**, 284-289 (2000).
32 Roemer, P. B., Edelstein, W. A., Hayes, C. E., Souza, S. P. & Mueller, O. M. The NMR phased array. *Magnetic resonance in medicine* **16**, 192-225 (1990).
33 l Mispelter, J., Lupu, M. & Briguet, A. *NMR probeheads for biophysical and biomedical experiments: theoretical principles & practical guidelines*. (Imperial college press, 2006).
34 Haines, K., Neuberger, T., Lanagan, M., Semouchkina, E. & Webb, A. High Q calcium titanate cylindrical dielectric resonators for magnetic resonance microimaging. *Journal of Magnetic Resonance* **200**, 349-353 (2009).
35 Webb, A. Dielectric materials in magnetic resonance. *Concepts in magnetic resonance part A* **38**, 148-184 (2011).
36 Yang, Q. X. *et al.* Manipulation of image intensity distribution at 7.0 T: passive RF shimming and focusing with dielectric materials. *Journal of Magnetic Resonance Imaging: An Official Journal of the International Society for Magnetic Resonance in Medicine* **24**, 197-202 (2006).

Chapter 2

A 16-channel Transceiver Loop + Dipole Antennas Head Array for Human Head Imaging at 10.5T

Published in

Myung Kyun Woo, Russell L Lagore, Lance DelaBarre, Byeong-Yeul Lee, Yigitcan Eryaman, Jerahmie Radder, Arcan Erturk, Gregory Metzger, Pierre-Francois van de Moortele, Kamil Ugurbil and Gregor Adriany, "A 16-channel Transceiver Loop+Dipole Antennas Head Array for Human Head Imaging at 10.5T", 2017 International Conference on Electromagnetics in Advanced Applications (ICEAA), 12 October 2017, 10.1109/ICEAA.2017.8065607

Presented at

Myung Kyun Woo, Russell L Lagore, Lance DelaBarre, Byeong-Yeul Lee, Yigitcan Eryaman, Jerahmie Radder, Arcan Erturk, Gregory Metzger, Pierre- Francois van de Moortele, Kamil Ugurbil, Gregor Adriany, "A Geometrically Adjustable Loop-Dipole (LD) Head Array for 10.5T", 25th ISMRM meeting, Honolulu, USA, 22-27 April, 2017. [Oral presentation #1051]

Submitted to

Myung Kyun Woo[1], Lance DelaBarre[1], Byeong-Yeul Lee[1], Matt Waks[1], Russell Luke Lagore[1], Jerahmie Radder[1], Yigitcan Eryaman[1], Kamil Ugurbil[1] and Gregor Adriany[1] , "Evaluation of a 16-channel transceiver loop + dipole antenna array for human head imaging at 10.5 tesla", Institute of Electrical and Electronics Engineers (IEEE) Access, 10 October 2020

Abstract

Purpose: To evaluate a 16-channel head loop + dipole (LD) transceiver antenna array design for 10.5 tesla (T) human head imaging

Methods: Three different types of arrays with equal inner dimensions - an 8-channel dipole antenna, an 8 -channel loop, and a 16-channel LD antenna arrays - were built and compared. Signal-to-noise ratio (SNR) and B_1^+ efficiency (in units of μT per $\sqrt{W}$) were calculated through simulation and measured in 10.5 T magnetic resonance imaging (MRI) experiments. For the safety validation, 10 g specific absorption rate (SAR) and SAR efficiency (defined as the B_1^+ over$\sqrt{\text{peak } SAR_{10g}}$) were calculated through simulation. Finally, high resolution porcine brain images were acquired with the 16-channel LD antenna array using fast turbo-spin echo (TSE) sequence incorporating B_1 shimming techniques.

Results: Both the simulation and experiments demonstrate that the combined 16-channel LD antenna array showed similar B_1^+ efficiency compared to the 8-channel dipole antenna and loop arrays in a circular polarized (CP) mode. In a central 2 mm × 2 mm region of the phantom, however, the 16-channel LD antenna array shows an improvement in SAR efficiency of ~7 % over the 8-channel dipole antenna and the 8-channel loop arrays, respectively.

Conclusion: We conclude that the proposed 16-channel head LD antenna array design is capable of achieving higher SAR efficiency at 10.5 T compared to either the 8-channel loop-only or the 8-channel dipole-only antenna arrays of the same dimensions.

Keywords

dipole antenna array, human head array, loop array, magnetic resonance imaging, RF coil, ultra-high field

1 | Introduction

Noninvasive exploration of the human body using magnetic resonance imaging (MRI) benefits from the use of ultra-high field (UHF) systems, which are capable of achieving higher signal-to-noise ratios (SNR) than the systems widely used within the current clinical market [4-6,37-39]. Numerous new applications for human brain imaging have been developed for UHF [40-42]. However, the short wavelength in the human body at such frequencies contributes to a significantly non-uniform field distribution [43-45]. Upon expanding the highest MR field strength from 4 tesla (T) [46] to 7 T [38,45] then to 10.5 T [47,48], it became apparent that more control over the transmit field was required to achieve acceptable imaging uniformity in the human body. Considering an average ε_r of 50 for water dominated tissue types at UHF for 10.5 T proton based imaging the resulting shortened wavelength (~95 mm) leads to the type of non-uniform field distribution in the head at 10.5 T previously experienced in the torso at 7 T [49,50].

Loop [51,52] and stripline [53,54] transmit arrays have been the dominant element types for lower field MRI ($<$ 7 T). At 7 T and above, however, dipole type antennas, which were suggested by Raaijmakers et al., can be more efficient for UHF arrays compared to loop and stripline arrays [55]. Dipole antennas have been shown to produce more uniform B_1^+ field patterns and achieve better penetration depth compared to loop and stripline type arrays at UHF [13,56-58]. Thus the advantages of dipole type antennas for UHF have been studied extensively and demonstrated both in theory [59,60], and practice [55,61,62]. However, dipole antennas face greater challenges in minimizing the mutual coupling between neighboring elements.

In this work, we propose a concept of a loop + dipole (LD) antenna array a combined structure of loops and dipole antennas. To increase the density of the number of array elements, this combined structure has been suggested for UHF utilizing the complimentary decoupled fields produced by loops and dipole antennas [49,63]. From 7 T human torso imaging by Erturk et al., a LD antenna array was compared favorably to either individual loop or dipole antenna arrays. To investigate potential benefits for the human head imaging at 10.5 T, we built an 8-channel dipole antenna, an 8-channel loop and the 16-channel combined LD antenna arrays all with the same dimensions and the same overall spacing between individual elements. To evaluate the correlation among the elements, scattering (S) parameters of all three arrays were measured and compared with the phantom on the bench and noise covariance maps were acquired at 10.5 T MRI. Then intrinsic SNR (iSNR) and B_1^+ efficiency (defined as B_1 amplitude per unit square root total power) and of all arrays were calculated and obtained in electromagnetic (EM) field simulation and MR experiments at 10.5 T, respectively. For the safety validation, 10 g SAR and SAR efficiency (defined as (B_1^+ over $\sqrt{\text{peak } SAR_{10g}}$) of all arrays were calculated by the simulation for each type of the arrays. Finally, we obtained high

resolution turbo spin echo (TSE) images of an in vivo porcine brain with the 16-channel LD antenna array incorporating B_1 shimming to explore the image quality.

2 |Methods

2.1 | Coil design and bench measurements

Three different types of coil arrays were built onto similar head support frames, all with the same inner dimension (200 mm × 220 mm). The head support frames, shown in Fig. 1, were fabricated using a 3D printer (F410, Fusion3 Design, Greensboro, NC, USA). The individual formers were made of polyethylene terephthalate glycol-modified (PETG) materials. All arrays had a similar gap (88 mm ± 14 mm) between individual elements. In other words, sets of eight loops and eight dipole antennas were mounted for the 16-channel LD antenna array. All elements of the 8-channel dipole antenna and the 8-channel loop arrays were mounted directly on a tighter fitting 3D printed elliptical housing frame (4 mm). For only the 16-channel LD antenna array, eight 12 mm thick Teflon bars were attached on the patient side of each fractionated dipole antenna element [64]. These Teflon bars placed these elements of the 16-channel LD antenna array (outer diameter: 232 mm × 252 mm) further from the load compared to the 8-channel dipole antenna and the 8-channel loop arrays (outer diameter: 208 mm × 228 mm). As shown in Fig. 1b and 1c on the anterior side, one element of the 8-channel loop array and one set (one pair of a loop and a dipole antenna) of the 16-channel LD antenna array was shifted upwards by 40 mm compared to the other seven elements and sets, respectively.

The 16-channel LD antenna array was configured with loops and dipole antennas printed on opposite sides of the same FR4 boards (Advanced circuits, Maple Grove, MN, USA). The same loop size (60 mm × 100 mm) was chosen for the 8-channel loop and the 16-channel LD antenna arrays. Fractionated dipole antennas [64] were mounted for the 16-channel LD antenna array, while straight dipole antennas were used for the 8-channel dipole antenna array. Tuning inductors were used to reduce the physical length of the dipole antenna to 180 mm for both the 8-channel dipole antenna and the 16-channel LD antenna arrays, respectively. Furthermore, the anterior dipole element of the 16-channel LD antenna array was shortened to a total length of 100 mm with tuning inductors positioned at the feed point. Fine tuning of all dipole type antennas was performed with slight modifications in the feed point inductors. The loops were tuned with four 4.7 pF, two 5.1 pF ceramic capacitors (100B series, American Technical Ceramics, Huntington Station, NY, USA) and one variable capacitor (JZ200HV, Knowles Voltronics, Cazenovia, NY, USA). A lattice balun with two 10 pF ceramic capacitors and two 12.5 nH inductors (A04T_L, Coilcraft, Coilcraft Inc., Cary, IL, USA) was used for all matching networks of all three arrays at 447 MHz.

S-parameters of all arrays were measured on the bench using a 16-channel network analyzer (ZNBT8, Rohde & Schwarz, Munich, Germany). Input reflection and coupling coefficients are shown in Table 1. For realistic loading conditions reflecting that of a human head and neck, these values were measured while the arrays were loaded with a human head shaped spherical phantom with short neck structure [65]. This human head

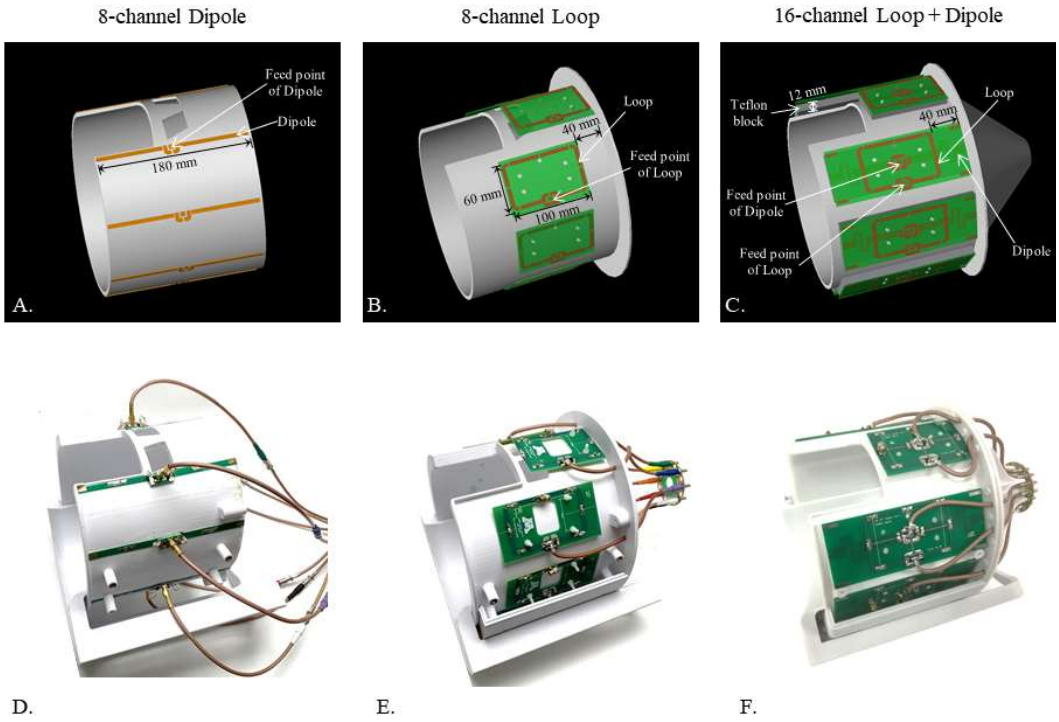

Fig. 1 3D drawing (a-c) and corresponding photographs (d-f) of an 8-channel dipole antenna, an 8-channel loop, and a 16-channel LD antenna arrays.

shaped phantom (diameter: 150 mm and height: 180 mm) have the electrical properties corresponding to a PVP-agar gel (conductivity (σ) of 0.69 S/m and the relative permittivity (ε_r) of 49). For the reference of isocenter in the phantom, a small cylinder (diameter: 30 mm and height: 50 mm) filled with oil (conductivity: 0.32 S/m and the relative permittivity of 2.8) was inserted in the phantom from the end of neck side of the phantom. Dielectric parameters were measured with DAKS-12 coaxial dielectric probe (SPEAG AG, Zurich, Switzerland) at 447 MHz.

2.2 | Experimental setup

A 10.5 T magnet with an 88 cm free bore diameter (Agilent, Santa Clara, CA, USA) was used in conjunction with a whole body gradient (Siemens, Erlangen, Germany). The 16-channel full parallel transmit console (Siemens Healthineers, Erlangen, Germany) was equipped with 16 channel 2 KW RF power amplifiers. All data presented were acquired with equal RF transmit power per channel with a custom built in-bore 16-channel transmit/receive interface. Noise covariance matrices of all arrays were obtained to evaluate crosstalk between all elements experimentally, as shown in Fig. 2 [66]. Fig. 3 displays relative transmit field maps (B_1^+ profiles) of individual elements in a phantom for all arrays, obtained using an actual flip angle imaging (AFI) sequence [67]. For this the AFI sequence (TR1/TR2 = 25/115 ms, TE = 3.39 ms, nominal flip angle = 60°, GRAPPA

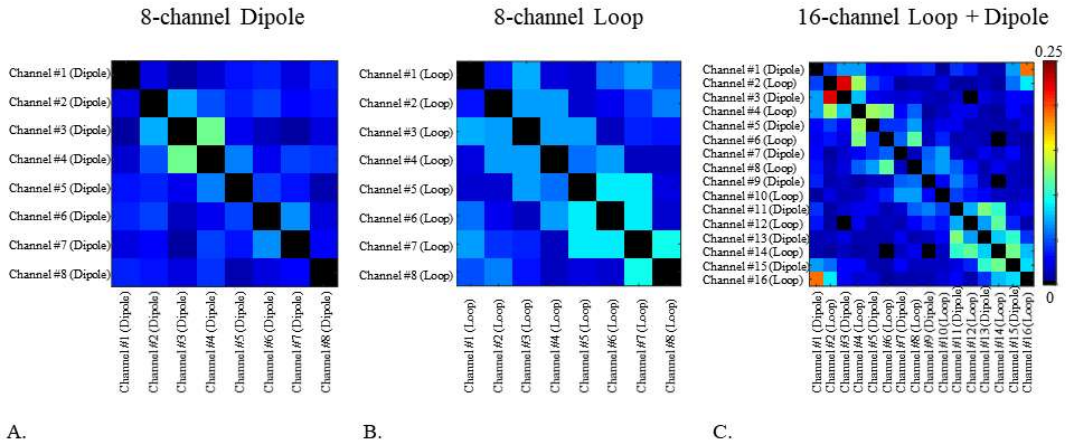

Fig. 2 Noise covariance matrices of the 8-channel dipole antenna (a), the 8-channel loop (b), and the 16-channel LD antenna (c) arrays. The color bar represents the noise covariance coefficient

(R=2) and resolution = 2 mm × 4 mm × 6 mm) was used to obtain transmit B_1^+ fields. The flip angle (α) with short TR_1 and TR_2 was calculated and converted to B_1^+ [68]. A gradient echo (GRE) sequence (TR = 4000 ms, TE = 3.00 ms, TA = 7:48 ms, nominal flip angle = 60°, FOV = 354 × 354 and resolution = 3.0 mm × 1.5 mm × 3 mm) was obtained to calculate the iSNR (Fig. 4) with the human shaped phantom at the isocenter of the magnet.

High resolution turbo spin echo (TSE) images with TR = 5000 ms, TE = 72 ms, TA = 3:45 and BW = 488 Hz/pixel was obtained with in-vivo porcine. The resolution of these images was 0.75 mm × 0.75 mm × 2 mm in the axial, coronal, and sagittal planes.

2.3 | Simulation and numerical analysis

All electromagnetic simulations were performed using a commercial computational EM simulation software (XFdtd, REMCOM, State College, PA, USA) using a phantom with the dimensions and contents as previously described. All data were calculated utilizing MATLAB (The Mathworks, Inc., Natick, MA, USA) after EM simulation and experiments. In Fig. 4, iSNR was calculated using B_1^- fields of the 8-channel dipole antenna, the 8-channel loop, and the 16-channel LD antenna arrays both with simulation (Fig. 4a-c) and experiments (Fig. 4d-f) in the phantom [69-71]. The SNR maps were calculated from the proton density-weighted images by dividing the flip angle maps and then divided by the measured noise in the scanner. Noise was obtained without RF pulses.

To evaluate the B_1^+ efficiency ($B_1^+/\sqrt{W}$), the B_1^+ fields with circularly polarized (CP) mode were normalized to 1 W both in simulation and experiments. Simulated (Fig. 5a-c) and experimental (Fig. 5d-f) B_1^+ efficiency of the 8-channel dipole antenna, the 8-channel loop, and the 16-channel LD antenna arrays are shown. 10 g SAR values and SAR efficiency ($B_1^+ / \sqrt{\text{peak } SAR_{10g}}$) values were calculated by simulation software and

utilized by MATLAB. For the quantitative comparison, the highest region of interest (ROI), B_1^+ efficiency, 10 g SAR, SAR efficiency, and central location (2 mm × 2 mm) of iSNR were chosen in the axial plane (red arrows shown in figure indicate ROIs) for all arrays and those values were summarized in Table 2.

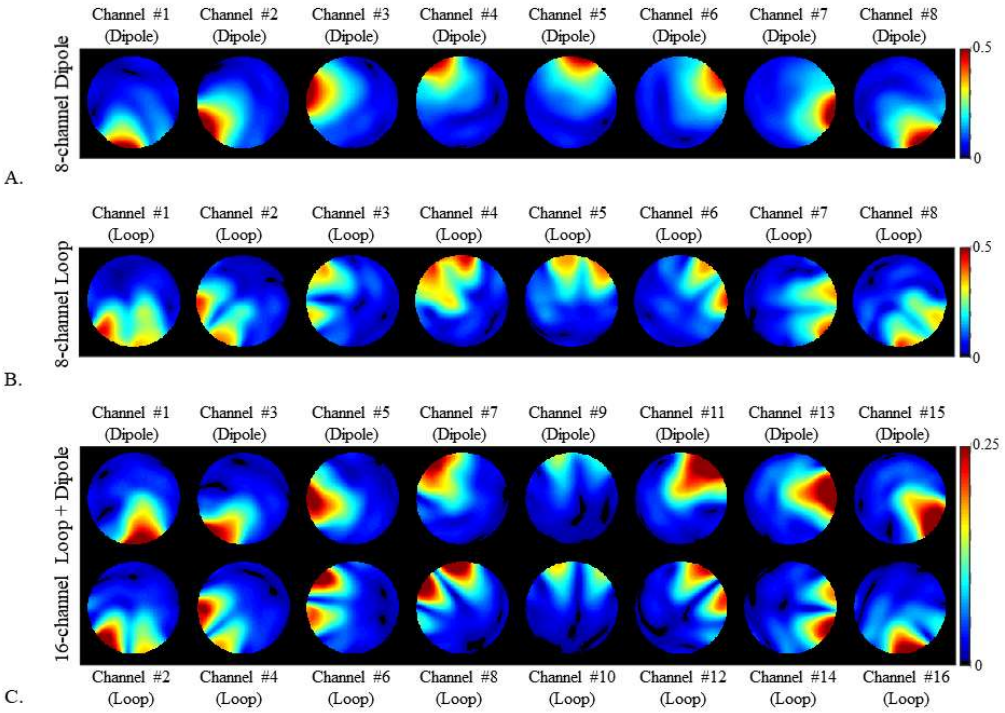

Fig. 3 Relative individual transmit fields of the 8-channel dipole antenna (a), the 8-channel loop (b), and the 16-channel LD antenna (c) arrays. These figures show relative percentage contribution of each transmitter on each pixel.

3 |Results

Table 1 indicates a similar range of S_{11} values for all three arrays, -12.5 dB to -36.5 dB for the 8-channel dipole antenna array, -15.1 dB to -22.1 dB for the 8-channel loop array, and -12 dB to -24.1 dB for the 16-channel LD antenna array. Due to the increased number of elements, the 16-channel LD antenna array shows relatively higher S_{21} coupling values (-8.2 dB to -24.1 dB) compared to both the 8-channel dipole antenna (-13.9 dB to -19.6 dB) and the 8-channel loop (-9.5 dB to -16 dB) arrays. As indicated in Fig. 2, the noise covariance of the 16-channel LD antenna array also shows higher coupling to neighboring elements among the channels compared to the 8-channel dipole antenna and the 8-channel loop arrays. The maximum correlation value was 0.11 for both the 8-channel dipole antenna and the 8-channel loop arrays. For the 16-channel LD antenna array, the noise covariance among the elements was increased - but still an acceptable value (0.25) was achieved.

Fig. 3 shows transmit field patterns of individual elements in the arrays. The patterns indicate that individual elements were able to generate acceptable B_1^+ in all arrays. An individual relative B_1^+ magnitude map is the magnitude of each individual transmitter divided by the sum of the magnitude of all sixteen individual transmitter maps. Channel #8 (loop) and #9 (dipole antenna) of the 16-channel LD antenna array were located 40 mm higher up compared to the other elements. Hence these loop and the dipole antennas (channel #8 and #9) showed relatively lower B_1^+ field contribution compared to the other elements of the 16-channel LD antenna array.

In Fig. 4, SNR values were compared among the arrays both in the simulation and experiments. The central SNR values of all arrays in the ROI which is located in the

	S_{11} (dB) (Reflection coefficient)			S_{21} (dB) (Coupling coefficient between adjacent)		
	Min	Max	Mean	Min	Max	Mean
8-channel Dipole	-36.5	-12.5	-22.2	-19.6	-13.9	-16.6
				Dipole to Dipole		
8-channel Loop	-22.1	-15.1	-16.5	-16.0	-9.5	-11.8
				Loop to Loop		
16-channel Loop + Dipole	-24.1	-12.0	-15.4	-24.0	-12.0	-13.7
				Loop to Loop		
				-16.2	-8.2	-10.4
				Loop to Dipole		
				-24.1	-18.5	-21.4
				Dipole to Dipole		

Table 2 Quantitative comparison of B_1^+ efficiency (simulation and experiments), 10 g SAR, SAR efficiency, and SNR (simulation and experiments) among the 8-channel dipole antenna, the 8-channel loop, and the16-channel LD antenna arrays with phantom in the ROI marked for the highest value.

middle of the phantom were shown similarly in the simulation and the experiment. We measured that the 8-channel dipole antenna array shows ~7.4 % and ~15.2 % higher iSNR compared to the 8-channel loop and the 16-channel LD antenna arrays in the ROI, respectively.

In Fig. 5, B_1^+ efficiency values in the simulation and the experiment are shown highly consistently. The highest B_1^+ efficiency values of all arrays in the ROI which is located in the middle of the phantom were shown similarly in the simulation and the experiment with circularly polarized (CP) mode. Red arrows indicate ROIs. At the periphery of the phantom, the 8-channel loop array (Fig. 5b and 5e) showed higher B_1^+ efficiency compared to the 8-channel dipole antenna (Fig. 5a and 5d) and the 16-channel LD antenna (Fig. 5c and 5f) arrays. In supplementary Fig. 1 and the supplementary Table 1, similar B_1^+ efficiency values among all the arrays were observed in the ROIs of the human model (Duke) [72].

Table 2 summarizes the key values of the calculation and measurements from the simulation and the experimental results. Importantly, we observed the lowest peak 10 g SAR with the 16-channel LD antenna array (0.4 W/kg) compared to the 8-channel dipole antenna (0.51 W/kg) and the 8-channel loop (0.53 W/kg) arrays. As observed in Fig. 4, B_1^+ efficiency values among all arrays were similar. This indicates that the 16-chanel LD

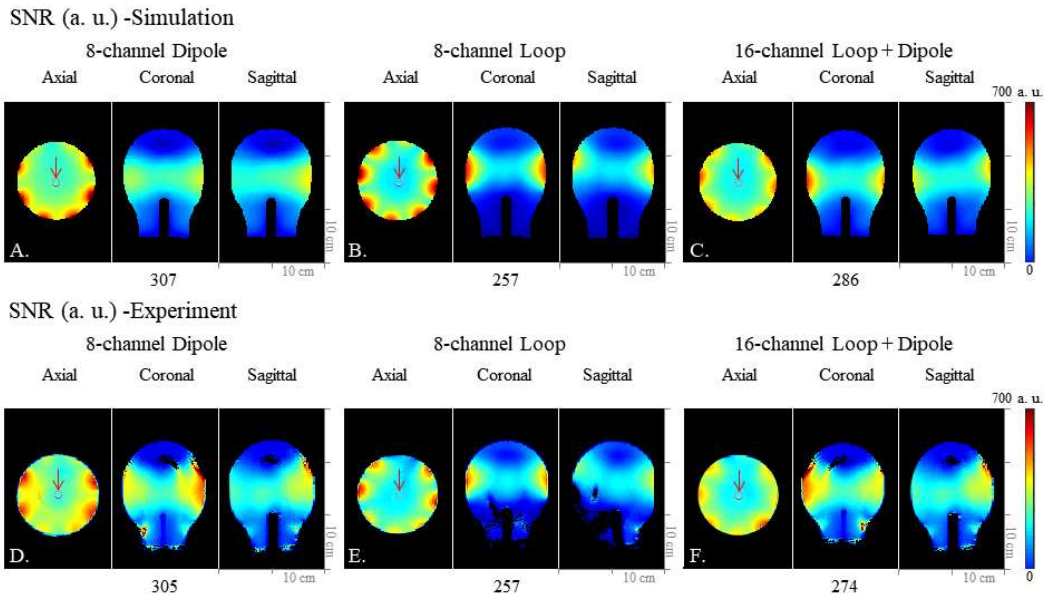

Fig. 4 Simulation (a-c) and experimental (d-f) SNR maps of the 8-channel dipole antenna, the 8-channel loop, and the 16-channel LD antenna arrays. Simulation data set of the 8-channel dipole antenna (a), the 8-channel loop (b), and the 16-channel LD antenna (c) arrays in the axial, coronal, and sagittal planes. Experimental data set of the 8-channel dipole antenna (d), the 8-channel loop (e), and the 16-channel LD antenna (f) arrays in the axial, coronal, and sagittal planes. Red arrows indicate ROIs where values are measured and compared.

antenna array shows the highest SAR efficiency compared to the 8-channel dipole antenna and loop arrays. The SAR efficiency of the 16-channel LD antenna array in the ROI of the phantom shows ~7 % higher values compared to the 8-channel dipole antenna and loop arrays, respectively. In the supplementary Fig. 2, however, the 16-channel LD antenna array showed ~ 12 % higher SAR efficiency compared to the 8-channel dipole antenna and the 8-channel loop arrays with the human model.

Fig. 6 shows high resolution T_2* weighted TSE images of an in vivo porcine brain obtained with the 16-channel LD antenna array. These images clearly demonstrate remarkably uniform B_1 field distribution with B_1 shimming in the porcine brain.

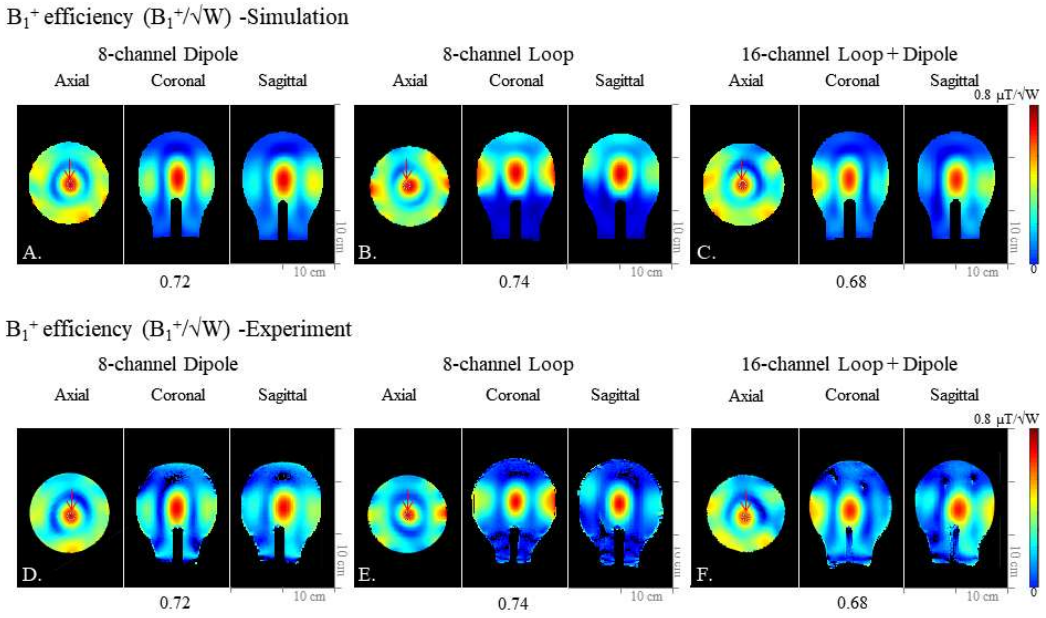

Fig. 5 Simulation (a-c) and experimental (d-f) B_1^+ efficiency ($B_1^+/\sqrt{W}$) maps of the 8-channel dipole antenna, the 8-channel loop, and the 16-channel LD antenna arrays. Simulation data set of the 8-channel dipole antenna (a), the 8-channel loop (b), and the 16-channel LD antenna (c) arrays in the axial, coronal, and sagittal planes. Experimental data set of the 8-channel dipole antenna (d), the 8-channel loop (e), and the 16-channel LD antenna (f) arrays in the axial, coronal, and sagittal planes. Red arrows indicate ROIs where values are measured and compared.

4.| Discussions

Overall our results indicate that the array structure of the 16-channel LD concept has the benefit of tighter spacing for head applications at 447 MHz without the need for decoupling circuitry. The 16-channel LD antenna array experienced relatively higher coupling (-8.2 dB) and correlation (0.25) in a set of a loop and a dipole antenna compared to only the 8-channel loop array and only the 8-channel dipole antenna array. However, those are acceptable values to achieve individually functioned field patterns of each elements of the 16-channel LD antenna array in Fig. 3.

All arrays performed consistently between simulation and experiment as shown in Fig. 4 and 5. In our simulation and experimental results at 447 MHz, the 16-channel LD antenna array does not show higher B_1^+ efficiency per se, but we do observed lower SAR values compared to both the 8-channel dipole antenna and the 8-channel loop arrays at 10.5 T. As a result, the 16-channel LD antenna array showed improved SAR efficiency compared to both the 8-channel arrays. All three arrays have the same inner dimensions, however all elements of the 16-channel LD antenna array were placed further by the Teflon blocks from the object compared to the 8-channel loop and the 8-channel dipole antenna arrays. Hence, the SNR performance of the 16-channel LD antenna array does not show the improvement compared to the 8-channel arrays [59,73]. However, the further distance from the object leads the improvement of the safety (10 g SAR) and the 16-channel LD antenna array showed the advantage of SAR efficiency.

	8-channel Dipole	8-channel Loop	16-channel Loop + Dipole
B_1^+ efficiency (μT/√W) -Simulation	0.72	0.73	0.68
B_1^+ efficiency (μT/√W) -Experiment	0.72	0.73	0.68
Peak 10g SAR (W/kg)	0.51	0.52	0.4
SAR efficiency (μT/√W/√kg)	1.00	1.01	1.08
SNR (A.U.) -Simulation	307	257	286
SNR (A.U.) -Experiment	305	257	274

Table 1 S_{11} (reflection coefficient) and S_{21} (coupling coefficient) between the adjacent elements of the 8-channel dipole antenna, the 8-channel loop, and the16-channel LD antenna arrays in dB scale. Note that neither of these arrays have any additional decoupling circuitry and consequently show relative higher coupling coefficient values

5.| Conclusion

A 16-channel LD antenna combination array was developed for 10.5 T human brain imaging. This array is composed of 8 dipole antennas and 8 loops which are geometrically decoupled from each other. Based on performance evaluations using a human head shaped phantom, the 16-channel LD antenna array showed higher SAR efficiency compared to an 8-channel dipole antenna and an 8-channel loop arrays, both in simulation and the experiments. The use of decoupling circuitry for the dipole antenna and loop elements will be evaluated in the future towards achieving better performance.

The dimension we chose for the comparison did not cover the entire phantom, especially at the superior part of the phantom. For the further study, we will evaluate the head shaped dipole antennas and loops to cover the superior part of the brain for the human subject. We will conduct human brain imaging with this array under FDA guidelines.

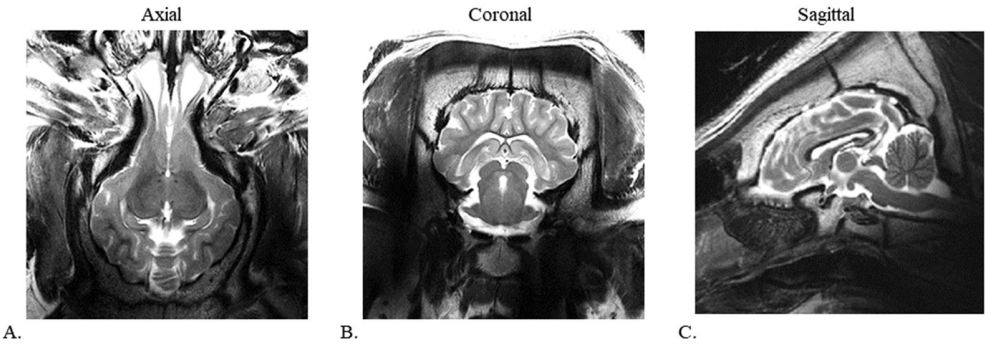

Fig. 6 TSE images of the porcine brain with the 16-channel LD antenna array in the axial (a), coronal (b), and sagittal (c) planes. TR = 5000 ms, TE = 72 ms, TA = 3:45 and BW = 488 Hz/pixel, resolution = 0.75 mm × 0.75 mm × 2 mm.

ACKNOWLEDGMENTS

This project was funded by NIH-U01-EB025144, NIH-S10-RR029672, NIH-P41-EB027061 and NIH-P30-NS076408. Part of this work was presented at the 25th Annual Meeting & Exhibition of ISMRM (abstract #1051).

References

[1] P. A. Bandettini, R. Bowtell, P. Jezzard, and R. Turner, "Ultrahigh field systems and applications at 7 T and beyond: Progress, pitfalls, and potential," *Magn Reson Med,* vol. 67, no. 2, pp. 317-321, Feb, 2012.

[2] R. Pohmann, O. Speck, and K. Scheffler, "Signal-to-noise ratio and MR tissue parameters in human brain imaging at 3, 7, and 9.4 tesla using current receive coil arrays," *Magn Reson Med,* vol. 75, no. 2, pp. 801-809, 2016.

[3] K. Uğurbil, "Magnetic resonance imaging at ultrahigh fields," *IEEE Trans Biomed Eng,* vol. 61, no. 5, pp. 1364-1379, 2014.

[4] K. Uğurbil, "Imaging at ultrahigh magnetic fields: History, challenges, and solutions," *Neuroimage,* vol. 168, pp. 7-32, 2018.

[5] T. Vaughan et al., "Whole-body imaging at 7T: preliminary results," *Magn Reson Med,* vol. 61, no. 1, pp. 244-248, 2009.

[6] T. Vaughan et al., "9.4T human MRI: preliminary results," *Magn Reson Med,* vol. 56, no. 6, pp. 1274-82, Dec, 2006.

[7] C. Kang, MK. Woo, SM. Hong, YB. Kim, and ZH. Cho, "Intracranial microvascular imaging at 7 T MRI with transceiver RF coils," *Magn Reson Imag,* vol. 32, no. 9, pp. 1133-1138, 2014.

[8] P. J. Koopmans, M. Barth, S. Orzada,, and D. G. Norris, "Multi-echo fMRI of the cortical laminae in humans at 7 T," *Neuroimage,* vol. 56, no. 3, pp. 1276-1285, Jun 1, 2011.

[9] E. Moser, F. Stahlberg, M. E. Ladd, , and S. Trattnig, "7-T MR—from research to clinical applications?," *NMR Biomed,* vol. 25, no. 5, pp. 695-716, 2012.

[10] Z. Cao, J. Park, ZH. Cho, , and C. M. Collins, "Numerical evaluation of image homogeneity, signal-to-noise ratio, and specific absorption rate for human brain imaging at 1.5, 3, 7, 10.5, and 14T in an 8-channel transmit/receive array," *J Magn Reson Med,* vol. 41, no. 5, pp. 1432-1439, 2015.

[11] M. A. Erturk et al., "Toward imaging the body at 10.5 tesla," *Magn Reson Med,* vol. 77, no. 1, pp. 434-443, Jan, 2017.

[12] J. T. Vaughan et al., "7T vs. 4T: RF power, homogeneity, and signal-to-noise comparison in head images," *Magn Reson Med,* vol. 46, no. 1, pp. 24-30, 2001.

[13] S. Ogawa et al., "Functional brain mapping by blood oxygenation level-dependent contrast magnetic resonance imaging. A comparison of signal characteristics with a biophysical model," *Biophysical journal,* vol. 64, no. 3, pp. 803-812, 1993.

[14] X. He et al., "First in-vivo human imaging at 10.5 T: Imaging the body at 447 MHz," *Magn Reson Med*, 2019.

[15] A. Sadeghi-Tarakameh et al., "In vivo human head MRI at 10.5 T: A radiofrequency safety study and preliminary imaging results," *Magn Reson Med,* vol. 84, no. 1, pp. 484-496, 2020.

[16] M. A. Ertürk, A. JE. Raaijmakers, G. Adriany, K. Uğurbil, and G. J. Metzger,, "A 16-channel combined loop-dipole transceiver array for 7 T esla body MRI," *Magn Reson Med,* vol. 77, no. 2, pp. 884-894, 2017.

[17] G. J. Metzger, C. Snyder, C. Akgun, T. Vaughan, K. Ugurbil, and PF. Van de Moortele, "Local B1+ shimming for prostate imaging with transceiver arrays at 7T based on subject-dependent transmit phase measurements," *Magn Reson Med,* vol. 59, no. 2, pp. 396-409, 2008.

[18] N. I. Avdievich et al., “Evaluation of transmit efficiency and SAR for a tight fit transceiver human head phased array at 9.4 T,” *Nmr in Biomedicine,* vol. 30, no. 2, pp. e3680, Feb, 2017.
[19] G. Shajan, M. Kozlov, J. Hoffmann, R. Turner, K. Scheffler, and R. Pohmann, “A 16-channel dual-row transmit array in combination with a 31-element receive array for human brain imaging at 9.4 T,” *Magn Reson Med,* vol. 71, no. 2, pp. 870-879, 2014.
[20] G. Adriany et al., “A 32-channel lattice transmission line array for parallel transmit and receive MRI at 7 tesla,” *Magn Reson Med,* vol. 63, no. 6, pp. 1478-1485, 2010.
[21] G. Adriany et al., “Transmit and receive transmission line arrays for 7 Tesla parallel imaging,” *Magn Reson Med,* vol. 53, no. 2, pp. 434-45, Feb, 2005.
[22] A. Raaijmakers et al., “Design of a radiative surface coil array element at 7 T: the single-side adapted dipole antenna,” *Magn Reson Med,* vol. 66, no. 5, pp. 1488-1497, 2011.
[23] S. M. Hong, J. H. Park, M. K. Woo, Y. B. Kim, and Z. H. Cho, “New design concept of monopole antenna array for UHF 7T MRI,” *Magn Reson Med,* vol. 71, no. 5, pp. 1944-52, May, 2014.
[24] C.-K. Kang, H.-K. Kim, Y.-D. Son, L. Yeong-Bae, and M.-K. Woo, "Magnetic resonance imaging apparatus with spirally extended monopole antenna structure," *U.S. Patent No. 10,488,474. 26 Nov. 2019*, 2019.
[25] C. Oezerdem et al., “16-channel bow tie antenna transceiver array for cardiac MR at 7.0 tesla,” *Magn Reson Med,* vol. 75, no. 6, pp. 2553-2565, 2016.
[26] M. K. Woo et al., “Extended monopole antenna array with individual shield (EMAS) coil: An improved monopole antenna design for brain imaging at 7 tesla MRI,” *Magn Reson Med,* vol. 75, no. 6, pp. 2566-2572, 2016.
[27] R. Lattanzi, G. C. Wiggins, B. Zhang, Q. Duan, R. Brown, and D. K. Sodickson, “Approaching ultimate intrinsic signal-to-noise ratio with loop and dipole antennas,” *Magn Reson Med,* vol. 79, no. 3, pp. 1789-1803, Mar, 2018.
[28] A. Pfrommer, and A. Henning, “The ultimate intrinsic signal-to-noise ratio of loop-and dipole-like current patterns in a realistic human head model,” *Magn Reson Med,* vol. 80, no. 5, pp. 2122-2138, 2018.
[29] J. D. Clément, R. Gruetter, and Ö. Ipek, “A human cerebral and cerebellar 8-channel transceive RF dipole coil array at 7T,” *Magnetic resonance in medicine,* vol. 81, no. 2, pp. 1447-1458, 2019.
[30] G. C. Wiggins, B. Zhang, R. Lattanzi *et al.*, “The electric dipole array: an attempt to match the ideal current pattern for central SNR at 7 Tesla,” *Proceedings of the 20th scientific meeting, International Society for Magnetic Resonance in Medicine, Melbourne, Australia,* vol. 541, 2012.
[31] Y. Eryaman et al., “SAR reduction in 7T C-spine imaging using a “dark modes” transmit array strategy,” *Magn Reson Med,* vol. 73, no. 4, pp. 1533-1539, 2015.
[32] A. J. Raaijmakers et al., “The fractionated dipole antenna: A new antenna for body imaging at 7 T esla,” *Magn Reson Med,* vol. 75, no. 3, pp. 1366-1374, 2016.
[33] W. M. Brink, Z. Wu, and A. G. Webb, “A simple head-sized phantom for realistic static and radiofrequency characterization at high fields,” *Magn Reson Med,* vol. 80, no. 4, pp. 1738-1745, 2018.
[34] A. J. Jesmanowicz, S. Hyde, W. Froncisz, and B. J. Kneeland, “Noise correlation,” *Magn Reson Med,* vol. 20, no. 1, pp. 36-47, Jul, 1991.
[35] V. L. Yarnykh, “Actual flip-angle imaging in the pulsed steady state: a method for rapid three-dimensional mapping of the transmitted radiofrequency field,” *Magn Reson Med,* vol. 57, no. 1, pp. 192-200, 2007.

[36] C. M. Collins, and M. B. Smith, “Signal-to-noise ratio and absorbed power as functions of main magnetic field strength, and definition of “90°” RF pulse for the head in the birdcage coil,” *Magnetic Resonance in Medicine: An Official Journal of the International Society for Magnetic Resonance in Medicine,* vol. 45, no. 4, pp. 684-691, 2001.

[37] C. M. Collins, and M. B. Smith, “Calculations of B1 distribution, SNR, and SAR for a surface coil adjacent to an anatomically-accurate human body model,” *Magn Reson Med,* vol. 45, no. 4, pp. 692-699, 2001.

[38] P. Kellman, and E. R. McVeigh, “Image reconstruction in SNR units: a general method for SNR measurement,” *Magn Reson Med,* vol. 54, no. 6, pp. 1439-1447, 2005.

[39] M. K. Woo et al., “A 16-channel transceiver loop+ dipole antennas head array for human head imaging at 10.5 T,” in IEEE-ICEAA, 2017 pp. 1649-1652.

[40] A. Christ et al., “The Virtual Family—development of surface-based anatomical models of two adults and two children for dosimetric simulations,” *Physics in Medicine & Biology,* vol. 55, no. 2, pp. N23, 2009.

[41] J. R. Corea et al., “Screen-printed flexible MRI receive coils,” *Nature communications,* vol. 7, no. 1, pp. 1-7, 2016.

Supplementary figures

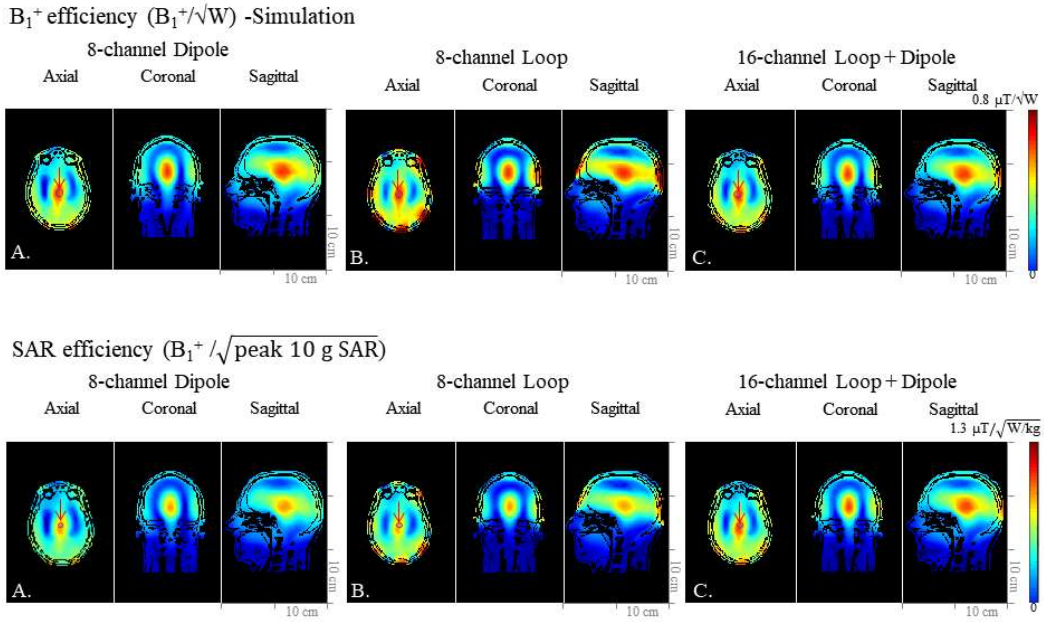

Supplementary figure 1. Simulated B_1^+ efficiency (a-c) and SAR efficiency (d-f) maps of the 8 CH dipole antenna (a), the 8 CH loop (b), and the 16 CH LD antenna (c) arrays in the axial, coronal and, sagittal planes.

Supplementary table

	8-channel Dipole	8-channel Loop	16-channel Loop + Dipole
B_1^+ efficiency	0.65	0.65	0.62
Peak 10 g SAR	0.49	0.52	0.40
SAR efficiency	0.94	0.93	1.06

Supplementary table 1. Simulation based quantitative comparison of B_1^+ efficiency, 10 g SAR, SAR efficiency, and SNR among the 8 CH dipole antenna, the 8 CH loop and, the16 CH LD antenna arrays with human model (Duke) in the ROI marked for the highest value.

Chapter 3

Interleaved ^{31}P MRS imaging of human frontal and occipital lobes using dual RF coils in combination with single-channel transmitter–receiver and dynamic B_0 shimming

Published in

Byeong-Yeul Lee, Xiao-Hong Zhu, Myung Kyun Woo, Gregor Adriany, Scott Schillak, Wei Chen, "Interleaved 31P MRS imaging of human frontal and occipital lobes using dual RF coils in combination with single-channel transmitter–receiver and dynamic B0 shimming" NMR in Biomedicine 31:e3842, 2018

1 | Introduction

In vivo 31P magnetic resonance (MR) spectroscopy (MRS) provides a unique and non-invasive tool for the assessment of cerebral high-energy phosphate metabolites, phosphate lipid metabolism, intracellular pH and redox state of nicotinamide adenine dinucleotide (NAD) and neuroenergetics.1-6 Moreover, the 31P MRS technique in combination with the magnetization transfer (MT) preparation (31P–MT MRS) offers new utility, enabling researchers to non-invasively examine the kinetics of key bioenergetic reactions catalyzed by the creatine kinase (CK) and adenosine triphosphate (ATP) synthase (ATPase) and their metabolic fluxes.7,8 In this regard, in vivo 31P or 31P–MT MRS studies have shown bioenergetic impairment, specifically in the frontal lobe in psychiatric patients, such as those with schizophrenia,9 and in neurodegenerative diseases, such as Alzheimer's disease.10,11

With the increasing recognition of complex neurological disorders involving a behavioral and cognitive impairment commonly linking to dysfunction in specific brain regions,12-16 the examination of functional and metabolic impairments in multiple brain regions of interest is essential to advance our understanding of the underlying pathophysiological mechanisms and to improve the diagnosis and treatment of diseases.

To detect in vivo 31P spectra from multiple brain regions, one common approach is to employ a large-sized 31P radiofrequency (RF) coil in combination with three-dimensional (3D) chemical shift imaging (CSI) for measurement of the 31P MRS signals across the whole brain.17-19 However, the presence of static magnetic field (B0) inhomogeneity in critical human brain regions, particularly the frontal and temporal lobes, as a result of the large susceptibility difference between the brain tissue and surrounding air cavity, poses a technical challenge for B0 field shimming and the acquisition of high-quality 31P MRS data. Another limitation is the relatively low detection sensitivity because of the large volume coil size, resulting in a low signal-to-noise ratio (SNR) or spatial resolution of CSI in the cortical regions of the human brain when compared with the use of RF surface coil(s). An alternative approach to overcome the technical limitations is to use multiple surface coils in combination with multi-channel RF receivers and to split the RF transmission power from a single channel transmit or to use transmitter–receiver (transceiver) arrays or volume coils.20-23 Despite the merits of high detection sensitivity and large imaging coverage, these approaches require advanced hardware equipment, such as multi-channel X-nuclear receivers or transceivers, which are not commonly available, even for the MR scanners equipped with the X-nucleus MRS capability. Moreover, it is challenging to perform regional dynamic B0 shimming for those brain regions prone to susceptibility artifacts, as all 31P signals [or free induction decays (FIDs)] from multiple RF receiver channels need to be acquired at the same time. For instance, strong B0 inhomogeneity in the human frontal lobe causes a magnetic field distortion as a result of the susceptibility difference between the air cavity

and brain tissue, and consequently a broader resonance linewidth and poor spectral quality.24 Therefore, it is a challenge to simultaneously obtain high-quality in vivo 31P spectra or CSIs from distinct brain regions of interest for most MR scanners that are not equipped with advanced shimming technology.25-28

To address these technical difficulties faced by most scanners, we herein present a simple and effective design that incorporates the transistor–transistor logic (TTL) controller and modified RF pulse sequence with an existing single-channel X-nuclear RF transceiver for rapid switching of the RF transceiver connection and interleaved signal acquisition between two distanced 31P RF surface coils covering the human occipital lobe (OL) and frontal lobe (FL), respectively. This design enables the simultaneous assessment of the high-energy phosphorus metabolism from two human brain regions of interest at 7 T, and

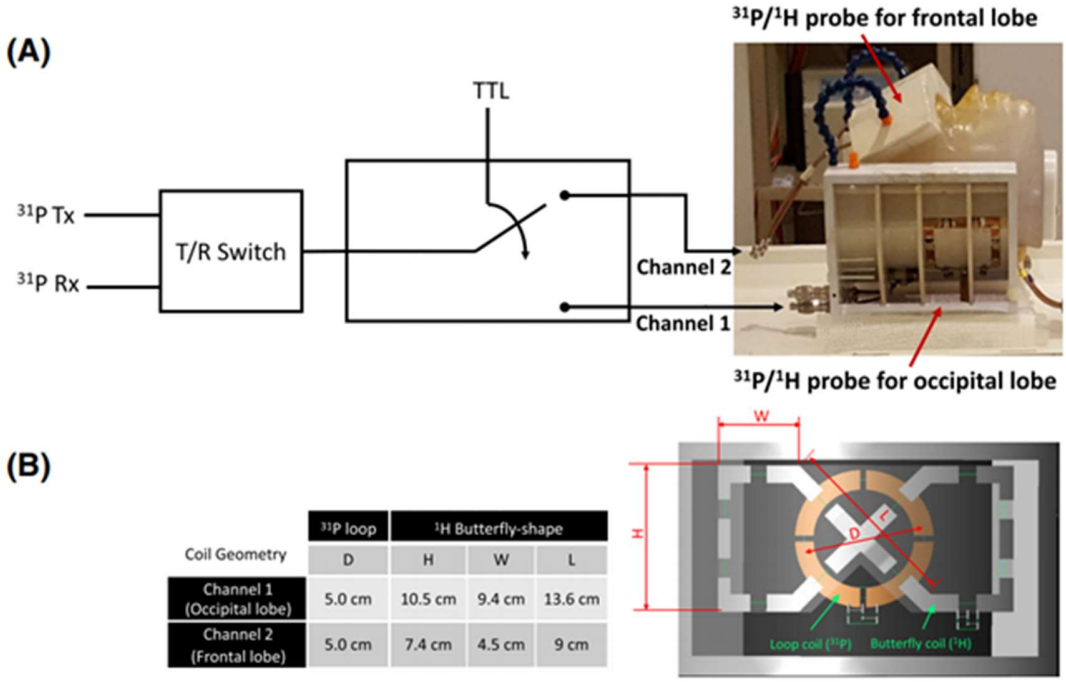

Coil Geometry	^{31}P loop	^{1}H Butterfly-shape		
	D	H	W	L
Channel 1 (Occipital lobe)	5.0 cm	10.5 cm	9.4 cm	13.6 cm
Channel 2 (Frontal lobe)	5.0 cm	7.4 cm	4.5 cm	9 cm

FIGURE 1 Schematic illustration of the dual-coil 31P magnetic resonance spectroscopy (MRS) system for the simultaneous measurement or imaging of 31P–containing metabolites from two brain regions of interest. (A) the system consists of a 31P transmit–receiver (T/R) switch with single-channel radiofrequency (RF) transmitter and receiver, two butterfly-shaped 1 H RF coils, two single-loop 31P RF surface coils and transistor– transistor logic (TTL) controller between the T/R switch and the 31P coils. With the existing single-channel RF transmitter–receiver configuration for X-nuclear application, the TTL switcher toggles the RF transmit power and signal reception between the two 31P coil channels: Channel (or coil) 1 for the detection of 31P signals from the OL, and channel (or coil) 2 for the detection of 31P signals from the FL in human brain. (B) the size and geometry of each coil were determined based on the signal coverage and location of the targeted brain regions. D is the diameter of single-loop 31P surface coils, whereas H, W and L represent the sizes of the butterfly-shaped 1 H coils

supports the dynamic B0 shimming utility for further improving the spectral quality of 31P MRS or CSI acquired in the human FL: a difficult brain region to reach with optimal shimming. This method was validated using a phantom and in human brain.

2 | Methods

All phantom and human experiments were carried out on a Siemens whole-body/90-cm bore, 7-T human scanner (MAGNETOM, Erlangen, Germany) equipped with a single-channel broadband X-nuclear transceiver. In vivo brain 31P–MT MRS experiments were performed on three healthy male volunteers [mean ± standard deviation (SD), 20 ± 1 years], and the human study protocol was approved by the Institutional Review Board of the University of Minnesota. Informed consent was obtained from the participants prior to the MR measurements.

2.1 | Dual-coil 31P MRS system

Figure 1 illustrates the configuration of the dual-coil 31P MRS system consisting of two single-loop 31P surface coils for the acquisition of 31P MRS or CSI from the human OL (Channel 1) and FL (Channel 2); two passively decoupled butterfly-shaped 1 H coils for anatomic MRI and B0 shimming; an X-nuclear transmit–receiver (T/R) switch connecting with a single-channel RF power transmitter (Tx) and a single-channel RF receiver (Rx); and a TTL controller. The size of the single-loop 31P surface coils (~5 cm in diameter) was desired to ensure that the detected 31P signal was dominated from the targeted brain tissue in the OL or FL with an optimized RF pulse flip angle (FA). A home-built TTL controller comprised lumped elements controlled by a digital logic circuitry and a PIN diode. A TTL pulsed signal controlled by the MR console and RF pulse sequence was sent to the TTL controller for toggling the T/R switch (thus, the Tx/Rx connections) between the two 31P surface coils for interleaved RF transmission and acquisition of two 31P FIDs from the OL and FL, respectively, within the same repetition time (TR). After placing the 31P coils at the target brain regions, each coil resonator was tuned and matched separately with minimal mutual interference because of the small coil size and the large distance between the two coils.

The scheme of the RF pulse sequence is designed for the interleaved acquisition of in vivo 31P MR spectra from two brain regions with the option for dynamic B0 shimming (Figure 2). The sequence enables the collection of regional 31P FIDs from the brain regions defined by the RF magnetic field (B1) profile of the 31P surface coil without additional spatial localization, or the acquisition of 3D CSI data by adding 3D phase-encoding gradients between the RF excitation pulse and analog-to-digital converter (ADC) acquisition. Two short TTL trigger pulses were inserted at the beginning of the first and second halves of the TR period, respectively, to toggle the 31P spin excitation and FID detection between the two 31P coils: one (Channel 1) measured the FID from the OL and the other (Channel 2) measured the FID from the FL within the same TR. The acquired 31P FIDs were alternately saved in the same ADC and separated through post-data processing. The B1 profiles of the two 31P surface coils were not electronically coupled

(the isolation was −27 dB between the two coils), and the RF pulse delivered by one 31P coil only affected the targeted brain region. Therefore, there was no signal saturation effect from the RF excitation pulse applied to another 31P coil during the magnetization recovery, and the true TR for each channel's signal acquisition was the same as TR to maximize SNR.

The isolation between the two 1 H coils was −25 dB. The 1 H coils were driven as transceivers with adjustable RF amplitude and phase to optimize the 1 H B1 field and MRI signal intensities. Prior to 31P MRS experiments, using both 1 H coils, global B0 shimming, covering a rectangular box (with an oblique) including both the FL and OL regions, was first carried out with a dual echo in the steady-state MRI pulse sequence in combination with high-order shimming (up to third-order shim). Subsequently, the linear shimming in the x, y and z directions was manually adjusted and optimized only for the

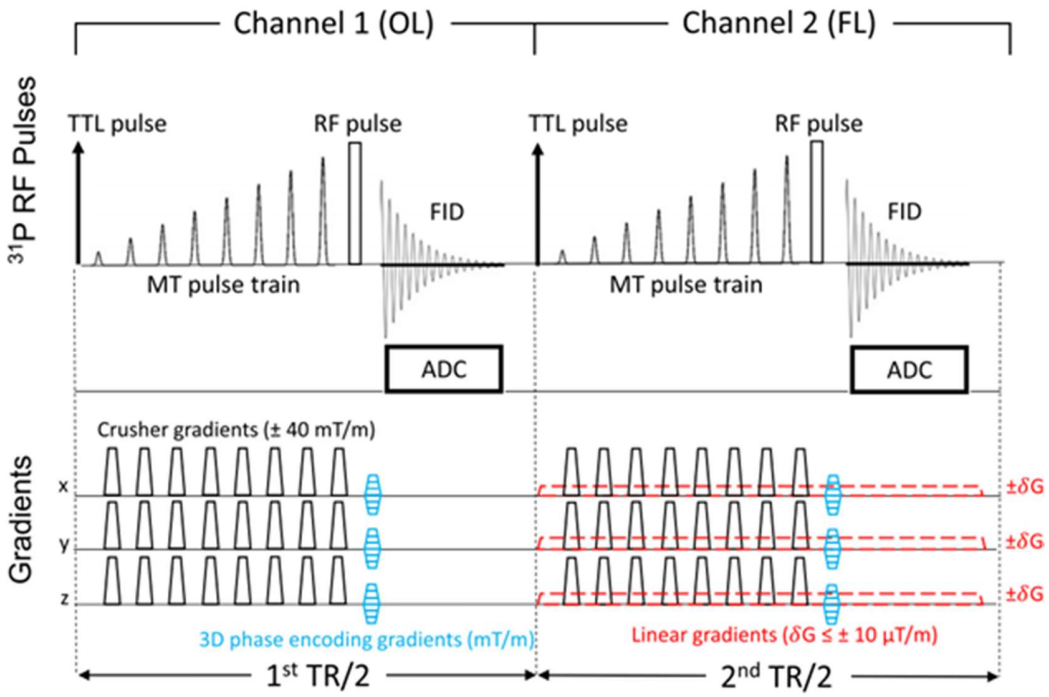

FIGURE 2 Schematic illustration of the dual-coil 31P-MT pulse sequence with 3D-CSI capability. This sequence is designed for acquiring either non-localized MRS FIDs or 3D chemical shift imaging data in the absence or presence of 3D phase encoding gradients, respectively. 31P spectra from two channels are acquired alternatively by switching each RF coil channel at the time of TR/2 by sending the TTL pulse from the MR scanner. For further improving B0 field homogeneity and 31P spectral quality, the adjusted linear gradients are applied to the 2 nd TR to perform dynamic B0 shimming and optimize the 31P spectral quality for the FL. The BISTRO pulse train can be turned on prior to the RF excitation pulse for selectively saturating the γ-ATP resonance and performing the 31P-MT MRS study

FL region using the frontal 1 H RF coil to further improve spectral quality. The first-order shimming values were converted to the linear gradient strengths for before (Gx, Gy, Gz) and after (Gf,x, Gf,y, Gf,z) manual shimming, and the offsets of linear shimming gradients (δGx = Gx–Gf,x, δGy = Gy–Gf,y, δGz = Gz–Gf,z) were turned on throughout the duration of the second half of TR for dynamic shimming and acquisition of optimized 31P FID from the FL (see Figure 2). The carrier frequencies of the RF pulse and receiver were adjusted and optimized for the two 31P coil channels, independently.

2.2 | 31P–MT MRS measurement

A single pulse-acquire sequence was carried out to study cerebral high-energy phosphorus metabolism in the human FL and OL. The 31P–MT MRS technique was implemented using the B1-insensitive selective train to obliterate signal (BISTRO) scheme29 to selectively saturate the γ-ATP resonance [−2.5 ppm from the phosphocreatine (PCr) resonance]. The crusher gradients (isosceles trapezoidal shape; ramp up/down time, 1 ms; top base time, 4 ms; amplitude, 40 mT/m; random order of either positive or negative gradient sign) were inserted between the RF saturation pulses [hyperbolic secant RF pulse waveform; pulse length, 51.2 ms; saturation pulse bandwidth (BW), 160 Hz or 1.3 ppm for 31P MRS at 7 T]. Each BISTRO pulse train consisted of eight RF pulses with varied voltage amplitude and scaling factors of 0.02, 0.04, 0.07, 0.14, 0.27, 0.49, 0.82 and 1, respectively, and the same BISTRO pulse train was repeated three times. The RF pulse power of the BISTRO trains was adjusted for optimal saturation of the γ-ATP resonance. The total magnetization saturation duration was 1.37 s, and the pre-saturation delay time was 1.63 s for each RF coil channel, which could lengthen the TR owing to the manner of the interleaved acquisition. The control spectrum was also acquired in the absence of γ-ATP saturation.

Using a series of RF pulse input voltages, the reference RF power for a nominal 90° excitation pulse FA for each 31P coil was determined by the voltage which reaches the maximum signal intensity of PCr measured under full relaxation conditions (TR = 20 s; FA = 90°; single average; 500-μs hard pulse), and was then reset to achieve an Ernst FA for γ-ATP for the desired TR. The 31P–MT MRS data were acquired alternately from the OL and FL using the following acquisition parameters: TR = 3 s; spectral receiver BW, 5 kHz; excitation (hard) pulse length, 300 μs; Ernst FA, 84.6°; number of complex FID points, 800; number of signal averages, 320.

All 31P–MT spectra were processed using the non-linear least-squares fitting algorithm of AMARES30 employing the jMRUI 5.2 software program30,31 with prior knowledge and fitting constraints including Lorentzian fitting, linewidth (Hz) and chemical shift ranges. Post-processing of the 31P MR spectra included zero filling of FIDs to 2048 data points. A spectral linewidth reported herein was measured in the phase mode after

spectral phase correction, and determined by the full width at half-maximum (FWHM) of the resonance peak without the use of line broadening.

The concentrations of ATP, PCr and inorganic phosphate (Pi) metabolites in the human brain were determined from the control 31P spectra (in the absence of γ-ATP saturation) after correcting a partial saturation factor as a result of the use of a short TR. Absolute concentrations of PCr and Pi were then calibrated using the cerebral ATP concentration of 2.8mM as an internal reference.5 The forward reaction rate constants (kf) under the partially relaxed acquisition condition were calculated according to the following equation: Mc=Ms ≈ 1 þ kfT1 nom (1) where Mc and Ms are the control and γ-ATP-saturated magnetization signals, respectively, and T1 nom is the nominal longitudinal relaxation time (T1) which depends on the intrinsic T1 values of ATP, PCr and Pi at a given magnetic field strength, TR and FA parameters,7,32 and was simulated and determined in this study. The forward reaction fluxes can be calculated using Ff,ATPase = kf,ATPase[Pi]intra for the ATPase reaction and Ff,CK = kf,CK[PCr] for the CK reaction,6,32 where [Pi]intra is the intracellular Pi concentration.

2.3 | pH measurement

The intracellular and extracellular pH values were determined from the chemical shift difference of Pi (δPi) relative to PCr based on the following equation using intracellular Pi (Pi in) and extracellular Pi (Pi ex) resonance signals, respectively33,34: pH ¼ 6:77 þ log10 ð Þ δPi − 3:29 =ð Þ 5:68 − δPi ½

2.4 | 31P CSI measurement

With the application of 3D phase-encoding gradients as shown in Figure 2, 3D 31P CSI was performed to explore the sensitivity of the assessment of brain high-energy phosphate metabolites and to access the signal profile and coverage of the single-loop 31P coils in the FL and OL. The 31P MRS imaging was realized using the 3D Fourier series window (FSW) CSI technique, in which weighted k-space filtering was applied according to the Fourier coefficients for a predetermined voxel shape following an optimum determination of the Fourier series.35 All 31P FSW-CSI data for both RF coil channels were acquired using the same acquisition parameters: TR = 1.2 s; spectral BW, 5 kHz; excitation RF (hard) pulse length, 300 μs; Ernst FA (γ-ATP), 67.1°; field of view, 120 × 120 × 90 mm3 ; 3D phase-encoding step, 7 × 7 × 5; total k-space scan number, 112 per CSI volume; number of complex FID points, 800; number of signal averages, 8. The nominal CSI voxel (3D cylindrical shape) size was 5.3 mL and the total CSI acquisition time was 18 min. Post-processing of the 31P MRS or FSW-CSI voxel spectral data included zero-filling of FIDs to 2048 data points with a line broadening of 10 Hz for SNR enhancement. The PCr and γ-ATP resonance integral images were generated from the 3D

FSW-CSI dataset using a home-built program coded in Matlab v14.0 (MathWorks, Natick, MA, USA). After phase correction of the 31P FSW-CSI voxel spectra in the frequency domain, the integrals of PCr and γ-ATP resonance peaks were estimated and employed to reconstruct high-resolution images and spatial profiles using the established interpolation algorithm, as well as the ratio maps between the PCr and γ-ATP resonance integrals.

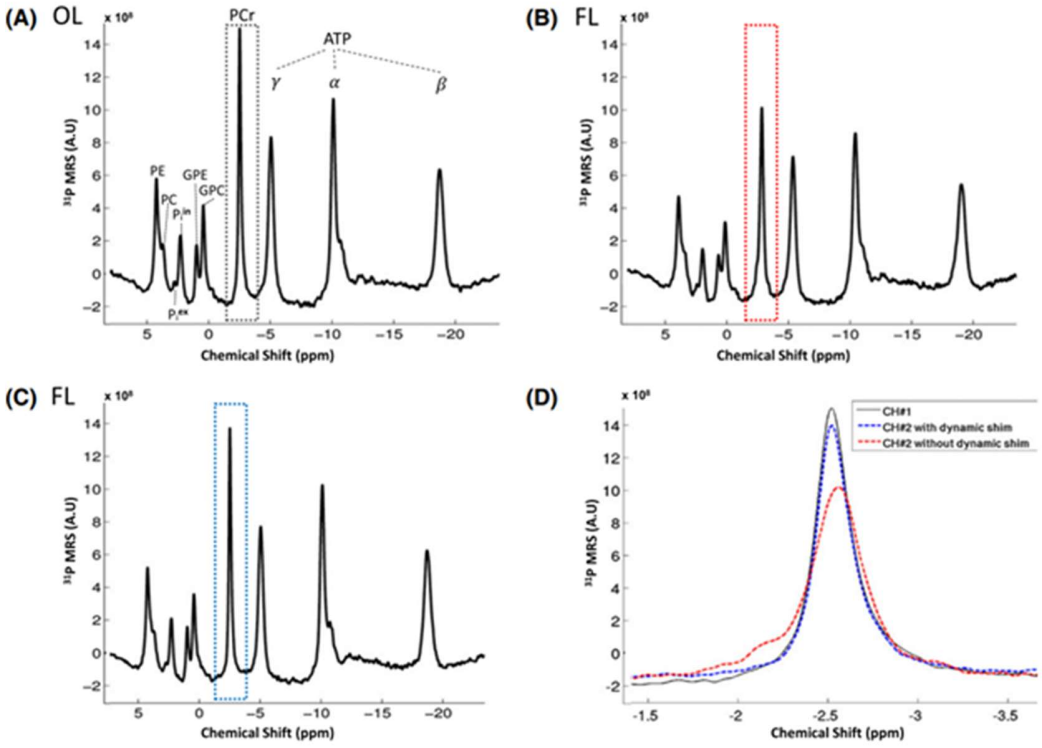

FIGURE 3 Comparison of in vivo 31P spectra (TR = 3 s; 320 signal averages; 16 min of acquisition time per spectrum) in the healthy human brain. In vivo 31P spectra were acquired in the occipital lobe (OL) [A, phosphocreatine (PCr) resonance outlined by the black dotted line] and frontal lobe (FL) with (C, blue dotted line) and without (B, red dotted line) adjustment of the first-order gradients. (D) Comparison of PCr resonance spectral quality shows a significant improvement in the FL using the dynamic B0 shimming approach. ATP, adenosine triphosphate; GPC, glycerophosphocholine; GPE, glycerophosphoethanolamine; PC, phosphocholine; PE, phosphoethanolamine; Piin, intracellular inorganic phosphate; Piex, extracellular inorganic phosphate

3 | Results

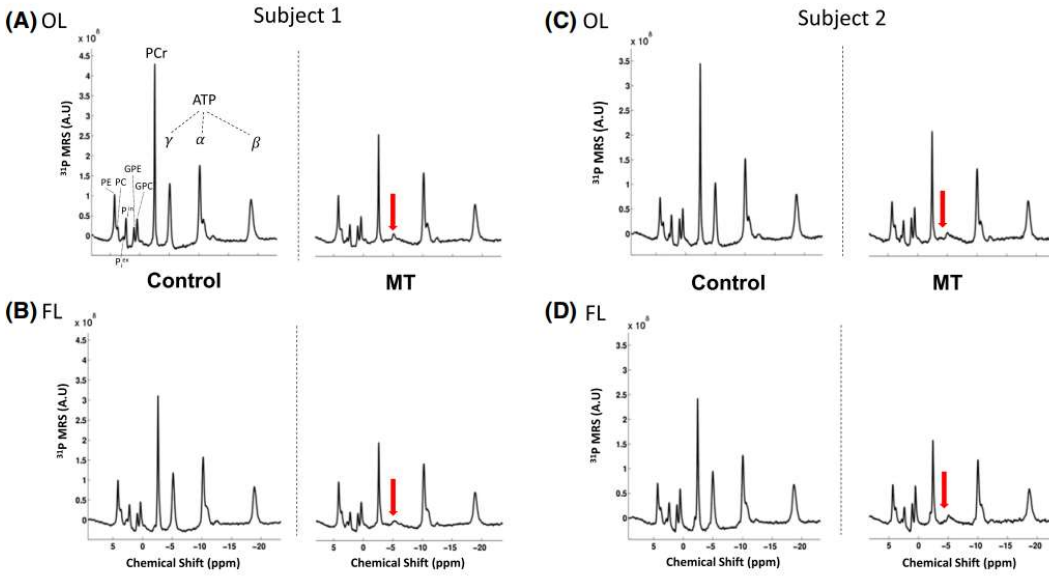

FIGURE 4 Representative in vivo 31P–magnetization transfer (31P–MT) spectra simultaneously detected from the occipital lobe (OL) and frontal lobe (FL) of healthy human subjects. (A, C) 31P control and 31P–MT spectra (with γ-ATP saturation indicated by the red arrows) acquired from the OL. (B, D) 31P control and 31P–MT spectra from the FL. Overall, the 31P magnetic resonance (MR) spectra from the two brain regions show excellent spectral quality and adequate MT saturation efficiency in two representative subjects (TR = 3 s; 320 signal averages; 16 min of acquisition time per spectrum). ATP, adenosine triphosphate; GPC, glycerophosphocholine; GPE, glycerophosphoethanolamine; PC, phosphocholine; PCr, phosphocreatine; PE, phosphoethanolamine; Piin, intracellular inorganic phosphate; Piex, extracellular inorganic phosphate

Figure 3 shows the comparison results of in vivo 31P spectral data from the human OL and FL acquired with and without the use of first-order dynamic B0 shimming at 7 T. In the absence of dynamic B0 shimming, the 31P MR spectrum of the FL showed a broader linewidth and asymmetric shape of PCr resonance (Figure 3B, D), resulting in a relatively low resonance intensity, and thus low SNR (= 100). In contrast, the application of the calibrated offset linear gradients ($\Delta G \leq \pm 10$ μT/m) for optimal B0 shimming of the FL region significantly improved the line shape and narrowed the linewidth (Figure 3C, spectral linewidth or FWHM of PCr = 11.3 Hz or 0.09 ppm at 7 T; SNR = 130), reaching comparable quality of the 31P spectra as in the OL (Figure 3A, FWHM of PCr = 10.1 Hz, SNR = 140) for this representative subject. We also compared the spectral linewidths of 31P spectra acquired from the FL and OL from the same subject, as shown in Figure 3 under two acquisition conditions: dual-coil configuration with dynamic shimming (11.3 Hz in FL and 10.1 Hz in OL) versus regional shimming within the lobe of interest using a

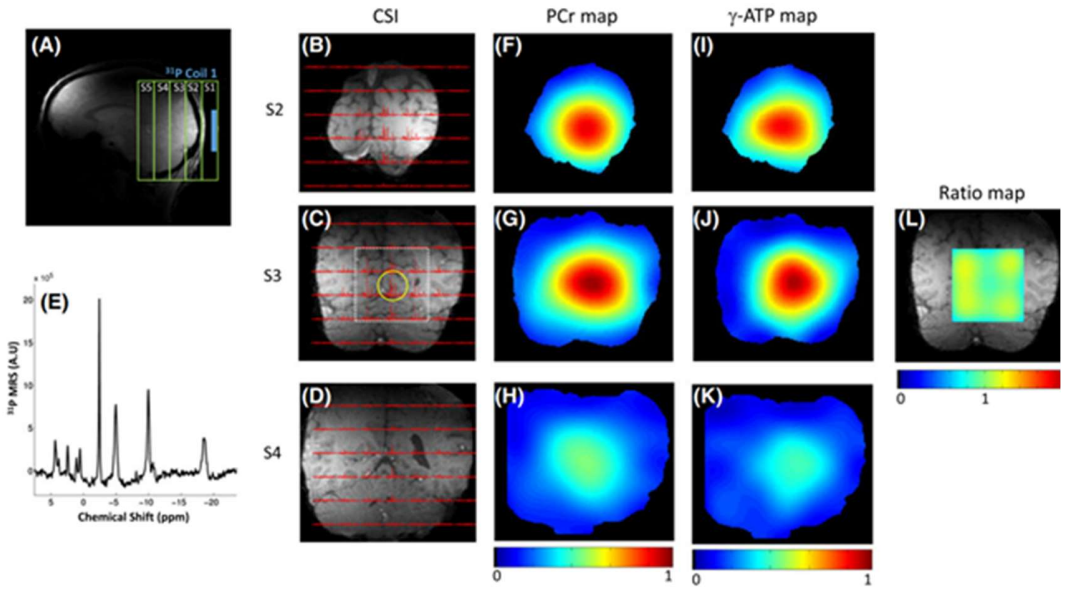

FIGURE 6 Representative in vivo 31P three-dimensional (3D) chemical shift imaging (CSI) data, phosphocreatine (PCr) and γ-adenosine triphosphate (γ-ATP) maps, and their ratio map, from the human occipital lobe (OL) overlaid on the coronal anatomical images. (A) Location of the single-loop 31P coil (channel 1, blue bar) placed near the OL, the field of view and slice positions of the 3D 31P CSI. (B–D) 31P magnetic resonance spectroscopy (MRS) profiles from three selected CSI slices. (E) Single-voxel 31P spectrum denoted by the yellow circle in (C) shows excellent detection sensitivity at the given spatial and temporal resolution. (F–H) corresponding normalized PCr maps (by setting the maximum peak integral of PCr to 1). (I–K) corresponding normalized γ-ATP maps. (L) Ratio map between PCr and γ-ATP in the region of interest (ROI) indicated by the white box in (C). 31P CSI data acquired with a single-loop coil clearly demonstrate a sufficient signal coverage (reaching a depth of approximately 5.4 cm)

traditional single 31P coil approach (10.3 Hz in FL and 9.0 Hz in OL). Therefore, the difference was small (about 1 Hz) between the two-coil (global plus dynamic shimming) and single-coil (optimal shimming focused on a single lobe of interest) configurations. The proposed method provides an effective approach for the interleaved acquisition of 31P spectra from two brain regions with high spectral resolution and quality. Figure 4 displays typical in vivo 31P–MT spectra in the absence (control) and presence of γ-ATP saturation (i.e. MT) preparation (indicated by red arrows) acquired from the human OL (Figure 4A, C) and FL (Figure 4B, D) from two representative subjects. Overall, in vivo 31P control spectra showed excellent quality and high sensitivity, allowing for the reliable detection and quantification of the PCr, ATP, Pi and other phosphorus metabolite signals in healthy human brains. The 31P–MT spectra with γ-ATP saturation indicated

sufficient saturation efficiency at given MT preparation duration with optimal RF saturation powers for each 31P RF coil channel. The PCr concentrations measured in the OL and FL were 4.12 ± 0.11mM and 4.08 ± 0.21mM, respectively. The Pi in concentrations for the OL and FL were 1.05 ± 0.04mM and 0.94 ± 0.05mM, respectively, and the corresponding Piex concentrations were 0.34 ± 0.01mM and 0.40 ± 0.03mM, respectively, after the correction of the T1 saturation effect for PCr (apparent T1 = 3.37 s) and Pi (apparent T1 = 3.19 s).36 Under partially relaxed acquisition conditions at a given nominal excitation RF pulse FA and TR, estimated T1 nom values for PCr and Pi in were 1.91 s and 1.55 s, which were determined by the slopes of the solid lines in Figure 5. The forward rate constants of kf,CK (for the PCr → ATP reaction) were 0.389 ± 0.002 s−1 and 0.32 ± 0.01 s−1 for OL and FL, respectively, which are in good agreement with previously reported values.32 The forward rate constants of kf,ATP (for the Pi → ATP reaction) were 0.14 ± 0.06 s−1 for OL and 0.18 ± 0.02 s−1 for FL. Accordingly, the forward CK reaction fluxes were 87.5 ± 1.7 μmol/g/min and 71.9 ± 1.6 μmol/g/min, and the forward ATPase reaction fluxes were 8.1 ± 3.7 μmol/g/min and 9.4 ± 1.3 μmol/g/min, for OL and FL, respectively, after unit conversion using a brain tissue density of 1.1 g/mL.6 The measured intracellular pH was 7.03 ± 0.01 for OL and FL, and the pH result is consistent with the value of 7.03 in human gray matter- dominated brain regions.19 The extracellular pH was 7.45 ± 0.04 and 7.47 ± 0.01 for OL and FL, respectively. Figure 6 displays the in vivo 3D 31P CSI results from three representative image slices (Figure 6B–D; in coronal orientation) detected in the OL from one subject, and the corresponding maps of PCr (Figure 6F–H) and γ-ATP (Figure 6I–K) resonance integrals. The large integral variation reflects the inhomogeneous B1 and signal intensity profiles of the 31P surface coil. In contrast, the ratio map between the PCr and γ-ATP integrals shows relatively uniform distribution in the

central brain region covered by the surface coil, even without the correction of the relaxation saturation effect because of the lack of information regarding the spatial distribution of RF pulse FA in this study. Figure 7 shows similar results detected in the FL from the same subject. Given the proximity of the 31P RF coils, each 31P CSI showed a sufficient signal coverage and excellent detection sensitivity for the desired cortical lobes without signal overlapping between the two 31P coils. In conjunction with the linear dynamic B0 shimming, in vivo 31P spectra taken from representative CSI voxels indicate comparable spectral quality with narrow resonance linewidth and excellent SNR for both the OL (Figure 6E, SNR = 60) and FL (Figure 7E, SNR = 45). Although the two 31P coils employed in this study had the same coil design and size, the coil planes to conform the human head shape were different between the FL and OL. The OL 31P coil plane was approximately parallel to the B0 direction (or z axis, see Figure 6) and produced an optimal distribution of the B1 field (i.e. the transverse magnetic field component Bxy) for coverage of the OL. In contrast, the FL 31P coil plane was slightly tilted from the z axis for most subjects in order to conform the front head shape (see

Figure 7), resulting in a reduction in Bxy (accompanied by an increase in Bz), thus reducing the detection sensitivity and 31P signal in the FL. The degree of signal reduction varied between subjects depending on the front head shape and RF coil setup.

4 | Discussions

We have demonstrated a novel design of dual-coil 31P MRS system for the interleaved measurement and imaging of regional high-energy phosphorus metabolism in two human brain regions of interest. Using an existing single-channel X-nuclear RF transmit amplifier and receiver, 31P MRS data were successfully collected from the FL and OL within the same TR, providing a time-efficient way to reduce the total acquisition time by half compared with the single acquisition approach for two brain regions, and thus to improve the SNR by the square root of 2. Notably, with further adjustment of the linear gradients for dynamic shimming, the in vivo 31P spectrum of the frontal brain region showed high quality with better spectral line shape compared with that without adjustment. This enables the reliable assessment and quantification of cerebral phosphorus metabolites in the FL, which plays an essential role in high cognitive brain function. In addition, the 3D 31P CSI results demonstrate sufficient signal coverage and good B0 homogeneity achieved with the dual-coil 31P MRS system, resulting in excellent spectral quality and phosphate metabolite images in two distinct brain regions. As mentioned above, the putative presence of complex neurological symptoms commonly linked to neurodegenerative diseases has prompted the need for the re-evaluation of classic diagnostic/treatment approaches to neurodegenerative disease. For instance, there has been a strong association between the clinical manifestations of motor restlessness in the upper motor system and cognitive impairments in the frontal areas in amyotrophic lateral sclerosis.12,13 In addition, the central viewpoint of upper motor dysfunction in Parkinson's disease has been revised because of frequent reports of non-motor symptoms encompassing cognitive dysfunction in the frontal lobe14,16 and visual dysfunction in the OL.37,38 In this regard, the method proposed in this work, capable of simultaneous assessment of the bioenergetic abnormalities in the target brain regions of interest, could provide insights into the pathophysiology underlying neurodegenerative diseases. Detection sensitivity or SNR is essential for in vivo MRS measurement as it significantly influences the accuracy and precision for the assessment and quantification of cerebral metabolites, not only for X-nuclei, but also 1 H MRS.39-42 Moreover, low concentrations (a few millimoles) of phosphate metabolites in the human brain are challenging to the achievement of high spatial or temporal resolution of 31P MRS imaging. Given the known lower sensitivity of the RF volume coil, in vivo 31P MRS with the application of two single-loop 31P surface coils in the present work shows higher detection sensitivity and excellent SNR in the desired cortical regions of interest in the human brain at 7 T; thus, it could provide a valuable solution to address scientific questions demanding high SNR or imaging spatial resolution in the cortical regions of interest. The lack of physical proximity between the two RF surface coils inherently minimizes unwanted interactions between the brain regions and allows for discrete acquisition of in vivo 31P MRS data with comparable spectral quality within the same

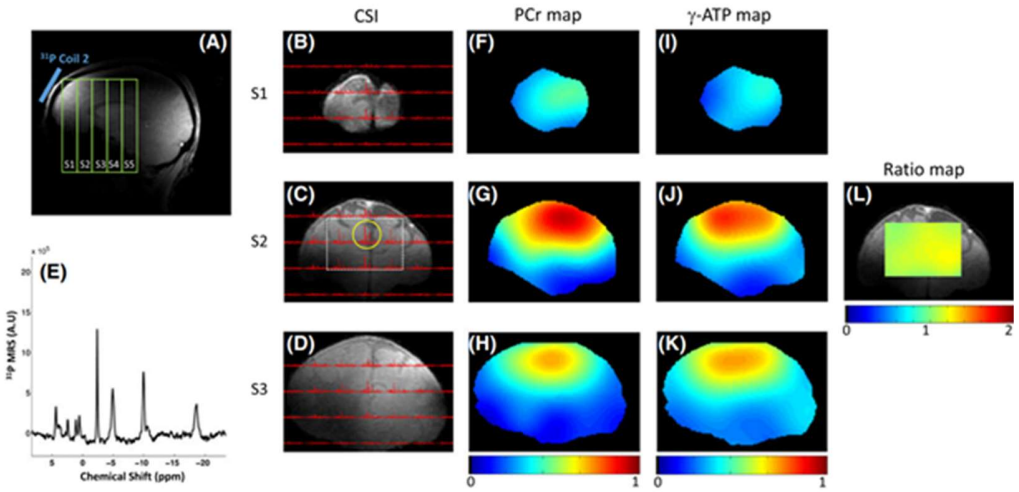

FIGURE 7 Representative in vivo 31P three-dimensional (3D) chemical shift imaging (CSI) data, phosphocreatine (PCr) and γ-adenosine triphosphate (γ-ATP) maps, and their ratio map, from the human frontal lobe (FL) overlaid on the coronal anatomical images. (A) Location of the single-loop 31P coil (channel 2, blue bar) placed near the FL, the field of view and slice positions of the 3D 31P CSI. (B–D) 31P magnetic resonance spectroscopy (MRS) profiles from three selected CSI slices. (E) with dynamic B0 shimming, the single-voxel 31P MR spectrum [yellow circle in (C)] shows excellent spectral quality and detection sensitivity. (F–H) corresponding normalized PCr maps. (I–K) corresponding normalized γ-ATP maps. (L) Ratio map between PCr and γ-ATP in the region of interest indicated by the white box in (C). 3D 31P CSI data demonstrate that the brain region with the highest signal detected by the 31P coil was approximately 2.5 cm from the surface of the FL (slice 2), which covers critical brain regions including the medial frontal gyrus and cingulate gyrus

sampling time. Accordingly, the combination of the dual 31P surface coils with the CSI method, as demonstrated here, provides considerable potential for further investigation of the correlation of high- energy phosphorus metabolism between different human brain regions, or for functional imaging of neuroenergetic changes between rest and activated brain states with rich matrices of physiological measures, including the high-energy phosphorus metabolites of ATP and PCr, Ff,ATPase and Ff, CK, intra- and extracellular pH, intracellular free [Mg2+] and metabolic precursors of phosphorus lipid metabolism. Homogenization of the B0 field is an essential prerequisite for the enhancement of spectral quality and resolution for all in vivo MRS applications. For this reason, several advanced B0 shimming techniques have been proposed.25-28 Despite the substantial improvement in B0 homogeneity, the availability of these methods is still limited in most conventional MR scanners. In addition, the current state-of-the-art technology employing either multiple-channel receivers or transceivers acquires FIDs from multiple RF receiver

coils at the same time, and thus it is difficult to perform alternate and dynamic B0 shimming for individual RF coils at a different time within a single TR period. Most conventional MR systems, including the scanner employed in this study, do not allow real-time updating of high-order shim currents owing to the eddy currents induced by fast switching shim currents and slow decays, leading to the degradation of spectral quality. The present study was limited to first-order dynamic shimming using linear gradients. Nevertheless, the concept of alternative B0 shimming amongst multiple RF coils within the same TR is not limited to the first-order shim, and can be incorporated with other advanced dynamic shimming techniques, enabling first-order and higher order dynamic shimming. Early attempts at dynamic shimming showed the improved image quality when updating the linear shim terms dynamically in multi-slice imaging acquisition,43,44 as well as in single-voxel 1 H MRS.45 We implemented this approach by adjusting the linear gradients for first-order shimming of the FL region, providing perceptible improved quality of in vivo 31P spectra in the FL, comparable with that of the OL, which is less problematic for achieving satisfactory B0 shimming. However, two different shimming offsets could be readily incorporated into the pulse sequence (Figure 2) and employed alternately to the two 31P coils for further improvement of the spectral resolution in both brain regions. In principle, in vivo MR spectra from multiple voxels could be acquired using a large (or volume) RF coil in combination with a single-voxel localization MRS method [e.g. image-selected in vivo spectroscopy (ISIS),46 point-resolved spectroscopy (PRESS)47 or stimulated echo acquisition mode (STEAM)48] and the option of dynamic shimming if the selected voxels are not spatially overlapped in a Cartesian coordinate system. Therefore, this approach is limited only to the oblique arrangement of multiple voxels and is not suitable if one is interested (for instance, as investigated in the present study) in the human FL and OL, which are aligned on the same sagittal plane. Although the voxel localization using multiple frequency- selective RF pulses could not be spatially overlapped between multiple voxels, the RF power delivered from all RF pulses employed to acquire multiple voxels will be absorbed by all brain regions covered by the RF coil. The average specific absorption rate (SAR) in brain tissue will increase significantly (approximately equals the product of the voxel number and the SAR required to collect single-voxel MRS), thus, pose a safety concern, especially at ultrahigh fields.

5 | Conclusion

We have demonstrated that the new dual-coil 31P MRS approach described in this work could offer a cost-effective and time-efficient solution for interleaved in vivo 31P MRS measurements and imaging from multiple desired brain regions based on an existing single-channel transmitter– receiver configuration with optimal SNR and spectral resolution. It could provide a valuable metabolic imaging tool for the examination of cerebral energy metabolism in healthy subjects and impairments in patients in desired and multiple brain regions. Moreover, the same approach and design can be: (1) extended to more than two RF coil channels, thus covering more brain regions; (2) adapted to other X-nuclei or 1 H MRS; and (3) potentially used for functional MRI studies from multiple brain regions of interest with higher sensitivity and spatiotemporal resolution.

ACKNOWLEDGEMENTS

This work was supported in part by National Institutes of Health (NIH) grants (R01 NS070839 and MH111447, R24 MH106049 and MH106049S1, S10RR026783, P41 EB015894 and P30 NS057091) and the AHC Faculty Research Development (FRD) grant from the University of Minnesota.

References

1. Ackerman JJ, Grove TH, Wong GG, Gadian DG, Radda GK. Mapping of metabolites in whole animals by 31P NMR using surface coils. Nature. 1980;283(5743):167-170.
2. Bottomley PA, Charles HC, Roemer PB, et al. Human in vivo phosphate metabolite imaging with 31P NMR. Magn Reson Med. 1988;7(3):319-336.
3. Bottomley PA, Hardy CJ. Rapid, reliable in vivo assays of human phosphate metabolites by nuclear magnetic resonance. Clin Chem. 1989;35(3):392-395.
4. Du F, Cooper A, Lukas SE, Cohen BM, Ongur D. Creatine kinase and ATP synthase reaction rates in human frontal lobe measured by 31P magnetization transfer spectroscopy at 4T. Magn Reson Imaging. 2013;31(1):102-108.
5. Zhu XH, Lu M, Lee BY, Ugurbil K, Chen W. In vivo NAD assay reveals the intracellular NAD contents and redox state in healthy human brain and their age dependences. Proc Natl Acad Sci U S A. 2015;112(9):2876-2881.
6. Lei H, Ugurbil K, Chen W. Measurement of unidirectional pi to ATP flux in human visual cortex at 7 T by using in vivo 31P magnetic resonance spectroscopy. Proc Natl Acad Sci U S A. 2003;100(24):14409-14414.
7. Xiong Q, Du F, Zhu X, et al. ATP production rate via creatine kinase or ATP synthase in vivo: a novel superfast magnetization saturation transfer method. Circ Res. 2011;108(6):653-663.
8. Du F, Zhu XH, Zhang Y, et al. Tightly coupled brain activity and cerebral ATP metabolic rate. Proc Natl Acad Sci U S A. 2008;105(17):6409-6414.
9. Du F, Cooper AJ, Thida T, et al. In Vivo evidence for cerebral bioenergetic abnormalities in schizophrenia measured using 31P magnetization transfer spectroscopy. JAMA Psychiat. 2014;71(1):19-27.
10. Bottomley PA, Cousins JP, Pendrey DL, et al. Alzheimer dementia: quantification of energy metabolism and mobile phosphoesters with P-31 NMR spectroscopy. Radiology. 1992;183(3):695-699.
11. Smith CD, Pettigrew LC, Avison MJ, et al. Frontal lobe phosphorus metabolism and neuropsychological function in aging and in Alzheimer's disease. Ann Neurol. 1995;38(2):194-201.
12. Ferrari R, Kapogiannis D, Huey ED, Momeni PFTD. ALS: a tale of two diseases. Curr Alzheimer Res. 2011;8(3):273-294.
13. Phukan J, Elamin M, Bede P, et al. The syndrome of cognitive impairment in amyotrophic lateral sclerosis: a population-based study. J Neurol Neurosurg Psychiatry. 2012;83(1):102-108.
14. Taylor AE, Saint-Cyr JA, Lang AE. Frontal lobe dysfunction in Parkinson's disease. The cortical focus of neostriatal outflow. Brain. 1986;109(Pt 5):845-883.

15. Weil RS, Schrag AE, Warren JD, Crutch SJ, Lees AJ, Morris HR. Visual dysfunction in Parkinson's disease. Brain. 2016;139(11):2827-2843.
16. Lewis SJ, Dove A, Robbins TW, Barker RA, Owen AM. Cognitive impairments in early Parkinson's disease are accompanied by reductions in activity in frontostriatal neural circuitry. J Neurosci. 2003;23(15):6351-6356.
17. Zhang XL, Zhu XH, Qiao HY, et al. A circular-polarized double-tuned (31P and 1 H) TEM coil for human head MRI/MRS at 7T. Proceedings of the 11th Annual Meeting ISMRM, p. 423, Toronto, ON, Canada, 2003.
18. Avdievich NI, Hetherington HP. 4 T actively-detuneable double-tuned 1 H/31P head volume coil and four-channel 31P phased array for human brain spectroscopy. J Magn Reson. 2007;186(2):341-346.
19. Zhu XH, Qiao H, Du F, et al. Quantitative imaging of energy expenditure in human brain. Neuroimage. 2012;60(4):2107-2117.
20. Lee RF, Giaquinto R, Constantinides C, Souza S, Weiss RG, Bottomley PA. A Broadband phased-array system for direct phosphorus and sodium metabolic MRI on a clinical scanner. Magn Reson Med. 2000;43(2):269-277.
21. Hardy CJ, Bottomley PA, Rohling KW, Roemer PB. An NMR Phased array for human cardiac 31P spectroscopy. Magn Reson Med. 1992;28(1):54-64.
22. Avdievich NI. Transceiver-phased arrays for human brain studies at 7 T. Appl Magn Reson. 2011;41(2–4):483-506.
23. Mirkes C, Shajan G, Chadzynski G, Buckenmaier K, Bender B, Scheffler K. 31P CSI of the human brain in healthy subjects and tumor patients at 9.4 T with a three-layered multi-nuclear coil: initial results. MAGMA. 2016;29(3):579-589.
24. Juchem C, de Graaf RA. B0 magnetic field homogeneity and shimming for in vivo magnetic resonance spectroscopy. Anal Biochem. 2017;529:17-29.
25. Juchem C, Nixon TW, McIntyre S, Boer VO, Rothman DL, de Graaf RA. Dynamic multi-coil shimming of the human brain at 7 T. J Magn Reson. 2011;212(2):280-288.
26. Stockmann JP, Witzel T, Keil B, et al. A 32-channel combined RF and B0 shim array for 3T brain imaging. Magn Reson Med. 2016;75(1):441-451.
27. Darnell D, Truong TK, Song AW. Integrated parallel reception, excitation, and shimming (iPRES) with multiple shim loops per radio-frequency coil element for improved B0 shimming. Magn Reson Med. 2017;77(5):2077-2086.
28. Pan JW, Lo KM, Hetherington HP. Role of very high order and degree B0 shimming for spectroscopic imaging of the human brain at 7 tesla. Magn Reson Med. 2012;68(4):1007-1017.
29. de Graaf RA, Luo Y, Garwood M, Nicolay K. B1-insensitive, single-shot localization and water suppression. J Magn Reson B. 1996;113(1):35-45.

30. Vanhamme L, van den Boogaart A, Van Huffel S. Improved method for accurate and efficient quantification of MRS data with use of prior knowledge. J Magn Reson. 1997;129(1):35-43.
31. Naressi A, Couturier C, Castang I, de Beer R, Graveron-Demilly D. Java-based graphical user interface for MRUI, a software package for quantitation of in vivo/medical magnetic resonance spectroscopy signals. Comput Biol Med. 2001;31(4):269-286.
32. Du F, Zhu XH, Qiao H, Zhang X, Chen W. Efficient in vivo 31P magnetization transfer approach for noninvasively determining multiple kinetic parameters and metabolic fluxes of ATP metabolism in the human brain. Magn Reson Med. 2007;57(1):103-114.
33. Petroff OA, Prichard JW, Behar KL, Alger JR, den Hollander JA, Shulman RG. Cerebral intracellular pH by 31P nuclear magnetic resonance spectroscopy. Neurology. 1985;35(6):781-788.
34. Patel N, Forton DM, Coutts GA, Thomas HC, Taylor-Robinson SD. Intracellular pH measurements of the whole head and the basal ganglia in chronic liver disease: a phosphorus-31 MR spectroscopy study. Metab Brain Dis. 2000;15(3):223-240.
35. Hendrich K, Hu X, Menon RS, et al. Spectroscopic imaging of circular voxels with a two-dimensional Fourier-series window technique. J Magn Reson B. 1994;105(3):225-232.
36. Lei H, Zhu XH, Zhang XL, Ugurbil K, Chen W. In vivo 31P magnetic resonance spectroscopy of human brain at 7 T: an initial experience. Magn Reson Med. 2003;49(2):199-205.
37. Davidsdottir S, Cronin-Golomb A, Lee A. Visual and spatial symptoms in Parkinson's disease. Vision Res. 2005;45(10):1285-1296.

Chapter 4

Comparison of 16-channel human head Mono-Dipole arrays vs. 16-channel Monopole + HDC Dipole arrays (8-channel monopole arrays + 8-channel high dielectric constant (HDC) dipole arrays) at 10.5T

Presented at

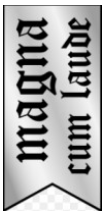

Myung Kyun Woo , Lance DelaBarre , Jerahmie Radder , Russell Lagore , Yigitcan Eryaman , Kamil Ugurbil , and Gregor Adriany, “Comparison of a 16-channel monopole/dipole hybrid array with a combined 8-channel monopole + 8-channel high dielectric constant (HDC) disk dipole array for head imaging at 10.5T”, 26th ISMRM meeting, Paris, France, 16-21 June, 2018. [Power pitch #0024] – Magna cum laude

1 | Introduction

As a transmitter, 16-channel dipole head arrays is desirable above 7T, however, it is difficult to achieve this high channel count due to coupling [1-3]. Also, shortening the length of dipole is required for the human head applications [4, 5]. Here we explore performance of two new types of array coil designs based on dipole and monopole antenna arrays. The first type is circumscribing 16-channel Mono-Dipole arrays and the other type is 16-channel Monopole + HDC Dipole arrays which is an arrays combination consisting of 8-channel monopole antenna arrays with 8-channel dipole arrays with high dielectric constant (HDC) materials [6]. To investigate this, we first compared 8-channel dipole arrays, monopole arrays, and Mono-dipole head arrays in simulation and later verified those by experiment. Then we compare arrays of 16-channel Mono-dipole, 16-channel Monopole + HDC Dipole arrays and 16-channel closer fitting stripline for achievable B_1^+ field efficiency at 10.5T.

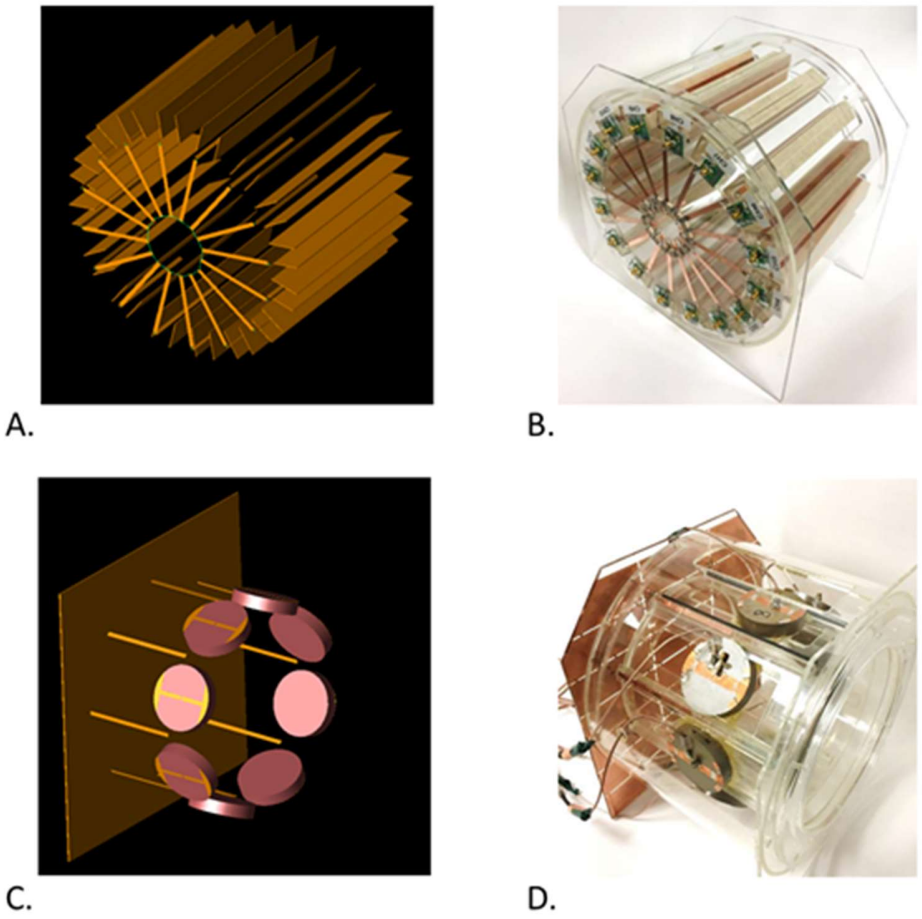

Figure 1. A, B : Schematics and Picture of the 16-channel Mono-Dipole array. C, D: Schematics and Picture of the 16-channel Monopole + HDC Dipole array (an 8-channel Monopole array + an 8-channel HDC Dipole array)

2 | Methods

Schematics and pictures of the 16-channel transceiver head arrays are shown in Fig. 1. The 16-channel Mono-Dipole arrays (Inner diameter (ID): 24 cm and length of each poles: 12 cm) has sixteen equally spaced dipole antennas, and one leg of each dipole antenna was effectively shortened to a common ground using 680 pF capacitors. Two floating copper shields (Shields dimension: 3.5 x 22 cm^2) were placed between one of the poles of the antenna along the z-direction to support an extension in longitudinal coverage [7]. Each shield was spaced 1 cm away from the center of the pole and placed 2cm away from the feed point. Floating cable traps were used to suppress the cable sheet currents [8].

For the 16-channel Monopole + HDC Dipole arrays (ID: 24 cm and monopole length: 12 cm), the longitudinal coverage was extended with a dual row type approach by combining 8-channel monopole arrays with 8-channel HDC (Dipole length: 8 cm and End loaded: 1.5 cm) dipole arrays. The HDC (σ= 0.0031 S/m and ε_r = 101.05) dipole arrays were placed 22.5° shifted from the monopoles and the z-directional gap between the HDC dipoles and the monopole ground plane was 10cm.

The 10.5T / 88 cm whole-body magnet (Agilent, Santa Clara, CA) and gradient (SC72, Siemens Healthcare, Erlangen, DE) was combined with 16 channel RF transmitters. Noise correlation matrices were obtained to evaluate crosstalk between elements (Fig. 2).

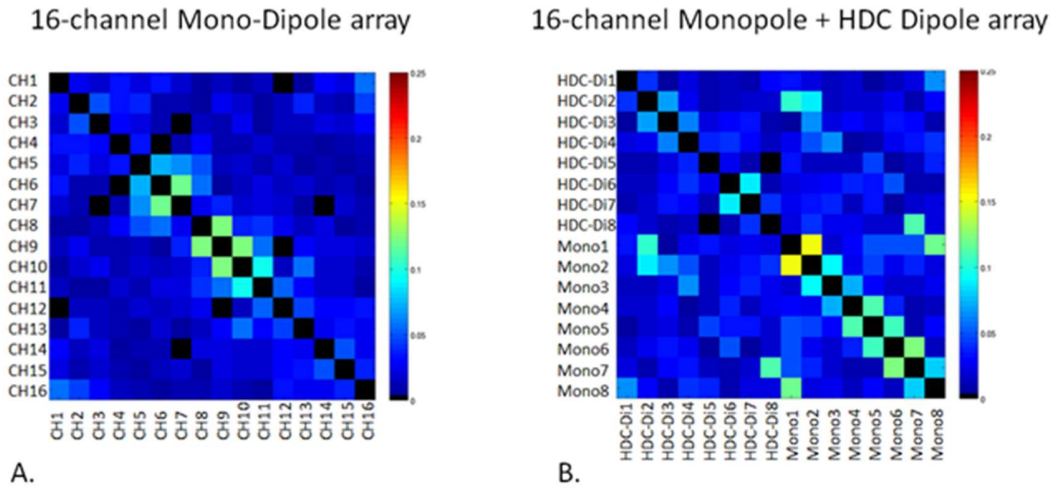

Figure 2. Noise correlation matrix of A: 16-channel Mono-Dipole arrays and B: 16-channel Monopole + HDC Dipole array (an 8-channel Monopole arrays + an 8-channel HDC Dipole array). The 16-channel Mono-Dipole array shows excellent correlation values (less than 0.12) regardless of close distance (2cm) among elements. For the 16-channel Monopole + HDC Dipole array, low correlation (less than 0.08) is observed between 8-channel HDC dipoles (Distance between elements: 6.5cm) , however, relatively high correlation (less than 0.15) is observed between monopoles. (Distance between elements: 8cm)

Transmit B_1^+ profiles were obtained using an actual flip angle imaging (AFI) sequence for a cylindrical phantom (Diameter: 17 cm and Height: 30.5 cm). The phantom has uniform electrical properties (σ= 0.6 S/m and ε_r = 49).

Electromagnetic simulation (XFdtd; REMCOM, State College, PA) was performed to calculate the B_1^+ field (normalized to 1 W). The B_1^+ efficiency was initially compared with 8-channel arrays of dipoles, monopoles, and Mono-Dipole (Fig. 3). A phantom with matching dimension and electrical properties was selected for experimental verification with a 2 x 2 x 2 mm^3 resolution. Fig. 4 shows the experimental results of the comparison between the arrays of 16-channel Mono-dipole, the 16-channel Monopole + HDC Dipole and 16-channel stripline.

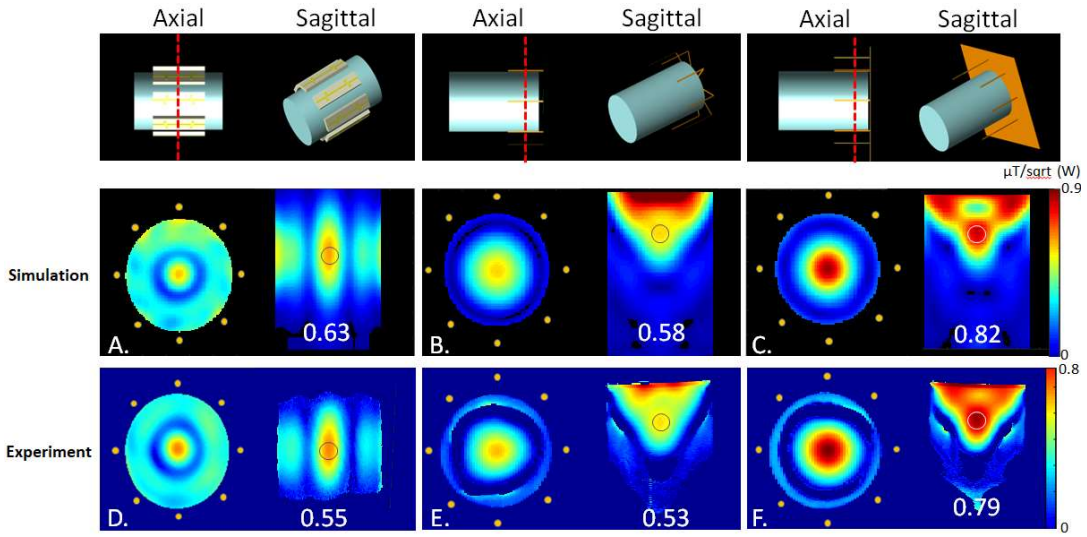

Figure 3. Simulation and Experimental B_1^+ maps of 8-channel Dipole array (Inner diameter: 19 cm) with teflon blocks (ε_r = 2.2), 8-channel Mono-Dipole array (Inner diameter: 24 cm) and 8-channel Monopole array (Inner diameter: 24 cm): Simulation data set of the axial and sagittal plane A: 8-channel Dipole array, B: 8-channel Mono-Dipole array, and C: 8-channel Monopole array. Experimental data set of the axial and transverse plane D: 8-channel Dipole array, E: 8-channel Mono-Dipole array, and F: 8-channel Monopole array.

3 | Results and Discussions

The 16-channel Mono-Dipole arrays consistently showed excellent decoupling as indicated in Fig. 2, on the order of ~10-14 dB between neighboring elements. Excellent agreement between simulation and experiment ~10% was achieved for the highest B_1^+ values among the 8-channel dipole, monopole and the Mono-Dipole arrays. From AFI imaging, the transmit efficiency of stripline (0.5 μT/sqrt (W)) was higher compared to Mono-dipole (0.3 μT/sqrt (W)). We attribute this difference in achievable B_1^+ in part to the fact that the dimension of stripline has 20% smaller area than the Mono-dipole. And without the floating shields to expand the coverage, the field of view is narrowed, but the efficiency improves and is similar to that of the stripline. For the 16-channel Monopole + HDC Dipole arrays, B_1^+ efficiency (0.45 μT/sqrt (W)) is higher than the 16-channel Mono-dipole head arrays, however, this value is lower than the 8-channel monopole arrays (0.7 μT/sqrt (W)).

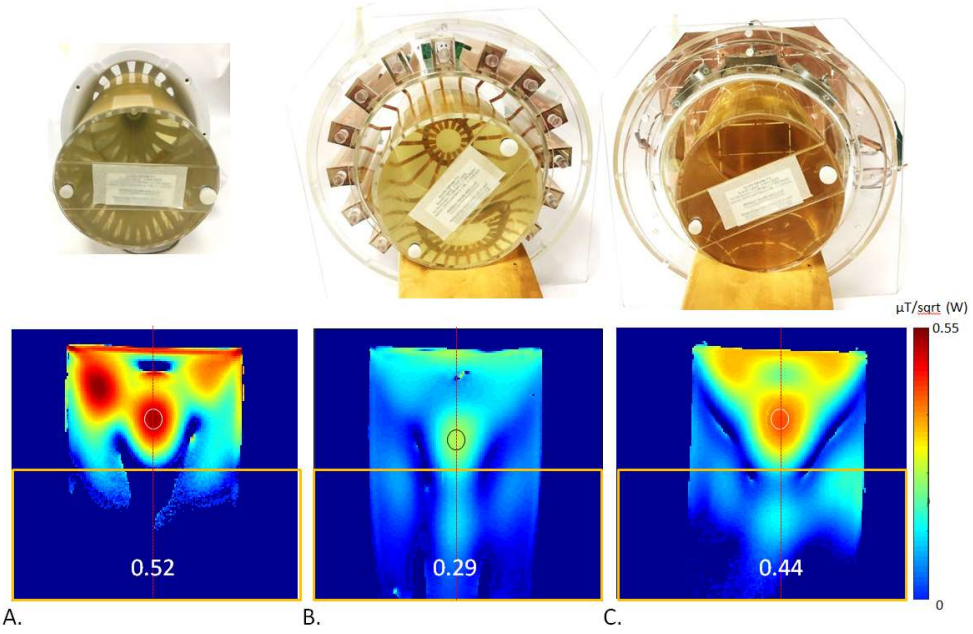

Figure 4. Experimental B_1^+ maps of A: 16-channel stripline array, B: 16-channel Mono-Dipole array, and C: 16-channel Monopole + HDC Dipole array (an 8-channel monopole array + an 8-channel HDC dipole array) on the axial and transverse plane. The profile of red line is indicated on Figure 5. Yellow boxes indicate the increased coverage for human head imaging.

4 | Conclusion

For head applications, it is difficult to achieve sufficient dipole decoupling because the dipoles couple less to tissue. To connect one pole of each dipole, we effectively created a radial ground plane resulting in 16-channel Mono-Dipole arrays. Improved decoupling among the channels is observed in the Mono-dipole arrays. We observed that 16-channel Mono-dipole head antenna arrays have potential advantages for whole head cover at 10.5T. For the 16-channel Monopole + HDC Dipole arrays, phase shimming between monopole and HDC dipole is required for the optimized results. We also plan to evaluate 16-channel Monopole + HDC dipole arrays for the potential improvement.

Acknowledgements

NIH- U01 EB025144 S10 RR026783, BTRC P41 EB015894, P30 NS076408 and WM Keck Foundation

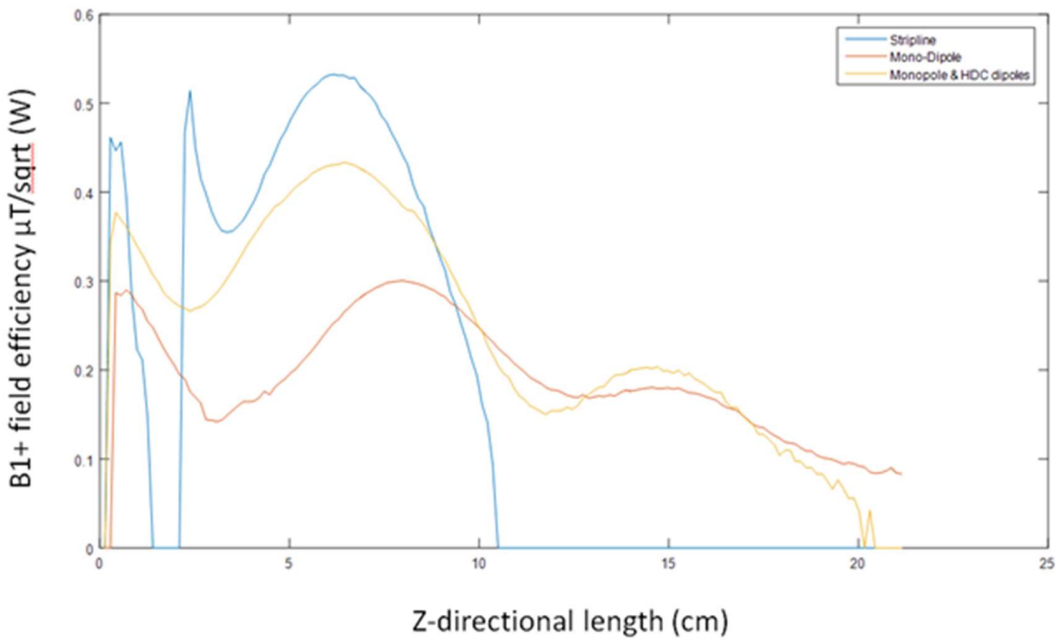

Figure 5. B_1^+ field profile of the 16-channel Mono-Dipole array, the 16-channel Monopole + HDC Dipole array (an 8-channel Monopole array + an 8-channel HDC Dipole array) and the 16-channel stripline array.

References

1 Ian Robert Oliphant Connell, Ravi S Menon. Decoupling and Integration of Electric Dipoles into RF Arrays. In Proceedings of the 25th Annual Meeting of ISMRM, Honolulu, 2017. p. 4295

2 Kyle M Gilbert, Joseph S Gati, L Martyn Klassen, Stefan Everling, Ravi S Menon. Fifteen-channel receive coil for high acceleration rates in UHF marmoset imaging. In Proceedings of the 25th Annual Meeting of ISMRM, Honolulu, 2017. p. 2661

3 Riccardo Lattanzi, Graham C. Wiggins, Bei Zhang, Qi Duan , Ryan Brown, Daniel K. Sodickson. Approaching Ultimate Intrinsic Signal-to-Noise Ratio With Loop and Dipole Antennas. Magn Reson Med DOI: 10.1002/mrm.26803, 2017

4 Gang Chen, Christopher M. Collins, Daniel K. Sodickson, and Graham C. Wiggins. A Method to Assess the Loss of a Dipole Antenna for Ultra-High-Field MRI. Magn Reson Med DOI 10.1002/mrm.26777, 2017

5 Gang Chen, Martijn Cloos, Daniel Sodickson, Graham Wiggins. A 7T 8 channel transmit-receive dipole array for head imaging: dipole element and coil evaluation. In Proceedings of the Joint Annual Meeting of ISMRM-ESMRMB, Milan, 2014. p. 621

6 Russell L Lagore, Lance DelaBarre, Qing X Yang, Michael Lanagan, Yigitcan Eryaman, Sebastian Rupprecht, Wei Luo, Byeong-Yeul Lee, Xiao-Hong Zhu, Kamil Ugurbil, Wei Chen, Gregor Adriany. In Proceedings of the 25th Annual Meeting of ISMRM, Honolulu, 2017. P. 1128

7 Myung-Kyun Woo, Suk-Min Hong, Jongho Lee, Chang-Ki Kang, Sung-Yeon Park, Young-Don Son, Young-Bo Kim, Zang-Hee Cho. Extended Monopole Antenna Array with Individual Shield (EMAS) Coil: An Improved Monopole Antenna Design for Brain Imaging at 7 Tesla MRI. Magn Reson Med 75:2566–2572, 2016

8 D.A. SEEBER, J. JEVTIC, A. MENON. Floating Shield Current Suppression Trap. D.A. Concepts Magn Reson Part B Magn Reson Eng 21B: 26–31, 2004

Chapter 5

Improved B_1^+ efficiency of a dipole antenna equipped with high dielectric constant (HDC) materials at 10.5T

Presented at

Myung Kyun Woo , Lance DelaBarre , Russell Lagore , Steve Jungst, Qing X. Yang, Bei Zhang, Sebastian Rupprecht, Riccardo Lattanzi, Michael T. Lanagan, Maryam Sarkarat, Kamil Ugurbil , and Gregor Adriany, “Improved B1+ efficiency of a dipole antenna equipped with high dielectric constant (HDC) materials at 10.5T”, 27th ISMRM meeting, Montreal, Canada, 13-17 May, 2019. [Digital poster #7431]

1 | Introduction

High dielectric constant (HDC) materials have been adapted for MRI to improve SNR, transmit B_1 efficiency, and B_1 field uniformity [1-3]. Typically, HDC materials are positioned between the subject and the RF coil, and for many ultra-high field (UHF) applications with improved local B_1 fields. Here, we explore the possible performance gains of a novel setup which flips the positions of antenna and HDC material. To investigate this, the B_1^+ efficiency of the "Normal" setup with object – dielectrics – antenna was compared with a "Flipped" setup of object – antenna – dielectrics. The comparison included arrangements where, both the flipped and the normal setups had the same distance between the dipole and the sample as well as a geometry where the dipole was placed close to the sample. Besides the two HDC dipole configurations we also evaluated for comparison an inductively shortened dipole of the same length [4]. All three configurations were compared in terms of B_1^+ efficiency relative to RF power used ($B_1^+/\sqrt{W}$) and relative to SAR ($B_1^+/\sqrt{W}/\sqrt{10g\ SAR_{peak}}$) and verified experimentally at 10.5T.

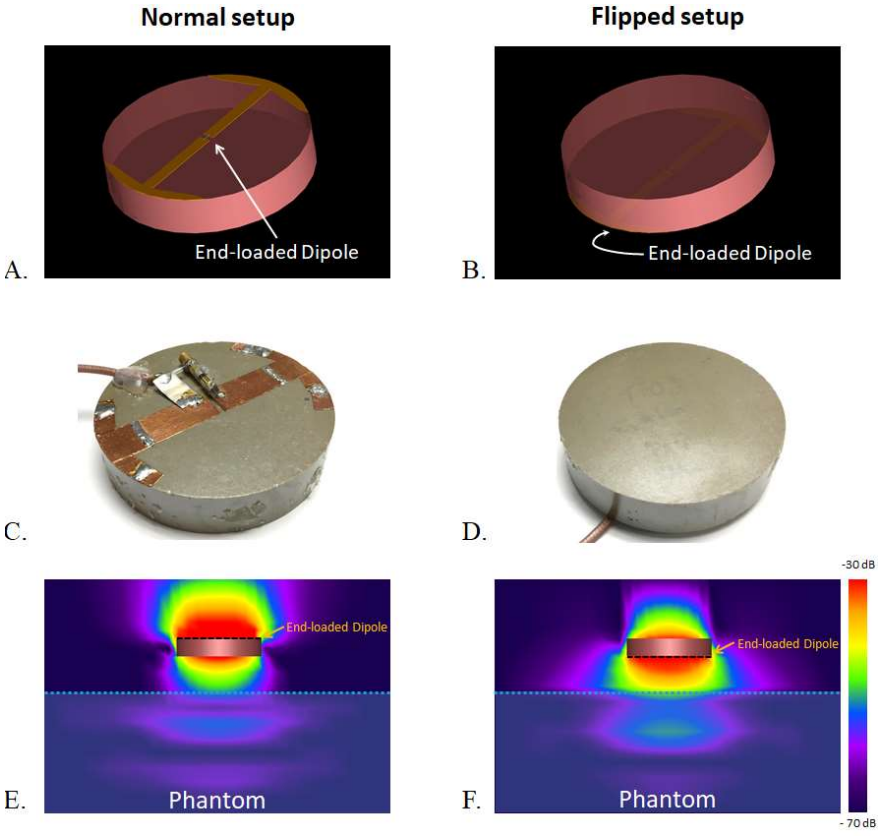

Figure 1. 3D CAD rendering, photographs and B_1 field pattern of an HDC disk with an end-loaded dipole attached to it in the "Normal" setup (A, C, and E) and the "Flipped" setup (B, D, and F). The blue dotted lines indicate the edge of the phantom.

2 | Methods

3D CAD renderings, photographs, and B-field patterns of the "Normal" and "Flipped" dipole antennas with HDC materials (TiO_2) are shown in Fig.1. The HDC (σ= 0.0031 S/m and ε_r = 100) material was formed into two different shapes [5]. One is a flat disk (8.2 cm diameter and 1.6 cm thick) and the other is 15 cm long box shape (two-3.2 x 7.5 x 1.6 cm^3 placed end to end) [6, 7]. An end-loaded dipole was built directly onto the

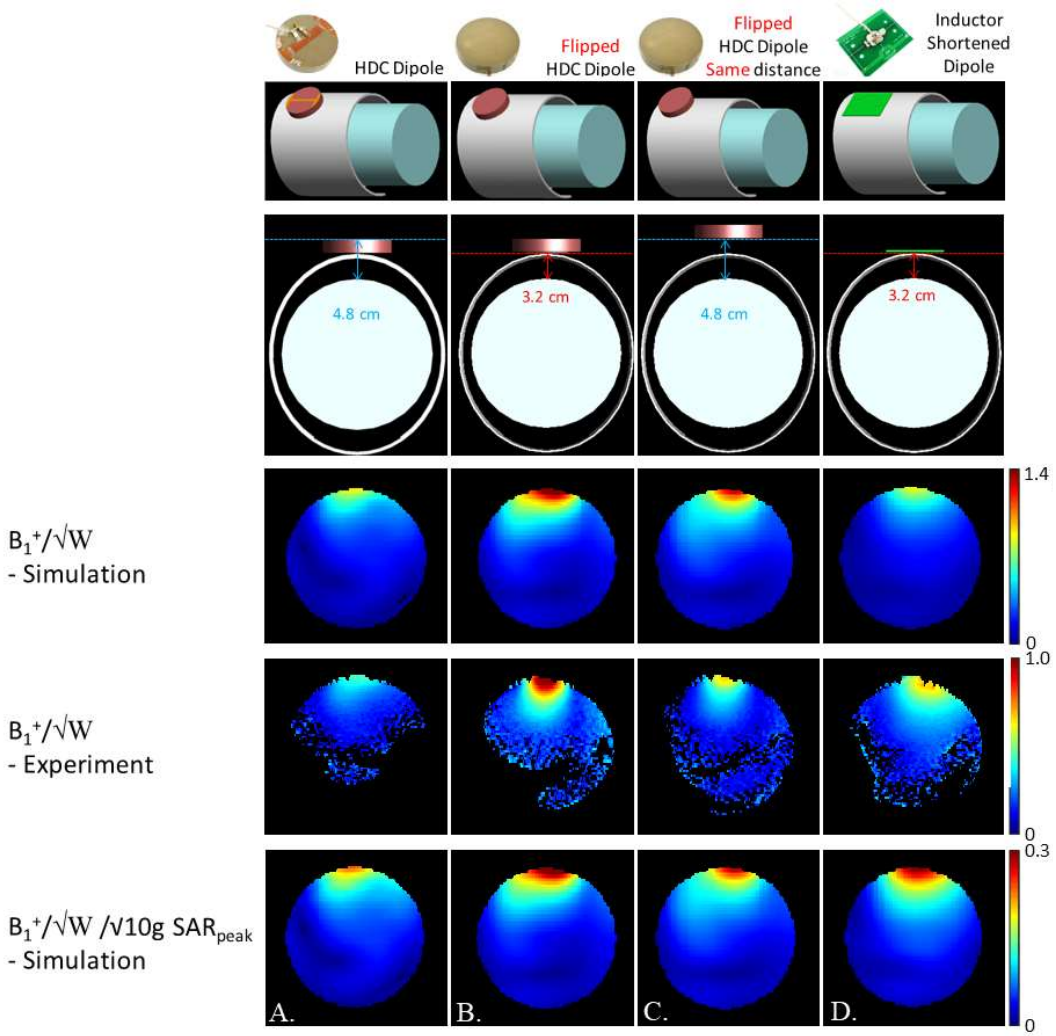

Figure 2. B_1^+ efficiency - Simulation (μT/√W) , B_1^+ efficiency - Experiment (μT/√W), and $B_1^+/\sqrt{W}$ /√10g SAR_{peak} (μT/√kg/W) maps with (A) Normal setup, (B) Flipped setup, (C) Flipped setup maintaining the same distance between the dipole and the subject as (A) and (D) Inductor-shortened dipole without HDC materials that has the same dipole length as in (A-C). Blue and red dashed lines indicate the location of dipole. Blue dashed lines of (A) and (C) indicate the same position (4.8 cm) and red dashed lines of (B) and (D) indicate the same position (3.2 cm).

HDC material with using one variable capacitor (Voltronics, NJ, USA). Experimental B_1^+ fields were obtained using an actual flip angle imaging (AFI) sequence for a cylindrical phantom (17 cm diameter and 30.5 cm long) with uniform electrical properties (σ= 0.6 S/m and ε_r = 49) at 10.5T [8]. B_1^+ fields were calculated in MATLAB (Mathworks, Inc., Natick, MA, USA) and were normalized to 1 W for B_1^+ efficiency ($\mu T/\sqrt{W}$). The B_1^+ efficiency ($B_1^+/\sqrt{W}$) and B_1^+/SAR ($B_1^+/\sqrt{W}/\sqrt{10g\ SAR_{peak}}$) were compared for the (i)normal setup (Fig.2A), (ii)the flipped setup (where the dipole/HDC complex was at the same location relative to the sample as the normal set up but the dipole was placed on the proximal as opposed to the distal (relative to sample) surface of the HDC material) (Fig.2B), (iii)the flipped setup with the distance between dipole and the sample identical to the normal setup (Fig.2C) and (iv)a dipole without HDC materials that was shortened to be the same length as the HDC dipole by adding inductors at the feed-point. Simulated B_1^+ efficiency and 10g SAR were calculated using XFdtd (REMCOM, State College, PA) with 2 x 2 x 2 mm^3 resolution. Fig.2 shows the B_1^+ efficiency calculated by the simulation and experiments comparison for the HDC disk. The dipole was either 3.2 or 4.8 cm away from the phantom. Fig.3 shows the same comparisons (minus the shortened dipole) for the rectangular HDC block both in simulation and experiment. The HDC block dipole was located either 4.8 or 6.4 cm above the phantom. The values of the HDC disk (Tab.1) and HDC block (Tab.2) are summarized and compared.

Disk shaped HDC				
	Normal HDC Dipole	Flipped HDC dipole	Flipped (Same distance)	Inductor shortened dipole
$B_1^+/\sqrt{W}$ - Simulation ($\mu T/\sqrt{W}$)	0.83	1.74	1.37	1.13
$B_1^+/\sqrt{W}$ - Experiment ($\mu T/\sqrt{W}$)	0.45	1.16	0.68	0.72
$B_1^+/\sqrt{W}/\sqrt{10g\ SAR_{peak}}$ ($\mu T/\sqrt{kg/W}$)	0.24	0.38	0.33	0.32

Table 1. The highest point value of B_1^+ efficiency with the disk shape HDC - Simulation ($\mu T/\sqrt{W}$) , B_1^+ efficiency - Experiment ($\mu T/\sqrt{W}$), and $B_1^+/\sqrt{W}/\sqrt{10g\ SAR_{peak}}$ ($\mu T/\sqrt{kg/\ W}$) maps with (A) Normal setup, (B) Flipped setup, (C) Flipped setup at the same distance between the dipole and the subject as (A) and (D) Inductor shortened dipole with the same length of the dipole as (A), (B) and (C) without HDC materials.

3 | Results and Discussions

Fig.1E shows the dipole and HDC material complex and the B_1 field calculations around this complex. The related simulation and experimental results with the afore described configurations are shown in Fig.2 and Tab.1. The flipped setup shows substantially higher B_1^+ efficiency values compared to the normal setup or an inductively shortened dipole without HDC materials. When the distance between the dipole and the phantom is kept the same (Fig.2C) as the normal setup (Fig.2A), the flipped orientation still shows an

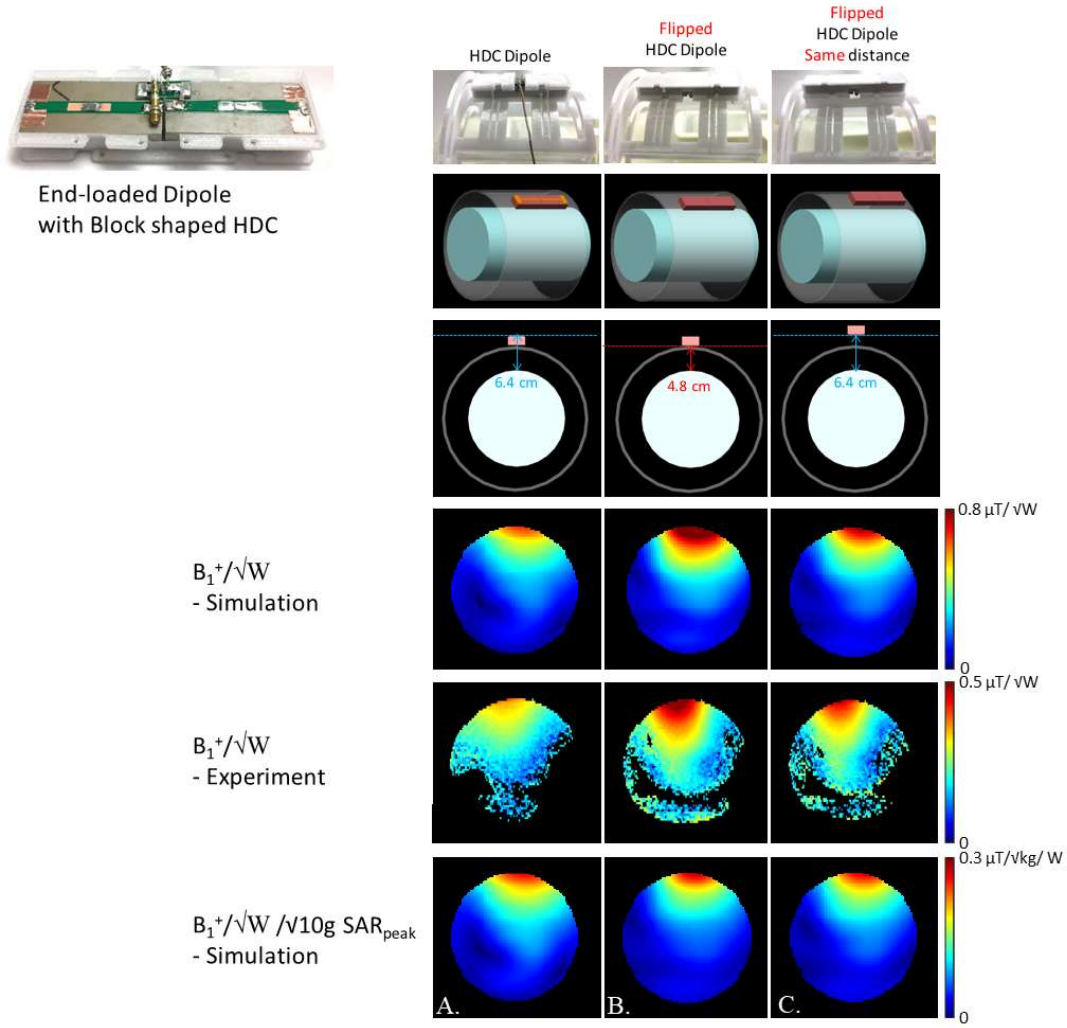

Figure 3. B_1^+ efficiency - Simulation (µT/√W) , B_1^+ efficiency - Experiment (µT/√W), and $B_1^+/\sqrt{W}$ /√10g SAR_{peak} (µT/√kg/ W) maps with (A) Normal setup, (B) Flipped setup and (C) Flipped setup at the same distance between the dipole and the subject as (A). Blue and red dashed lines indicate the location of dipole. Blue dashed lines of (A) and (C) indicate the same position (6.4 cm) and the red dashed line of (B) indicate 4.8 cm away from the phantom.

improvement. The flipped setup also produced the highest performance of relative $B_1^+/\sqrt{W}/\sqrt{10g}$ SAR_{peak}. To ensure independence of this effect from the HDC material shape, a dipole with different dimensions built on a rectangular-shaped HDC block demonstrated the same trends, as shown in Fig.3. The material properties and physical dimensions of the HDC material influence the gains made by flipping the order of the dipole and HDC material. Simulations directed the choice of HDC block size demonstrated in Fig.3.

Block shaped HDC			
	Normal HDC Dipole	Flipped HDC dipole	Flipped (Same distance)
$B_1^+/\sqrt{W}$ - Simulation ($\mu T/\sqrt{W}$)	0.67	1.06	0.79
$B_1^+/\sqrt{W}$ - Experiment ($\mu T/\sqrt{W}$)	0.41	0.58	0.51
$B_1^+/\sqrt{W}/\sqrt{10g}$ SAR_{peak} ($\mu T/\sqrt{kg/W}$)	0.27	0.29	0.27

Table 2. The highest point value of B_1^+ efficiency with the two segmented block shaped pucks- Simulation ($\mu T/\sqrt{W}$) , B_1^+ efficiency - Experiment ($\mu T/\sqrt{W}$), and $B_1^+/\sqrt{W}/\sqrt{10g}$ SAR_{peak} ($\mu T/\sqrt{kg/W}$) maps with (A) Normal setup, (B) Flipped setup, (C) Flipped setup at the same distance between the dipole and the subject as (A) and (D) Inductor shortened dipole with the same length of the dipole as (A), (B) and (C) without HDC materials.

4 | Conclusion

For dipoles built onto HDC materials, the highest B_1^+ efficiency ($B_1^+/\sqrt{W}$) can be achieved when the antenna side faces the imaging sample and the HDC material facing away. These HDC dipoles show favorable $B_1^+/\sqrt{W}/\sqrt{10g}$ SAR_{peak} compared to the other setups studied and is thus expected to be the more efficient transmitter and by reciprocity receiver as well. We plan to expand this work by studying different geometries and a complete array setup.

ACKNOWLEGEMENTS

NIH- U01 EB025144 S10 RR026783, BTRCP41 EB015894, P30 NS076408 and WM Keck Foundation

References

1 Neuberger T, Tyagi V, Semouchkina E, Lanagan M,Baker A, Haines K, et al. Concept Magn Reson Part B: Magn Reson 2008; Eng33B:109–114.

2 Qing X. Yang, Wei Luo, Sebastian Rupprecht, Zachary Herse, Christopher Sica, Jianli Wang, Zhipeng Cao, Jeffrey Vesek, Michael T. Lanagan, Giuseppe Carluccio, Yeun-Chul Ryu, and Christopher M. Collins. J Magn Reson. 2006; 24(1):197-202; 2

3 Haines K, Neuberger T, Lanagan M, Semouchkina E,Webb AG. J Magn Reson 2009; 200:349–353.

4 Bei Zhang, Gang Chen, Martijn Cloos, Zidan Yu, Jerzy Walczyk, Christopher Collins, Ryan Brown, Riccardo Lattanzi, Daniel Sodickson and Graham Wiggins. In Proceedings of the 25th Annual Meeting of ISMRM, Honolulu, 2017. P. 4314

5 Luo, W., Guo, J., Randall, C. and Lanagan, M., 2017. Effect of porosity and microstructure on the microwave dielectric properties of rutile. Materials Letters, 200, pp.101-104.

6 Russell L Lagore, Lance DelaBarre, Qing X Yang, Michael Lanagan, Yigitcan Eryaman, Sebastian Rupprecht, Wei Luo, Byeong-Yeul Lee, Xiao-Hong Zhu, Kamil Ugurbil, Wei Chen, Gregor Adriany. In Proceedings of the 25th Annual Meeting of ISMRM, Honolulu, 2017. P. 1128

7 Myung Kyun Woo, Lance DelaBarre, Jerahmie Radder, Russell Lagore, Yigitcan Eryaman, Kamil Ugurbil, and Gregor Adriany. In proceedings of the 26th Annual Meeting of ISMRM, Paris, 2018. P. 24

8 Beck BL, Jenkins KA, Rocca JR, Fitzsimmons JR. Tissue-equivalent phantoms for high frequencies. Concepts Magn. Reson. [Internet] 2004;20B:30–33. doi: 10.1002/cmr.b.20002.

Chapter 6

Floating asymmetric sleeve antenna array for magnetic resonance imaging

Presented at

Myung Kyun Woo, Lance DelaBarre, Russell Lagore , Steve Jungst, Kamil Ugurbil , and Gregor Adriany, “Evaluation of a sleeve monopole antenna array, a novel 16-channel radiative antenna array at 10.5T”, 27th ISMRM meeting, Montreal, Canada, 13-17 May, 2019. [Power pitch #7652]

Submitted to

Myung Kyun Woo[1], Lance DelaBarre[1], Russell Luke Lagore[1], Jingu Lee[2, 3], Steve Jungst[1], Matt Thomas Wacks[1], Andrea Grant[1], Yigitcan Eryaman[1], Kamil Ugurbil[1], and Gregor Adriany[1*], Institute of Electrical and Electronics Engineers (IEEE) Transaction on Medical Imaging, 10 October 2020

Abstract

Multi-element transmit arrays with low peak 10 g specific absorption rate (SAR) and high SAR efficiency (defined as $(B_1^+/\sqrt{}_{peak}SAR_{10g})$ are essential for ultra-high field (UHF) magnetic resonance imaging (MRI) applications. Recently, the adaptation of dipole antennas used as MRI coil elements in multi-channel arrays has provided the community with a technological solution capable of producing uniform images and low SAR efficiency at these high field strengths. However, human head-sized arrays consisting of dipole elements have a practical limitation to the number of channels that can be used due to radiofrequency (RF) coupling between the antenna elements, as well as, the coaxial cables necessary to connect them.

Here we suggest an asymmetric sleeve antenna as an alternative to the dipole antenna. When used in an array as MRI coil elements, the asymmetric sleeve antenna can generate reduced peak 10 g SAR and improved SAR efficiency. To demonstrate the advantages of an array consisting of our suggested design, we compared various performance metrics produced by 16-channel arrays of asymmetric sleeve antennas and dipole antennas with the same dimensions. Comparison data were produced on a phantom in electromagnetic (EM) simulations and verified with experiments at 10.5 Tesla (T). The results produced by the 16-channel asymmetric sleeve antenna array demonstrated 28 % lower peak 10 g SAR and 18.6 % higher SAR efficiency when compared to the 16-channel dipole antenna array.

Index Terms—cable trap, dipole antenna, deep brain imaging, asymmetric sleeve antenna, ultra-high field magnetic resonance imaging

1 | Introduction

Magnetic resonance imaging (MRI) at ultra-high fields (UHF, defined as ≥7 tesla (T)) are increasingly pursued for biomedical research due to gains in signal-to-noise [74-77] and, in some cases, contrast-to-noise ratios (SNR and CNR, respectively) (e.g. [78,79]). This has led to initiatives pushing human MRI systems to extremely high magnetic field strengths, such as 10.5 T [48,80]. However, in the UHF regime, the ratio of the wavelength of the radiofrequency (RF) electromagnetic (EM) waves employed for excitation of signals from the water protons in tissue compared to the object size becomes less than one [75,81]. Consequently, UHF RF coil designs frequently migrate towards far field antenna concepts rather than the near field domain, like those used at current clinical MRI field strengths.

As MRI pushes into the UHF regime, electric (E) and magnetic (B) field amplitude and phase non-uniformities increase over the sample volume, and this leads to non-uniform power deposition and transmit efficiency [77,81-84]. Radiative type antennas [48,55,56,85], particularly half wavelength (λ/2) dipole antennas, have been suggested as building blocks for such UHF transmit arrays and have recently shown promising performance initially for applications in the human torso [44,55,80,86] and recently in the human head [48,71,87] enabling improved transmit B_1 efficiency and minimized power deposition in the imaging target (i.e. specific absorption rate (SAR)). Compared to other RF coil types, such as loops (e.g. [52,88]) or microstrip type structures [53,54], dipole antennas show more favorable Poynting vectors and improved B_1 shimming performance. Dipole antennas also achieve greater penetration depth, however they encounter greater challenges in minimizing the mutual coupling between neighboring elements. For applications in the human torso, this challenge is mitigated by positioning the antenna in consistent close proximity to the body, thus promoting maximal coupling between the sample and the antenna while maintaining consistent coupling between neighboring elements. Similarly, subject-specific stripline coil arrangements in combination with geometric capacitive decoupling schemes had been successfully utilized to support more reliable coil loading for head arrays at 7 T [89]. More recently, in order to minimize coupling for radiative antenna arrays, a number of innovative decoupling techniques have been suggested [90-93]. However mutual coupling and radiation remain a significantly problem for human head applications at 10.5 T due to the relatively large and non-uniform gap between the head and the antenna array [92,94,95]. The lack of strong coupling to the imaging object encountered for dipole antenna array implementations for human head imaging also results in stronger interaction between the dipole antenna and the coaxial feed cable, which is typically routed in parallel to one leg of the dipole antenna in MR applications. Combined with the interaction among the many coaxial cables in a multi-element array, degraded antenna performance and significant E- and B-field perturbations have been observed [96-98].

Here we adapt the sleeve antenna concept for MR imaging at UHF. The "sleeve" of the sleeve antenna concept has the same structure as a cable trap and we can elegantly use this for reducing sheath currents on the coaxial feed cable. We incorporate these floating sleeves [99,100] into the antenna feed structure and extend the concept towards development of an asymmetric sleeve antenna array for MRI applications in the human head. In this paper, we describe a 16-channel asymmetric sleeve antenna array design for 447 MHz (10.5 T human head ^{1}H imaging), which, at the time of this publication, is the highest magnetic field available for human imaging. We compare this asymmetric sleeve antenna array to a dipole antenna array and present validation with EM simulations and 10.5 T MR experiments, demonstrating advantages in B_1^+ efficiency (defined as B_1^+ amplitude in the center of the coil per unit square root power), 10 g SAR, and SAR efficiency (defined as $(B_1^+\text{Center}/\sqrt{_{\text{peak}}\text{SAR}_{10\text{g}}})$).

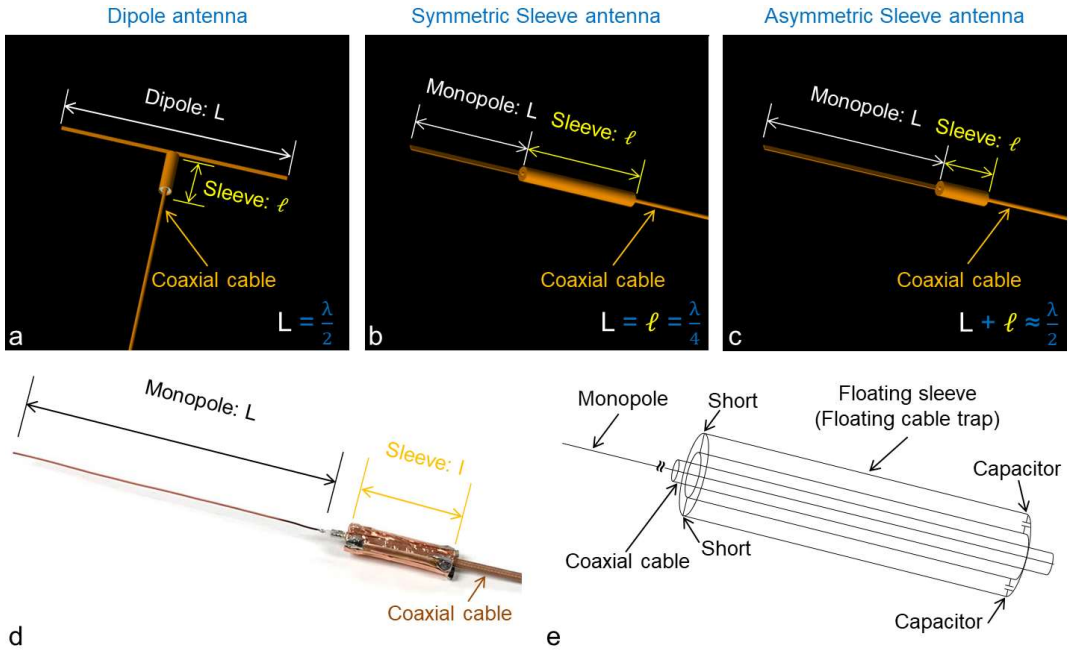

Fig. 1 Modification steps involved in converting a dipole antenna (a) to a symmetric sleeve antenna (b) then to an asymmetric sleeve antenna (c). The basic structures of a dipole and a symmetric sleeve antenna are equivalent (b). However, the sleeve antenna is an end-fed structure (b and c) while the dipole antenna is a center-fed structure (a). The sleeve portion of the sleeve antenna is a part of the antenna which acts as the ground. The architecture of the sleeve antenna leads the freedom to modify the length of the antenna part, which consists of the monopole, and sleeve portion, leading to an asymmetric sleeve antenna (c-e). Photograph (d) and schematic diagram (e) of an asymmetric sleeve antenna. The sleeve portion of the antenna is mechanically fixed in position, remains electrically floating without any direct contact to conductors of the coaxial cable.

2 | Methods

A. Antenna concept and design of the asymmetric sleeve antenna

The 3D modeling of a single element dipole antenna (Fig. 1a), a symmetric sleeve antenna (Fig. 1b) and an asymmetric sleeve antenna (Fig. 1c) are shown above, indicating the evolution from a classical half wave dipole to an asymmetric sleeve antenna. The practical implementation is shown in Fig. 1d; and drawn schematically in Fig. 1e. The basic structure of a sleeve antenna [99-103] is configured as a seamless combination of a monopole (= λ/4) built from the center conductor of a coaxial cable with one floating cable trap (= λ/4) placed over the shield. The resulting structure is equivalent to a dipole antenna since the total structural length of the monopole and associated floating cable trap approximate a half wavelength. The length of the floating cable trap and monopole can be varied as long as the sum of the aforementioned parts remains the same (Fig. 1c-1e). The possibility to vary the length of the monopole and sleeve portions of the antenna adds an essential degree of freedom in the design and supports asymmetrical construction with benefits for the overall antenna layout [102,103].

Theoretically the current distribution of the half wave dipole and the asymmetric sleeve antenna can be described as

$$I_{Dipole} = I_0 \sin(\frac{\beta L}{2}) \quad (1)$$

$$I_{Sleeve} = I_0 \sin(\beta(\frac{L}{2} - h)) = I_0 \sin(\beta \ell), \quad (2)$$

where I_{Dipole} and I_{Sleeve} are the current of the dipole and asymmetric sleeve antenna at the matching point, respectively. ß is the phase constant associated with the transmission line, L is the length of dipole antenna (Fig. 1a) and ℓ is the length of the floating sleeve (Fig. 1c) [103,104].

In air, the resonant length of a dipole antenna is the sum of the equal length poles. At 447 MHz, this half wavelength is ~330 mm. For the sleeve antenna, the length of the antenna is the sum of the length of monopole and floating cable trap, which is also approximately one half of the wavelength [101,102]. Due to dielectric media in close proximity (e.g., human head), the actual effective resonance length of the antenna is shortened to ~250 mm for both dipole antenna and sleeve antenna.

B. Construction of the 16-channel arrays

The coil arrays and related coil formers were 3D modeled and the formers were fabricated in-house using a 3D printer (F410, Fusion3 Design, Greensboro, NC, USA). Both the 16-channel dipole (Fig. 2a and 2b) and asymmetric sleeve antenna arrays (Fig.

2c and 2d) were designed and fabricated to the same physical inner dimensions. The array elements were arranged on an elliptically shaped former with a minor axis of 100 mm and major axis of 110 mm. The length of the formers is 250 mm for the dipole antenna array and 200 mm for the asymmetric sleeve antenna array. This geometry results in an arrangement of sixteen antennas with 39 ± 14 mm spacing between individual elements. These arrays use the same elements for B_1 transmit and receive

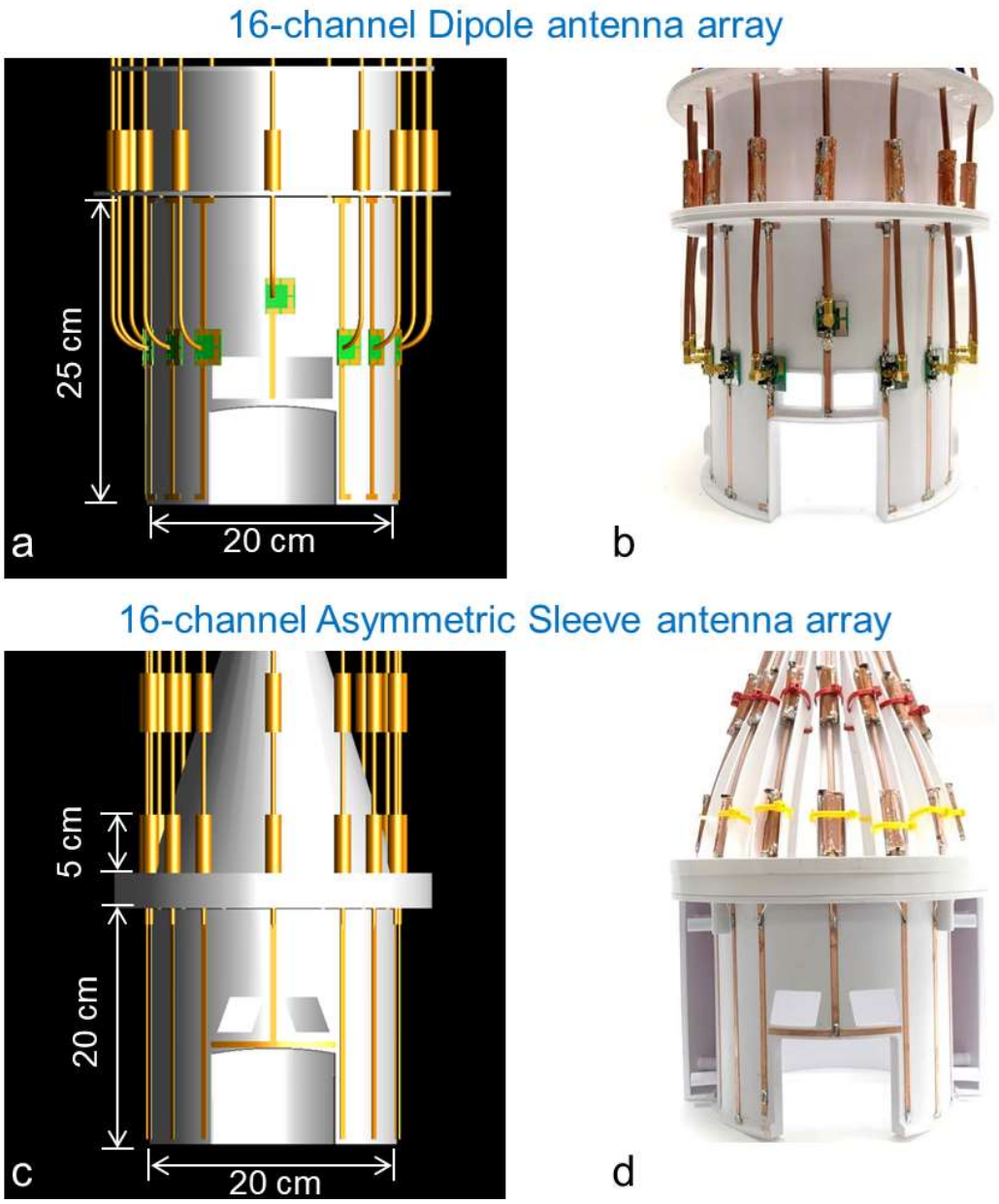

Fig. 2 3D modeling (a and c) and photographs (b and d) of the 16-channel dipole and the 16-channel asymmetric sleeve antenna arrays. Importantly, all coaxial cables were included in the simulation to calculate E- and B-fields.

(i.e. transceive array); the concepts, however, can be extended to transmit only and receive only designs.

A 16-channel dipole antenna (length: 250 mm) array with end points were built [85,105]. Fine tuning of individual elements was achieved by adjusting the end points of each dipole antenna. In the frontal location, tuning inductors were inserted into both legs of the dipole in order to achieve the required physical length reduction while preserving electrical length and subsequent resonance frequency. The use of lattice balun match circuit and a floating cable trap significantly reduced sheath currents for each element of the 16-channel dipole antenna array (Fig. 2a and 2b). The length of each monopole conductor of the 16-channel asymmetric sleeve antenna array was set to 200 mm and combined with the 50 mm floating cable trap as shown in Fig. 2c and 2d.

All floating cable traps were built utilizing 50 mm long 3D printed polyethylene terephthalate glycol-modified (PETG) pipe structures. Each pipe has a 12 mm outer diameter and 5 mm inner diameter which accommodates the RG-400 coaxial feed cable. Two ceramic capacitors (100B series, American Technical Ceramics, Huntington Station, NY, USA) and one variable capacitor (JZ200HV, Knowles Voltronics, Cazenovia, NY, USA) were used to adjust the resonance frequency of the cable traps. Two sets of cable traps were utilized for each sleeve element, with the first set located at the nearest point to the antenna feed point; the second set located another quarter wavelength down the feed cable [99,100]. The 16-channel dipole antenna array was equipped with the same type of floating cable traps at a quarter wavelength distance from the feed point. These cable traps reduced the coupling between the coaxial cable and dipole antenna. Optimally, cable traps should be located in immediate proximity to the feed point. In practice, however, cable traps are resonant structures that can interact with one of the dipole antenna poles. Thus in practice it is beneficial to locate the cable traps up the feed coax $\lambda/4$ from the feed point for the dipole antenna.

C. Experimental setup and bench measurements

All MR experiments were performed using a 10.5 T / 880 mm whole body magnet (Agilent, Santa Clara, CA, USA) interfaced with a MAGNETOM 10.5 T console (Siemens Healthineers, Erlangen, Germany) equipped with 16 independent parallel transmit (pTx) channels. The pTx system allowed for full control over transmitter phase, amplitude, timing, and waveform. For better comparison with standard systems all data presented here were acquired with equal RF transmit power per channel. A 16-channel transmit/receive interface box (Virtumed, Minneapolis, MN, USA), mounted on the patient table was equipped with in-house built transmit/receive switch modules to connect all array elements to the MRI system as shown in Fig. 3a and 3d. All of the individual antenna elements were connected with coaxial cables to the interface box and then on to the pTx system connectors of the MR scanner.

The phantom used to compare coil performance was an acrylic cylindrical container 180 mm in diameter and 305 mm in height filled with a sucrose doped saline solution [106]. Electromagnetic properties of this solution were measured using a DAKS-12 (SPEAG, Zurich, Switzerland) to be ε_r = 49 and σ = 0.6 S/m. The diameter of the phantom was selected based on the availability of pre-fabricated acrylic tubes that were close in size to that of the human head. The length of phantom was chosen to emulate the human head and neck. The phantom was positioned within the coil formers in a realistic location for the human brain imaging applications.

All input reflections and coupling coefficients were measured in bench measurements using a 16-channel network analyzer (ZNBT8, Rohde & Schwarz,

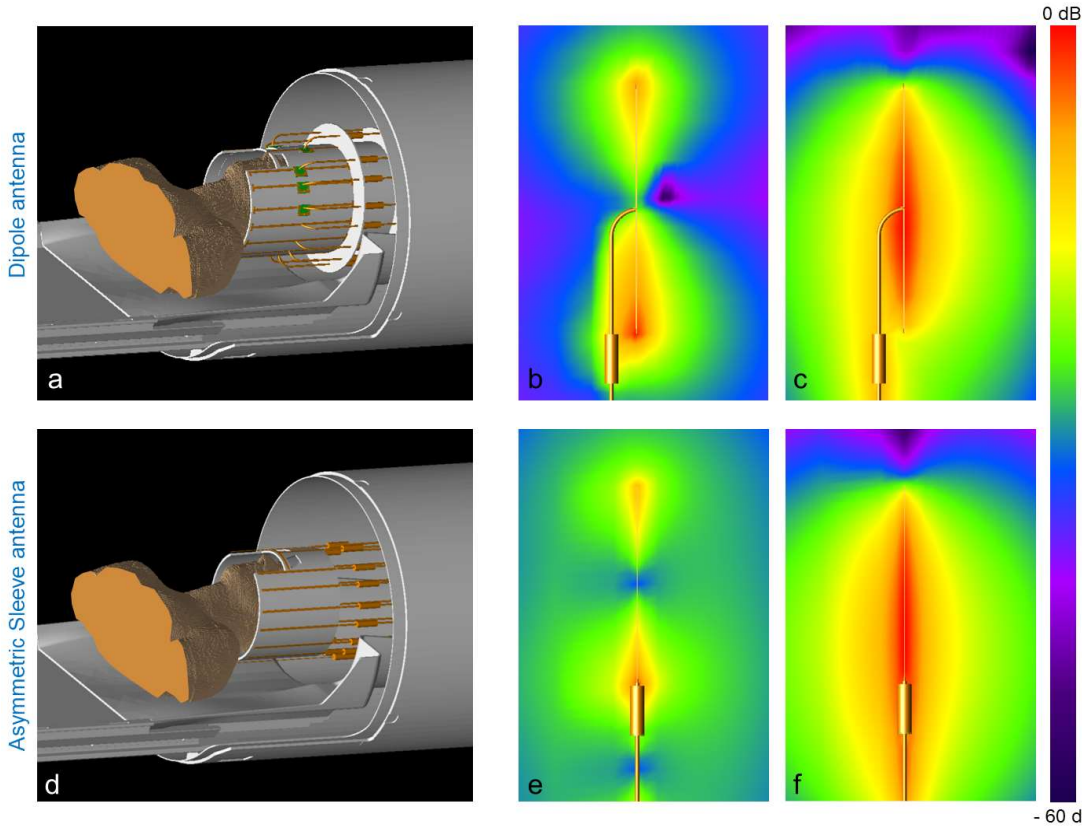

Fig. 3 Simulation model of a dipole antenna array (a) and an asymmetric sleeve antenna array (d) with coaxial cables in the bore of the MRI system. For realistic head imaging, coaxial feed cables have to be positioned in parallel alignment with antennas for an in bore setup. Individual E-fields in free space including simulation of the coaxial cable of one dipole antenna (b) and one asymmetric sleeve antenna (e) are shown. Also shown are corresponding B-fields of one dipole antenna (c) and one asymmetric sleeve antenna (f). Note the higher interaction of the dipole antenna array with the center-fed coaxial cable, which results in high E- and B-fields between one pole of a dipole antenna and a coaxial cable (b and c). However, this is notably minimized in the asymmetric sleeve antenna (e and f).

Munich, Germany). The S-parameters of all 16 elements both arrays were measured in dB scaled values. The S_{11} of all channels, the S_{21} values with the nearest neighbors, and S_{31} values with the next nearest neighbors of all 16-channel are summarized in Fig. 4a and 4d.

Noise covariance matrices of the 16-channel dipole antenna array (Fig. 4b) and the 16-channel asymmetric sleeve antenna array (Fig. 4e) were acquired to experimentally evaluate the crosstalk between the elements [66]. An actual flip angle imaging (AFI) sequence (TR1/TR2 = 20/120 ms, TE = 3.39 ms, nominal flip angle = 60°, GRAPPA (R=2), resolution = 2 mm × 4 mm × 6 mm) was used to obtain the transmit B_1^+ field maps (Fig. 5c and 5d) with the cylindrical phantom in a circular polarization (CP) mode. All B_1^+ efficiency data sets using AFI were achieved with rectangle pulses (non-selective option and 3D). The flip angle with short TR_1 and TR_2 was calculated by

$$\alpha = \arccos\left(\frac{rn-1}{n-r}\right), \tag{3}$$

where α = flip angle, n = TR_2/TR_1, and $r \approx \frac{1+n\cos\alpha}{n+\cos\alpha}$ [107]. The flip angle was converted to B_1^+ with

$$\alpha = 2\pi\gamma B_1^+\tau, \tag{4}$$

where γ is the gyromagnetic ratio and τ is the width in seconds of the RF pulse [108]. The individual relative B_1 magnitude maps corresponding to each channel of the arrays are shown in Fig. 4c for the dipole antenna array and in Fig. 4f for the asymmetric sleeve antenna array. An individual relative B_1 magnitude map is defined here as the magnitude of each individual transmitter divided by the total magnitude of all sixteen individual transmitter maps. In other words, the individual relative B_1 map is proportional to the total of all B_1 fields. The total magnitude of all sixteen individual transmitter maps was obtained by the calculation with the square root sum of squares. High resolution T_2 weighted TSE images (TR = 5000 ms, TE = 72 ms, TA = 3:45 min, echo train length = 9, BW = 488 Hz/pixel, FOV = 200 mm × 159 mm, resolution = 0.39 mm × 0.39 mm × 1.0 mm) of a human cadaver were obtained for the evaluation of the 16-channel asymmetric sleeve antenna array.

D. Numerical simulation

EM simulations (XFdtd, REMCOM, State College, PA, USA) were performed to acquire E- (Fig. 3b) and B- (Fig. 3c) fields of the 250 mm long dipole antenna and E- (Fig, 3e) and B- (Fig.3f) fields of the asymmetric sleeve antenna (200 mm monopole antenna + 50 mm sleeve). These simulation were obtained with parallel alignment of a sleeve (= cable trap) and a coaxial cable for the dipole antenna and with collinear

alignment of a sleeve and a coaxial cable for the asymmetric sleeve antenna. Coaxial cables were modeled by parallel cylindrical central bars and pipe structures with realistic dimensions and electrical characteristic of copper. All cable traps were modeled and included in the simulation to match the experimental setup as much as possible.

EM simulations were also used to calculate B_1^+ fields (Fig. 5a and 5b) and 10 g SAR (Fig. 6a and 6b) of both the 16-channel dipole antenna and the asymmetric sleeve antenna arrays with non-isotropic gridding (minimum: 4 mm and maximum: 8 mm). A phantom with matching dimensions and electrical properties was selected for experimental verification with a 1 mm × 1 mm × 1 mm resolution (re-gridded by post-processing). Importantly, all of the simulated 16-channel arrays included the coaxial cables and the sleeve - thus closely resembling the practical coil setup. All data were calculated using MATLAB (The Mathworks, Inc., Natick, MA, USA) after EM simulation. B_1^+ fields were determined from

$$B_1^+ = \left|\frac{B_x + iB_y}{2}\right|, \qquad (5)$$

where B_x and B_y are the complex amplitudes of x- and y-oriented RF magnetic fields, respectively [109].

B_1^+ efficiency, 10 g SAR, and SAR efficiency maps shown below (Fig. 5 and Fig. 6) compare the two 16-channel arrays. B_1^+ fields were normalized to 1 W, in order to evaluate the B_1^+ efficiency. The normalization was performed over the power supplied to the all antenna elements. For the safety validation, 10 g SAR (W/kg) values were calculated from the E-field and compared between arrays. SAR efficiency values, which are B_1^+ efficiency per square root of peak 10 g SAR, were compared between arrays as shown in Fig. 6c and 6d. For a quantitative comparison, the highest B_1^+ efficiency, 10 g SAR, and SAR efficiency areas are indicated in the axial plane of the arrays. The values of each ROI (2 mm isotropic voxel) are indicated below the figures.

3 | Results

A. Comparison of bench measurements, simulation, and experiments between the 16-channel arrays

Bench measurements of the scattering parameters for the reflection (S_{11}) and coupling ($S_{21,}$ and S_{31}) coefficients when the coils were loaded with a uniform cylindrical phantom are summarized in Fig. 4a and 4d for both arrays, respectively. The S_{11} values of the 16-channel dipole and the asymmetric sleeve antenna arrays ranged between -11.1 dB to -28 dB, and between -15.4 dB to -22.8 dB, respectively. Coupling between adjacent elements (S_{21}) was in the range of -7.9 dB to -14.3 dB for the dipole antenna array and -8.7 dB to -19.6 dB for the asymmetric sleeve antenna array. Noise covariance matrices were obtained in an MR experiment and are shown in Fig. 4b and 4e. A maximum correlation value of 0.17 was observed for the 16-channel dipole antenna array and of 0.11 for the 16-channel asymmetric sleeve antenna array, respectively. Overall B_1^+ efficiency loss due to the inter-element coupling was calculated and shown to be 44 % for the 16-channel dipole antenna array and 22.7 % for the 16-channel asymmetric sleeve antenna array, respectively.

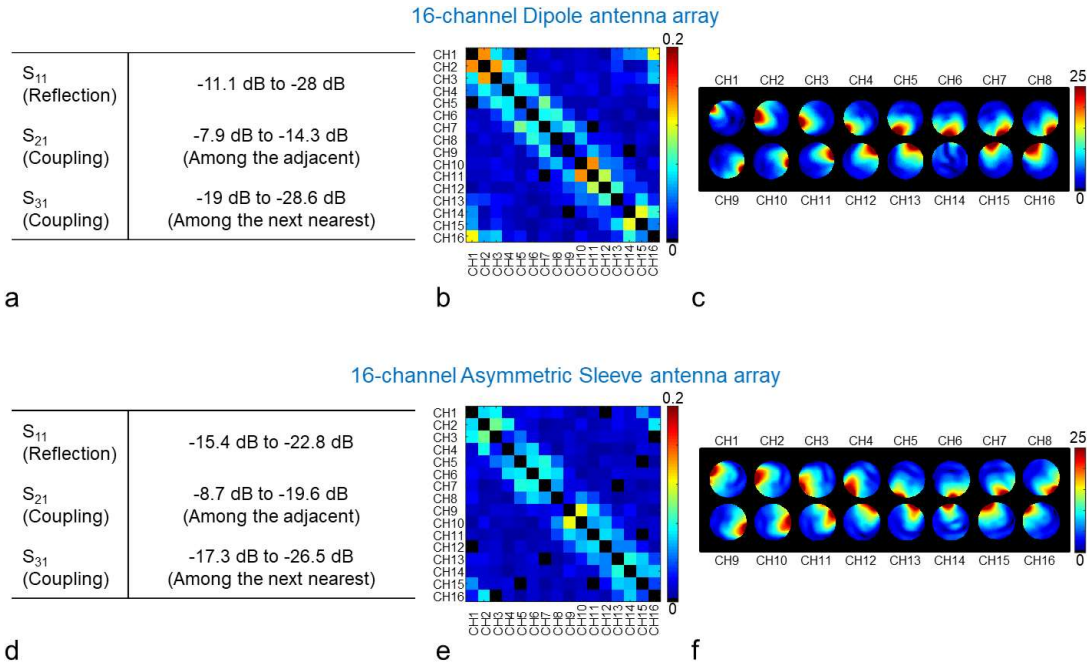

Fig. 4 Summary of the achieved S-parameters (a and d), noise covariance matrices (b and e) and individual relative B_1 magnitude maps (c and f) of the 16-channel dipole (upper row) and the 16-channel asymmetric sleeve antenna (lower row) arrays. Fig. 4c and 4f show relative percentage contribution of each transmitter on each pixel. Note that neither of these radiative arrays have any additional decoupling circuitry.

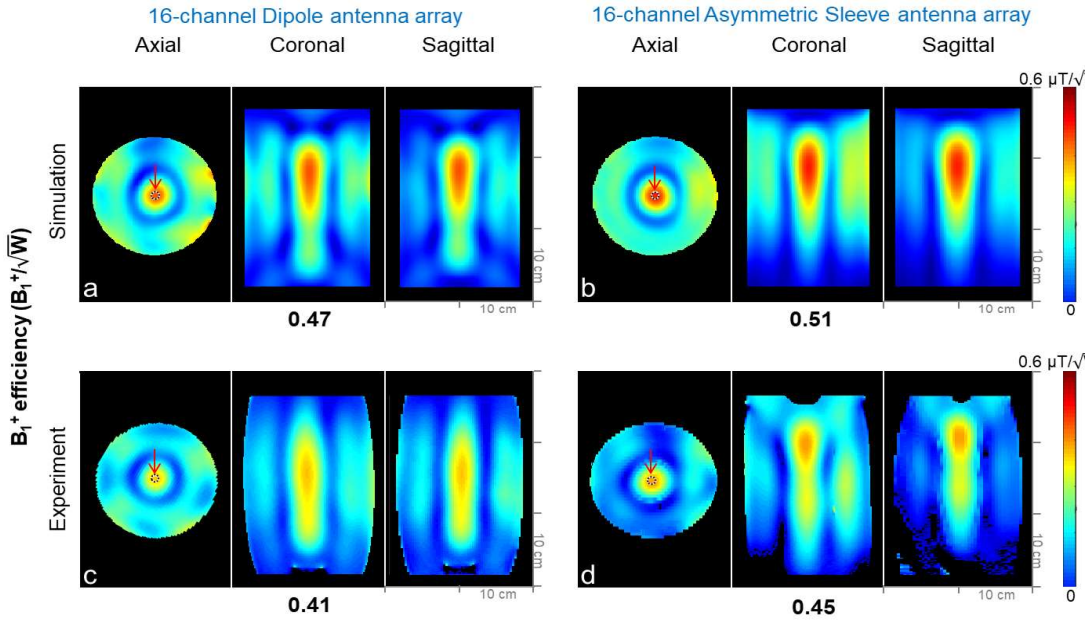

Fig. 5 Simulation (a and b) and experimental (c and d) B_1^+ efficiency ($B_1^+/\sqrt{W}$) maps of the 16-channel dipole and the 16-channel asymmetric sleeve antenna arrays with a phantom. The results are shown in the axial, coronal, and sagittal planes. For the experimental data (c and d), a threshold was applied for better data display purpose. Note: Due to the extended ROI of the 16-channel asymmetric sleeve antenna array, the sagittal image shows more field distortion compared to the 16-channel dipole antenna array. Red arrows indicate ROIs where values are measured. The measurements are listed below the corresponding set of figures for comparison.

The B_1^+ efficiency comparisons between the two arrays calculated from electromagnetic simulations and obtained experimentally are illustrated in Fig. 5. Compared to the 16-channel dipole antenna array, the 16-channel asymmetric sleeve antenna array achieved ~8 % higher B_1^+ (center) efficiency both in simulation and experimentally, as measured in the indicated region of interest (ROI) in the phantom. Red arrows indicate ROIs.

Peak 10 g SAR values of the 16-channel dipole (Fig. 6a) and the 16-channel asymmetric sleeve antenna arrays (Fig. 6b) were 0.32 W/kg and 0.25 W/kg with the phantom, respectively. This indicates 28 % lower SAR value for the 16-channel asymmetric sleeve antenna array compared to the 16-channel dipole antenna array. As observed in both the sagittal and coronal plane, the SAR distribution of the 16-channel asymmetric sleeve antenna array is more distributed in the z-direction compared to that of the 16-channel dipole antenna array. The result is that the 16-channel asymmetric sleeve antenna array showed 18.6 % higher SAR efficiency compared to the 16-channel dipole antenna array in the simulation due to the lower peak 10 g SAR values depicted in Fig. 6c and 6d.

B. Human cadaver experiments with the 16-channel asymmetric sleeve antenna array

The high resolution turbo-spin-echo (TSE) human cadaver images acquired at 10.5 T, shown in Fig. 7, demonstrate the good overall B_1 penetration and field distribution of the 16-channel asymmetric sleeve antenna array. These images were achieved with the 16-channel asymmetric sleeve antenna array driven in a CP mode without any further B_1 shimming or pTx pulses adjustments for improved transmit B_1 uniformity; the images were also not manipulated with reconstruction techniques aimed at flattening the signal intensity variations. In axial images, the signal intensity is highly uniform even in the absence of specific efforts to improve its uniformity.

4 | Discussions

Within the described parameters of our comparison, our results demonstrate clear benefits of the asymmetric sleeve antenna concept compared to dipole antenna array when used as RF coil array element at 447 MHz. The structure of the sleeve antenna itself closely resembles the dipole antenna with one important difference: the layout of a sleeve antenna element and the coaxial feed cable are collinear, whereas in the dipole antenna, the feed cable attaches at the center of the antenna and necessarily runs parallel to a portion of the dipole antenna to exit the coil assembly. The dipole antenna thus suffers from E- and B-fields interactions between the antenna element and the parallel-running feed cable. In MR body applications, dipole antennas can be placed directly on the body resulting in high coupling to the sample. This reduces interaction between the dipole antennas and coaxial feed cables. Remaining unbalanced currents flowing on coaxial feed cables can be tackled using balun matching networks, cable traps or the combination of the two [33,99,100]. For head applications, however, the weaker coupling combined with coaxial cable routing does affect both the E- and B-fields pattern of a dipole antenna. The collinear arrangements of the elements that make up the asymmetric sleeve antenna minimize these E- and B-fields interactions.

Moreover, the floating cable trap design of a sleeve antenna acts to further suppress imbalanced RF currents leaking onto the outer surface of the shield of the coaxial feed cable. These floating cable traps did not negatively influence either the antenna efficiency nor the radiation pattern.

The other important advantage of the asymmetric sleeve antenna array, compared to the dipole antenna array, is substantially lower peak 10 g SAR, and resulting enhanced SAR efficiency over a central ROI. To evaluate the safety at UHF, 10 g SAR can be used as an important criterion to estimate local E-fields and the related temperature changes [48,110-112]. As shown in supplementary Fig. 1[1], the peak 10 g SAR of the 16-channel asymmetric sleeve antenna array loaded with the human model was substantially lower than that of the 16-channel dipole antenna array. As a result, asymmetric sleeve antenna concepts allow for improved RF transmission for 10.5 T human brain imaging (for a given number of transmits channels).

Recently a passive feeding network and a snake type antenna structure were suggested to reduce peak 10 g SAR by Zivkovic et al. [113] and Steensma et al. [114], respectively. In future work, we will evaluate and compare SAR and SAR efficiency as a transceiver with these newly suggested techniques and we will also extend the comparison transmit-only and receive-only (TORO) arrays [115].

We observed non-uniformity along the superior-inferior (z-) direction, visible in the sagittal image (Fig. 7) produced by the asymmetric sleeve antenna array. This is to be expected as the cylindrical layout of the antenna elements does not allow for antenna

[1] A supplementary figure is available in the supporting documents.

conductors to be in the vicinity of the superior portion of the head. However, this could possibly be remedied using monopole elements that are not straight, but conform to the curvature of the head in the z-direction, and we will evaluate this in future work. Furthermore, B_1 shimming using pTx techniques can be utilized to improve the uniformity of images encompassing the entire human head, and we plan to evaluate this in future work.

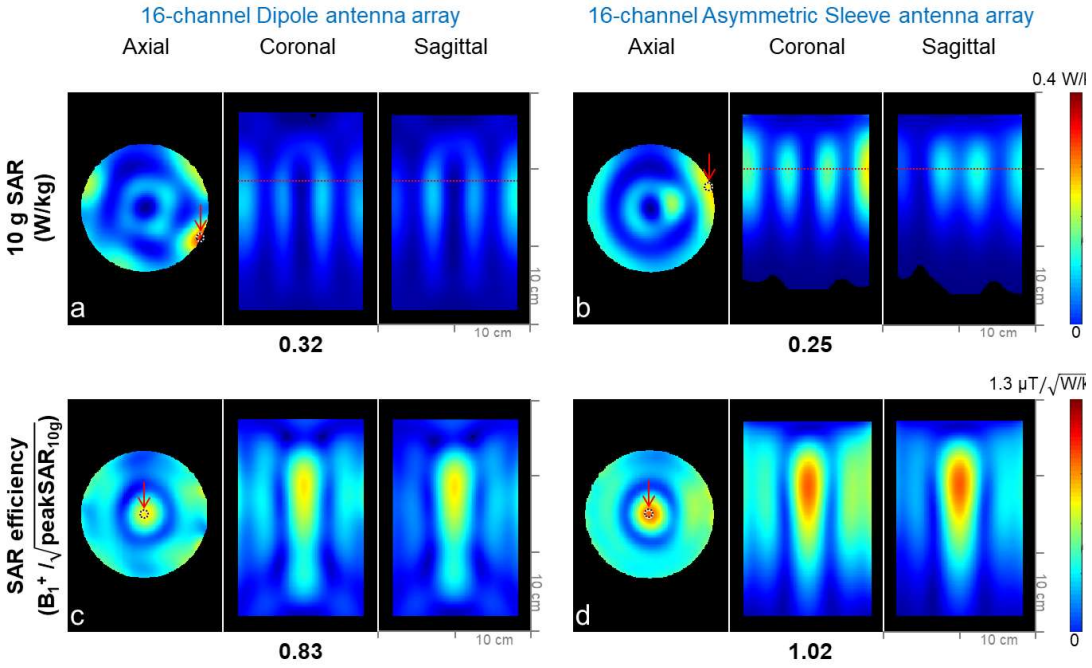

Fig. 6 10 g SAR (a and b) and SAR efficiency ($B_1^+ / \sqrt{_{peak}SAR_{10g}}$) (c and d) maps of the 16-channel dipole and asymmetric sleeve antenna arrays with a phantom; results are shown in axial, coronal, and sagittal planes. Red dotted lines of a coronal and a sagittal plane in Fig 6a and 6b indicate the location of the axial plane with peak 10 g SAR. Red arrows indicate ROIs where values are measured. The measurements are listed below the corresponding set of figures for comparison.

5 | Conclusion

Here we present an asymmetric sleeve antenna concept for UHF MRI of the human head and demonstrate the potential of this antenna type for imaging at 10.5 T. For future in-vivo human brain imaging, the asymmetric sleeve antenna array will be further optimized regarding number of channels and more form fitting geometry. This optimized sleeve antenna array will be RF safety validated for in vivo human head experiments and carefully evaluated for whole head shim capability. It is expected that the optimized sleeve antenna array geometry and utilization of pTx techniques will support further improved B_1 field and allow for lower peak 10 g SAR, which could lead to new neurological developments using UHF MRI.

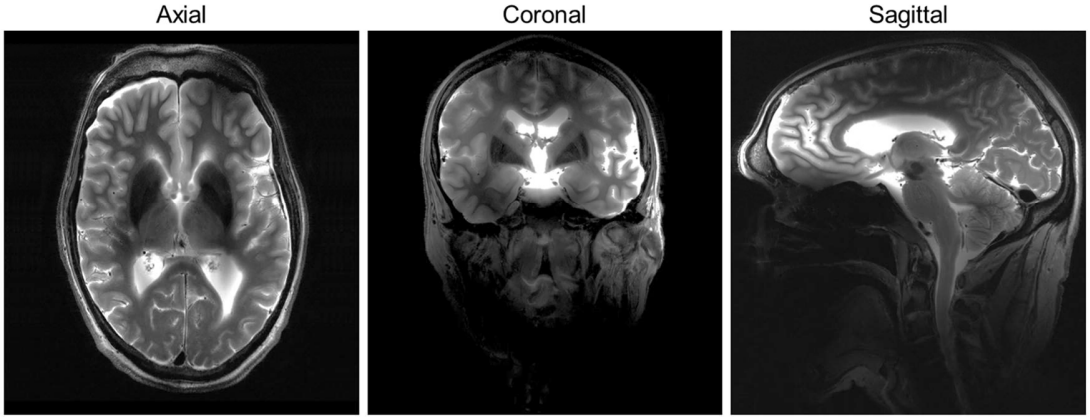

Fig. 7 Turbo-spin-echo (TSE) images acquired at 10.5 T with the 16-channel asymmetric sleeve antenna array with human cadaver in the axial, coronal and sagittal planes. The displayed images were achieved in circular polarization (CP) mode without any B_1 shimming or pTx pulse optimization technique. TR = 5000 ms, TE = 72 ms, TA = 3:45 min, BW = 488 Hz/pixel, FOV = 200 mm × 159 mm, resolution = 0.39 mm × 0.39 mm × 1.0 mm.

References

[1] B. Guérin et al., "The ultimate signal-to-noise ratio in realistic body models," *Magn Reson Med,* vol. 78, no. 5, pp. 1969-1980, 2017.

[2] K. Ugurbil, "Magnetic resonance imaging at ultrahigh fields," *IEEE Trans Biomed Eng,* vol. 61, no. 5, pp. 1364-79, May, 2014.

[3] K. Ugurbil, "Imaging at ultrahigh magnetic fields: History, challenges, and solutions," *Neuroimage,* vol. 168, pp. 7-32, Mar, 2018.

[4] J. T. Vaughan et al. , "7T vs. 4T: RF power, homogeneity, and signal-to-noise comparison in head images," *Magn Reson Med,* vol. 46, no. 1, pp. 24-30, Jul, 2001.

[5] J. H. Duyn, P. van Gelderen, T. Q. Li, J. A. de Zwart, A. P. Koretsky, and M. Fukunaga, "High-field MRI of brain cortical substructure based on signal phase," *Proc Natl Acad Sci U S A,* vol. 104, no. 28, pp. 11796-801, Jul 10, 2007.

[6] J. H. Lee et al., "High contrast and fast three-dimensional magnetic resonance imaging at high fields," *Magn Reson Med,* vol. 34, no. 3, pp. 308-312, 1995.

[7] X. He et al., "First in-vivo human imaging at 10.5 T: Imaging the body at 447 MHz," *Magn Reson Med,* vol. DOI: 10.1002/mrm.28131 2019.

[8] A. Sadeghi-Tarakameh et al., "In vivo human head MRI at 10.5 T: A radiofrequency safety study and preliminary imaging results," *Magn Reson Med,* vol. 84, no. 1, pp. 484-496, 2020.

[9] Q. X. Yang et al., "Analysis of wave behavior in lossy dielectric samples at high field," *Magn Reson Med,* vol. 47, no. 5, pp. 982-9, May, 2002.

[10] Z. Cao, J. Park, Z. H. Cho, and C. M. Collins, "Numerical evaluation of image homogeneity, signal-to-noise ratio, and specific absorption rate for human brain imaging at 1.5, 3, 7, 10.5, and 14T in an 8-channel transmit/receive array," *J Magn Reson Imaging,* vol. 41, no. 5, pp. 1432-1439, 2015.

[11] P. F. Van de Moortele et al., "B1 destructive interferences and spatial phase patterns at 7 T with a head transceiver array coil," *Magn Reson Med,* vol. 54, no. 6, pp. 1503-1518, 2005.

[12] F. Wiesinger, P. F. Van de Moortele, G. Adriany, N. De Zanche, K. Ugurbil, and K. P. Pruessmann "Parallel imaging performance as a function of field strength—an experimental investigation using electrodynamic scaling," *Magn Reson Med,* vol. 52, no. 5, pp. 953-964, 2004.

[13] S. M. Hong, J. H. Park, M. K. Woo, Y. B. Kim, and Z. H. Cho, "New design concept of monopole antenna array for UHF 7T MRI," *Magn Reson Med,* vol. 71, no. 5, pp. 1944-52, May, 2014.

[14] A. Raaijmakers et al., "Design of a radiative surface coil array element at 7 T: the single-side adapted dipole antenna," *Magn Reson Med,* vol. 66, no. 5, pp. 1488-1497, 2011.

[15] G. C. Wiggins, B. Zhang, R. Lattanzi, G. Chen, and D. Sodickson, "The electric dipole array: an attempt to match the ideal current pattern for central SNR at 7 Tesla," in Proc. 20th Annu. Meeting ISMRM, Melbourne, Australia, 2012, pp. 541.

[16] M. A. Erturk et al., "Toward imaging the body at 10.5 tesla," *Magn Reson Med,* vol. 77, no. 1, pp. 434-443, Jan, 2017.

[17] M. A. Ertürk et al., "A 16-channel combined loop-dipole transceiver array for 7 tesla body MRI," *Magn Reson Med,* vol. 77, no. 2, pp. 884-894, 2017.

[18] D. Wenz, and R. Gruetter, “Dielectric Resonators and Dipole Antennas Combined: New Approach in Radio Frequency Coil Design for Ultrahigh Field MRI,” in Proc. 29th Annu. Meeting. ISMRM, Virtual meeting, 2020, pp. 28.

[19] M. K. Woo et al., “A 16-channel transceiver loop+ dipole antennas head array for human head imaging at 10.5 T,” in IEEE-ICEAA, 2017 pp. 1649-1652.

[20] N. I. Avdievich et al., “Evaluation of transmit efficiency and SAR for a tight fit transceiver human head phased array at 9.4 T,” *NMR Biomed,* vol. 30, no. 2, pp. e3680, Feb, 2017.

[21] G. Shajan, M. Kozlov, J. Hoffmann, R. Turner, K. Scheffler, and R. Pohmann, “A 16-channel dual-row transmit array in combination with a 31-element receive array for human brain imaging at 9.4 T,” *Magn Reson Med,* vol. 71, no. 2, pp. 870-879, 2014.

[22] G. Adriany et al., “Transmit and receive transmission line arrays for 7 Tesla parallel imaging,” *Magn Reson Med,* vol. 53, no. 2, pp. 434-45, Feb, 2005.

[23] G. Adriany et al., “A 32-channel lattice transmission line array for parallel transmit and receive MRI at 7 tesla,” *Magn Reson Med,* vol. 63, no. 6, pp. 1478-1485, 2010.

[24] G. Adriany et al., “A geometrically adjustable 16-channel transmit/receive transmission line array for improved RF efficiency and parallel imaging performance at 7 Tesla,” *Magn Reson Med,* vol. 59, no. 3, pp. 590-597, 2008.

[25] J. Clément, R. Gruetter, and Ö. Ipek, “A combined 32-channel receive-loops/8-channel transmit-dipoles coil array for whole-brain MR imaging at 7T,” *Magn Reson Med,* vol. 82, no. 3, pp. 1229-1241, 2019.

[26] J. D. Clément, R. Gruetter, and Ö. Ipek, “A human cerebral and cerebellar 8-channel transceive RF dipole coil array at 7T,” *Magn Reson Med,* vol. 81, no. 2, pp. 1447-1458, 2019.

[27] I. R. Connell, and R. S. Menon, “Shape Optimization of an Electric Dipole Array for 7 Tesla Neuroimaging,” *IEEE Trans Med Imaging,* vol. 38, no. 9, pp. 2177-2187, Sep, 2019.

[28] A. C. Mak, C. R. Rowell, and R. D. Murch, “Isolation enhancement between two closely packed antennas,” *IEEE Trans Antennas and Propagation,* vol. 56, no. 11, pp. 3411-3419, 2008.

[29] R. F. Lee, R. O. Giaquinto, and C. J. Hardy, “Coupling and decoupling theory and its application to the MRI phased array,” *Magn Reson Med,* vol. 48, no. 1, pp. 203-13, Jul, 2002.

[30] M. K. Woo et al., “Extended Monopole antenna Array with individual Shield (EMAS) coil: An improved monopole antenna design for brain imaging at 7 tesla MRI,” *Magn Reson Med,* vol. 75, no. 6, pp. 2566-72, Jun, 2016.

[31] D. Hill, and J. Wait, “Coupling between a Radiating Coaxial Cable and a Dipole Antenna,” *IEEE Trans Communications,* vol. 23, no. 11, pp. 1354-1357, 1975.

[32] L. Liu, S. Cheung, and Y. Weng, "Cable effects on measuring small planar UWB monopole antennas," *Ultra Wideband—Current Status and Future Trends*: InTech, 2012.

[33] J. R. Wait, and D. A. Hill, “Electromagnetic-Fields of a Dielectric Coated Coaxial Cable with an Interrupted Shield - Quasi-Static Approach,” *IEEE Trans Antennas and Propagation,* vol. 23, no. 5, pp. 679-682, 1975.

[34] D. M. Peterson, B. L. Beck, Duensing, C. R., Fitzsimmons, J. R., “Common mode signal rejection methods for MRI: Reduction of cable shield currents for high static magnetic field systems,” *Concept Magn Reson B,* vol. 19b, no. 1, pp. 1-8, Oct, 2003.

[35] D. A. Seeber, I. Jevtic, and A. Menon, “Floating shield current suppression trap,” *Concept Magn Reson B,* vol. 21b, no. 1, pp. 26-31, Apr, 2004.

[36] W. Kissick, WJ. Ingram, J. Vanderau, and R. Jennings, “Antenna System Guide NIJ Guide 202–00,” *NCJ,* vol. 20531, 2001.

[37] D. M. Pozar, *Microwave engineering*, p.^pp. 136, 111 River Street, Hoboken, NJ 07030, USA: John Wiley & Sons, 2009.
[38] W. L. Weeks, *Antenna engineering*: McGraw-Hill, 1968.
[39] R. King, "Asymmetrically Driven Antennas and the Sleeve Dipole," *Proceedings of the Institute of Radio Engineers,* vol. 38, no. 10, pp. 1154-1164, 1950.
[40] R. Lagore, L. DelaBarre, Tian, J, Adriany, G, Eryaman, Y, and J. Vaughan, "End-loaded dipole array for 10.5 T head imaging," in Proc. 24th Annu. Meeting ISMRM, Singapore, Singapore, 2016, pp. 2138.
[41] B. Beck, KA. Jenkins, J. Rocca, and J. Fitzsimmons, "Tissue-equivalent phantoms for high frequencies," *Concept Magn Reson B,* vol. 20, no. 1, pp. 30-33, 2004.
[42] A. J. Jesmanowicz, S. Hyde, W. Froncisz, and B. J. Kneeland, "Noise correlation," *Magn Reson Med,* vol. 20, no. 1, pp. 36-47, Jul, 1991.
[43] V. L. Yarnykh, "Actual flip-angle imaging in the pulsed steady state: a method for rapid three-dimensional mapping of the transmitted radiofrequency field," *Magn Reson Med,* vol. 57, no. 1, pp. 192-200, Jan, 2007.
[44] V. Hartwig et al., "B1+/actual flip angle and reception sensitivity mapping methods: simulation and comparison," *Magn Reson Med,* vol. 29, no. 5, pp. 717-722, 2011.
[45] C. M. Collins, and M. B. Smith, "Signal-to-noise ratio and absorbed power as functions of main magnetic field strength, and definition of "90°" RF pulse for the head in the birdcage coil," *Magn Reson Med,* vol. 45, no. 4, pp. 684-691, 2001.
[46] J. l Mispelter, M. Lupu, and A. Briguet, *NMR probeheads for biophysical and biomedical experiments: theoretical principles & practical guidelines*, p.^pp. 283: Imperial college press, 2006.
[47] A. Hirata, and O. Fujiwara, "The correlation between mass-averaged SAR and temperature elevation in the human head model exposed to RF near-fields from 1 to 6 GHz," *Physics in Medicine & Biology,* vol. 54, no. 23, pp. 7227, 2009.
[48] R. L. McIntosh, V. Anderson, and R. J. McKenzie, "The use of temperature as a metric for the assessment of RF safety," *Radiation Protection in Australasia, vol. 25, pp. 9-21, Nov 27-29 2008.*, 2008.
[49] A. Razmadze, L. Shoshiashvili, D. Kakulia, R. Zaridze, G. Bit-Babik, and A. Faraone, "Influence of specific absorption rate averaging schemes on correlation between mass-averaged specific absorption rate and temperature rise," *Electromagnetics,* vol. 29, no. 1, pp. 77-90, 2009.
[50] I. Zivkovic, C. A. de Castro, and A. Webb, "Design and characterization of an eight-element passively fed meander-dipole array with improved specific absorption rate efficiency for 7 T body imaging," *NMR Biomed,* vol. 32, no. 8, pp. e4106, 2019.
[51] B. Steensma et al., "Introduction of the snake antenna array: Geometry optimization of a sinusoidal dipole antenna for 10.5 T body imaging with lower peak SAR," *Magn Reson Med*, 2020.
[52] E. A. Barberi, J. S. Gati, B. K. Rutt, and R. S. Menon, "A transmit-only/receive-only (TORO) RF system for high-field MRI/MRS applications," *Magn Reson Med,* vol. 43, no. 2, pp. 284-289, 2000.

Chapter 7

Summary and General discussions

7.1 Summary

7.2 General discussions

7.1 Summary

Most MRI applications benefit from the inherent SNR advantages of ultra-high field (UHF (>300MHz proton operating frequency) MR systems for human imaging. However, an increased field strength results in substantial non-uniformity in the B_1 fields. Arrays consisting of transmit antennas have the ability to mitigate inhomogeneity through an optimal combination of phase/ amplitude and RF excitation waveform. Such arrays are essentially required for achieving an acceptable B_1^+ field homogeneity and optimized transmit efficiency. At ultra-high fields, multi-element transmit arrays with independent channels are essential for achieving acceptable B_1 field homogeneity and to optimize transmit efficiency. As a transmitter, 16-channel dipole head arrays is desirable above 7 T, however, it is difficult to achieve this high channel count due to coupling. In this study, we demonstrate that the newly designed human head array is capable of overcoming this non-uniformity.

The loop + dipole concept discussed by chapter 2 is one of the alternative methods for a 16-channel array for the human head. The possibility that the spacing between antenna and sample can be adjusted is advantageous for dipoles and loops for consistent tuning and matching as well as better coupling to the sample and reduced radiation. However, if the antennas are spaced to closely, they may couple with each other. However, with increased operating frequency, dipole antenna element spacing is expected to become less challenging compared to lower frequencies due to an increased coupling to the load and narrower sensitivity profiles.

Loop + dipole antennas arrays can potentially benefit from this ultra-high field effect - which results in tighter spacing and the ability to utilize more array elements without the need for decoupling circuitry. This has been shown previously for body applications where a heavily loaded dipole antenna allowed tighter element spacing without the need for decoupling circuitry. For the tight fitting loop + dipole arrays, we observed a similarly improved decoupling performance.

Compared with an 8-channel loop-only array or an 8-channel dipole antenna array, a 16-channel loop + dipole antenna array at 10.5 T allows for tight spacing that is independent of the decoupling circuitry but additionally provides higher B_1^+ transmit efficiency and improves the ratio of B_1^+ per peak 10 g SAR. Our data confirms that a 16-channel loop + dipole antenna array has advantages compared to an 8-channel loop array and dipole only antenna array.

Loop array coils (e.g., more than eight channels) have been demonstrated to provide a high SNR with a decent spatial coverage. However, a large B_1 non-uniformity due to the short wavelength at 7 T continues to exist and induces significant signal variations in both the transmit and receive B_1 fields. Under loaded conditions, the dipole shows more symmetric excitation because of the coherent current source. And the conductivity and the permittivity in the sample result the inhomogeneous B_1^+ pattern of loop. However, the

loop + dipole combination, in which loops and dipoles are located geometrically, shows better performance than the individual loop and the dipole. Dipole elements combined with loop elements in particular configurations are predicted to yield optimal coil performance.

The other approach for the 16-channel array is the Mono-Dipole array concept discussed in chapter 4. Improved decoupling among the channels was observed in the Mono-Dipole arrays. For head applications, it is difficult to achieve sufficient dipole decoupling because the dipoles couple to a lesser extent to tissue. In addition, shortening the length of the dipole is required for the human head applications. To connect one pole of each dipole, we effectively created a radial ground plane resulting in a 16-channel Mono-Dipole array. Improved decoupling among the channels was observed in the Mono-Dipole arrays. We observed that 16-channel Mono-Dipole head antenna arrays have potential advantages for whole head cover at 10.5 T. In addition, for the 16-channel Mono-Dipole array, the phase shimming between elements is required for the optimized results.

At chapter 6, a Sleeve antenna array was the latest research topic of this article. A dipole antenna which is a kind of a radiative antenna, has the advantage of providing a uniform B_1^+ field. However, the dipole antenna shows high coupling between the elements and it limits the number of the elements for the multi-channel array. A sleeve antenna array was developed to extend the number of elements.

The RF coil was adapted for the sleeve monopole antenna concept for use as a novel MRI antenna array and was used to successfully construct a high density 16-channel sleeve monopole antenna array for use at 10.5 T. This 16-channel sleeve monopole antenna array showed higher $B_1^+ /\sqrt{}$peak 10 g SAR values compared to both 16-channel dipole and 16-channel sleeve monopole antenna arrays.

7.2 General discussions

The impact that the progress in imaging techniques has had on the diagnosis and subsequent treatment of many life-threatening diseases is remarkable. There is, however, still considerable room for improvement in technological innovations as well as their dissemination across the global community. Coupling hinders the development of high density radiative antenna arrays for UHF imaging. As the frequency increased higher, spacing becomes more challenging compared to low frequencies. However, the loop + dipole array proposed in chapter 2 can achieve better spacing without further decoupling. Good decoupling was consistently observed, as indicated by the data.

The structure of the sleeve antenna itself closely resembles the dipole antenna structure, but with one important difference: the sleeve antenna array has a side-fed structure while the dipole has a center-fed structure. In other words, the structure of a sleeve antenna array does not require parallel alignments of antennas and coaxial cables in the same plane unlike the dipole antenna array. Therefore, the interaction between the antenna and coaxial cable can be eliminated. Moreover, the floating cable traps of a sleeve antenna array acts to suppress imbalanced RF current leaking onto the outer surface of the shield of the coaxial feed line. These floating cable traps did not negatively influence either the antenna efficiency nor radiation pattern.

We attribute the reduced interference between the elements to the routing of the feed cable for the sleeve antenna array. Furthermore, the asymmetric structure of the sleeve antenna causes a change in current distribution and radiation pattern. The current distribution of this asymmetric structure results in reduced magnetic coupling between elements.

The feed point of an antenna has a high current flow and generally produces strong E-fields in the imaging sample. Due to being side-fed, however, the E-fields are more spread out around the feed point of the sleeve antenna. This is observed in the sagittal and coronal 10g SAR maps of the sleeve antenna array. Consequently, the sleeve antenna array has an increased region of 10g SAR towards the feed point, however, this spread out 10g SAR distribution leads to lower peak 10 g SAR values compared to the dipole antenna array. The peak 10 g SAR value of the sleeve antenna array was substantially lower than that for the dipole antenna array. Lower SAR is a very important advantage of the sleeve antenna array described herein compared to dipole arrays. This reduced SAR leads to a higher SAR efficiency of the sleeve antenna array over the ROI compared to the dipole antenna array.

In summary, the main advantage of the sleeve antenna array is that coupling between neighboring elements is reduced significantly compared to a dipole array. With the same spacing between adjacent antennas, the sleeve antenna array shows a significantly lower noise correlation compared to the dipole antenna array. Thus, sleeve antenna concepts can support tighter element spacing and potentially can allow an increased density of

antenna elements in an array. The 16 channel sleeve array presented here is the initial step towards possible higher channel arrays such as more than 32 elements. The other advantage of the sleeve antenna array is a substantially lower SAR and enhanced SAR efficiency.

As a result, sleeve antenna concepts have some potential to be closer to ‘optimal’ RF transmission performance for a given number of channels for 10.5 T human brain imaging. For future in-vivo human brain imaging, the coil will need to be further optimized regarding the number of channels and the length of individual antennas.

Chapter 8

Publications and awards

Publications

- Byeong-Yeul Lee, Xiao-Hong Zhu, **Myung Kyun Woo**, Gregor Adriany, Scott Schillak, Wei Chen, "Interleaved 31P MRS imaging of human frontal and occipital lobes using dual RF coils in combination with single-channel transmitter–receiver and dynamic B0 shimming" NMR in Biomedicine 31:e3842, 2018

- Jeong-Hee Kim, Jong-Hoon Kim, Young-Don Son , Yo-Han Joo, Sang-Yoon Lee, Hang-Keun Kim, **Myung-Kyun Woo**, "Altered interregional correlations between serotonin transporter availability and cerebral glucose metabolism in schizophrenia: A high-resolution PET study using [11C]DASB and [18F]FDG" Schizohrenia Research 182 (2017) 55-65

- **Myung-Kyun Woo**, Suk-Min Hong, Jongho Lee, Chang-Ki Kang, Sung-Yeon Park, Young-Don Son, Young-Bo Kim, Zang-Hee Cho, "Extended Monopole Antenna Array with Individual Shield (EMAS) – An Improved Monopole Antenna Design for Brain Imaging at 7T MRI", Magn Reson Med 75:2566–2572, 2016

- Randall B. Stafford, **Myung-Kyun Woo**†, Se-Hong Oh, Tiejun Zhao, Young-Bo Kim, John A. Detre, Zang-Hee Cho, Jongho Lee, "An Actively Decoupled Dual Transceiver Coil System for Continuous ASL at 7 T" Int J Imaging Syst Technol. 26(2): 106–115, 2016

- Chang-Ki Kang, **Myung-Kyun Woo**, Suk-Min Hong, Young-Bo Kim, Zang-Hee Cho, "Intracranial micro vascular imaging at 7T MRI with transceiver RF coils" Magn Reson Imaging 32:1133-1138,2014

- Suk-Min Hong, Joshua Haekyun Park, **Myung-Kyun Woo**, Young-Bo Kim, Zang-Hee Cho, "New Design Concept of Monopole Antenna Array for UHF 7T MRI" Magn Reson Med 71:1944-1952, 2014

Conference paper

- **Myung Kyun Woo**, Russell L Lagore, Lance DelaBarre, Byeong-Yeul Lee, Yigitcan Eryaman, Jerahmie Radder, Arcan Erturk, Gregory Metzger, Pierre- Francois van de Moortele, Kamil Ugurbil, Gregor Adriany, "A 16 channel transceiver loop-dipole head array for human head imaging at 10.5T". 2017 International Conference on Electromagnetics in Advanced Applications (ICEAA), 10.1109/ICEAA.2017.8065607

- Jerahmie Radder, **Myung-Kyun Woo**, Pierre-Francois Van de Moortele, Greg Metzger, Arcan Ertürk, John Strupp, Kamil Ugurbil, Gregor Adriany, "Optimization and Simulation of a 16-Channel Loop and Dipole Array for Head MRI Applications at 10.5 Tesla." 2017 International Conference on Electromagnetics in Advanced Applications (ICEAA), 10.1109/ICEAA.2017.8065655

Awards (Magna cum laude)

- **Myung Kyun Woo** , Lance DelaBarre , Russell Lagore , Steve Jungst, Kamil Ugurbil , and Gregor Adriany, "Evaluation of a sleeve monopole antenna array, a novel 16-channel radiative antenna array at 10.5T", 27th ISMRM meeting, Montreal, Canada, 13-17 May, 2019. [Power pitch #7652]

- **Myung Kyun Woo** , Lance DelaBarre , Jerahmie Radder , Russell Lagore , Yigitcan Eryaman , Kamil Ugurbil , and Gregor Adriany, "Comparison of a 16-channel monopole/dipole hybrid array with a combined 8-channel monopole + 8-channel high dielectric constant (HDC) disk dipole array for head imaging at 10.5T", 26th ISMRM meeting, Paris, France, 16-21 June, 2018. [Power pitch #0024]

Chapter 9

Acknowledgements

This work is the result of more than 4 years of research at the Center for Magnetic Resonance and Research (CMRR) and the University of Minnesota with contributions of all members of the lab. I am much obligated that I had the occasion to work in such an inspiring atmosphere and to enjoy the great sprit with this institute. I want to address my special thanks to:

Dr. Kamil Ugurbil gave me the opportunity to work in his group thoroughly revising manuscripts that came up, and I especially appreciate his future-oriented insights and trustful guidance which are keys to productive and creative atmosphere in the group.

Dr. Gregor Adriany guided me into radio frequency electronics, hardware and engineering in MRI. I gladly appreciate many interesting and also diverting discussions. He is always the greatest supporter one can rely on getting something working.

Dr. Lance Delabarre helped me with highly skillful MR data processing and many interesting discussions. Special thanks for taking a lot of time to run the scanner and evaluate experimental results with me.

Dr. Russell Luke Lagore discussed the results for the reliable approach with me. His knowledge and help with field theoretical questions were the key to discoveries and developments made.

Steve Jungst helped me get the work done on the 3D drawings and designs for RF coils and on MR related supplementary equipment. His skillful drawings made it possible to do the experiments smoothly.

Matt Wacks shared his great experience in MR hardware and electronics. Also, he contributed to the enjoyable atmosphere in the group.

Dr. Greg Metzger shared many interesting discussions about MRI and other related topics on the body imaging. His wit always changed the atmosphere in the group meeting.

Dr. Xiaoping Wu helped to achieve wonderful images with his amazing B_1 shimming techniques with Spoke pulse.

Dr. Yigitcan Eryaman shared his great experience regards to the safety he collected over the years. His guidance helped to find right way when I was lost in finding the solution.

Dr. Andrea Grant shared her great experience in in-vivo work and clinical applications. She also taught me how to approach the system.

Jerahmie Radder helped me do the simulations which provided me the insight into the complex computational fields. He helped to solve any problems with programming and simulation related to MRI.

Jeromy Thotland helped me in 3D printing with his insightful drawing skills. And he always took care of me with warm-hearted languages.

Dr. Pierre-Francois van de Moortele guided me with unbiased and interesting discussions with wonderful B_1 shimming technique. His tool approached to obtain all of processes easy and fast.

Dr. Edward Auerbach solved entire problems occurring from the MR system which allowed me to work under the environment with all of the systems working properly.

Sean Moen provided me nice circumstances for data collection. He always created fun and exciting atmosphere.

Chapter 10

Curriculum vitae

I was born on November 9th, 1983 as the son of Tae Hyung Woo and In Sook Han in Seoul, Republic of Korea. I have a bachelor's degree in Material Science and Engineering at the Korea University in Seoul, Republic of Korea. My scientific career started from the Neuroscience Research Institute (NRI) supervised by Dr. Zang-Hee Cho in Incheon, Republic of Korea. I adapted an opportunity to work at the NRI to focus on developing/improving brain research with radiofrequency (RF) coil. Upon earning my master's degree in Medical Science at the Gachon University in 2011, I continued to stay as a researcher at the NRI until August of 2014. After, I worked in RF coil part in the Laboratory for Imaging Science and Technology team supervised by Dr. Jongho Lee (Department of Electrical and Computer Engineering) at the Seoul National University in Seoul, Republic of Korea until November 2015. In March 2016, I joined the Center for Magnetic Resonance Research (CMRR) as a research assistant in Minnseota, USA. Dr. Kamil Ugurbil provided me the opportunity to work at his group, and Dr. Gregor Adriany guided me to improve my skills for RF coil at 10.5T MRI, which is one the highest human whole body systems in the world. I achieved the master's degree in Medical Physics at the University of Minnesota supervised by Dr. Kamil Ugurbil in Minnesota, USA. I received my doctorate diploma in Medical Physics from the University of Minnesota in 2020.

Chapter 11

References

1 Duyn, J. H. *et al.* High-field MRI of brain cortical substructure based on signal phase. *Proceedings of the National Academy of Sciences* **104**, 11796-11801 (2007).

2 Guérin, B. *et al.* The ultimate signal-to-noise ratio in realistic body models. *Magnetic resonance in medicine* **78**, 1969-1980 (2017).

3 Lattanzi, R. *et al.* Approaching ultimate intrinsic signal-to-noise ratio with loop and dipole antennas. *Magnetic resonance in medicine* **79**, 1789-1803 (2018).

4 Pohmann, R., Speck, O. & Scheffler, K. Signal-to-noise ratio and MR tissue parameters in human brain imaging at 3, 7, and 9.4 tesla using current receive coil arrays. *Magn Reson Med* **75**, 801-809 (2016).

5 Uğurbil, K. Magnetic resonance imaging at ultrahigh fields. *IEEE Trans Biomed Eng* **61**, 1364-1379 (2014).

6 Uğurbil, K. Imaging at ultrahigh magnetic fields: History, challenges, and solutions. *Neuroimage* **168**, 7-32 (2018).

7 Wiesinger, F. *et al.* Parallel imaging performance as a function of field strength—an experimental investigation using electrodynamic scaling. *Magnetic Resonance in Medicine: An Official Journal of the International Society for Magnetic Resonance in Medicine* **52**, 953-964 (2004).

8 Vaughan, J. T. *et al.* 7T vs. 4T: RF power, homogeneity, and signal-to-noise comparison in head images. *Magnetic Resonance in Medicine: An Official Journal of the International Society for Magnetic Resonance in Medicine* **46**, 24-30 (2001).

9 Yang, Q. X. *et al.* Analysis of wave behavior in lossy dielectric samples at high field. *Magnetic Resonance in Medicine: An Official Journal of the International Society for Magnetic Resonance in Medicine* **47**, 982-989 (2002).

10 Kang, C.-K., Kim, H.-K., Son, Y.-D., Yeong-Bae, L. & Woo, M.-K. (Google Patents, 2019).

11 Raaijmakers, A. *et al.* Design of a radiative surface coil array element at 7 T: the single-side adapted dipole antenna. *Magnetic resonance in medicine* **66**, 1488-1497 (2011).

12 Wiggins, G. C., Zhang, B., Lattanzi, R., Chen, G. & Sodickson, D. in *Proceedings of the 20th Annual Meeting of ISMRM, Melbourne, Australia.* 541.

13 Woo et al., M. K. Extended monopole antenna array with individual shield (EMAS) coil: An improved monopole antenna design for brain imaging at 7 tesla MRI. *Magn Reson Med* **75**, 2566-2572 (2016).

14 Ertürk, M. A., Raaijmakers, A. J., Adriany, G., Uğurbil, K. & Metzger, G. J. A 16-channel combined loop-dipole transceiver array for 7 T esla body MRI. *Magnetic resonance in medicine* **77**, 884-894 (2017).

15 Woo, M. K. *et al.* in *2017 International Conference on Electromagnetics in Advanced Applications (Iceaa).* 1649-1652 (IEEE).

16 Adriany, G. *et al.* A 32-channel lattice transmission line array for parallel transmit and receive MRI at 7 tesla. *Magnetic Resonance in Medicine: An Official Journal of the International Society for Magnetic Resonance in Medicine* **63**, 1478-1485 (2010).

17 Adriany, G. *et al.* Transmit and receive transmission line arrays for 7 Tesla parallel imaging. *Magnetic Resonance in Medicine: An Official Journal of the International Society for Magnetic Resonance in Medicine* **53**, 434-445 (2005).
18 Avdievich, N. *et al.* Evaluation of transmit efficiency and SAR for a tight fit transceiver human head phased array at 9.4 T. *NMR in Biomedicine* **30**, e3680 (2017).
19 Connell, I. R. & Menon, R. S. Shape Optimization of an Electric Dipole Array for 7 Tesla Neuroimaging. *IEEE transactions on medical imaging* **38**, 2177-2187 (2019).
20 Lee, R. F., Giaquinto, R. O. & Hardy, C. J. Coupling and decoupling theory and its application to the MRI phased array. *Magnetic Resonance in Medicine: An Official Journal of the International Society for Magnetic Resonance in Medicine* **48**, 203-213 (2002).
21 Hill, D. & Wait, J. Coupling between a radiating coaxial cable and a dipole antenna. *IEEE Transactions on Communications* **23**, 1354-1357 (1975).
22 Wait, J. & Hill, D. Electromagnetic fields of a dielectric coated coaxial cable with an interrupted shield--Quasi-static approach. *IEEE Transactions on Antennas and Propagation* **23**, 679-682 (1975).
23 Yang, X., Zheng, T. & Fujita, H. in *ISMRM Fourteenth Scientific Meeting Weekend Syllabus.*
24 Bloch, F. Nuclear induction. *Physical review* **70**, 460 (1946).
25 Purcell, E. M., Torrey, H. C. & Pound, R. V. Resonance absorption by nuclear magnetic moments in a solid. *Physical review* **69**, 37 (1946).
26 Lauterbur, P. C. Image formation by induced local interactions: examples employing nuclear magnetic resonance. *nature* **242**, 190-191 (1973).
27 Lauterbur, P. G. & Lai, C.-M. Zeugmatography by reconstruction from projections. *IEEE Transactions on Nuclear Science* **27**, 1227-1231 (1980).
28 Ernst, R. R. & Anderson, W. A. Application of Fourier transform spectroscopy to magnetic resonance. *Review of Scientific Instruments* **37**, 93-102 (1966).
29 Ernst, R. R., Bodenhausen, G. & Wokaun, A. *Principles of nuclear magnetic resonance in one and two dimensions*. Vol. 14 (Clarendon press Oxford, 1987).
30 Kang, C.-K., Woo, M.-K., Hong, S.-M., Kim, Y.-B. & Cho, Z.-H. Intracranial microvascular imaging at 7 T MRI with transceiver RF coils. *Magnetic resonance imaging* **32**, 1133-1138 (2014).
31 Barberi, E. A., Gati, J. S., Rutt, B. K. & Menon, R. S. A transmit-only/receive-only (TORO) RF system for high-field MRI/MRS applications. *Magnetic Resonance in Medicine: An Official Journal of the International Society for Magnetic Resonance in Medicine* **43**, 284-289 (2000).
32 Roemer, P. B., Edelstein, W. A., Hayes, C. E., Souza, S. P. & Mueller, O. M. The NMR phased array. *Magnetic resonance in medicine* **16**, 192-225 (1990).
33 l Mispelter, J., Lupu, M. & Briguet, A. *NMR probeheads for biophysical and biomedical experiments: theoretical principles & practical guidelines*. (Imperial college press, 2006).
34 Haines, K., Neuberger, T., Lanagan, M., Semouchkina, E. & Webb, A. High Q calcium titanate cylindrical dielectric resonators for magnetic resonance microimaging. *Journal of Magnetic Resonance* **200**, 349-353 (2009).
35 Webb, A. Dielectric materials in magnetic resonance. *Concepts in magnetic resonance part A* **38**, 148-184 (2011).
36 Yang, Q. X. *et al.* Manipulation of image intensity distribution at 7.0 T: passive RF shimming and focusing with dielectric materials. *Journal of Magnetic Resonance*

Imaging: An Official Journal of the International Society for Magnetic Resonance in Medicine **24**, 197-202 (2006).

37 Bandettini, P. A., Bowtell, R., P. Jezzard & Turner, R. Ultrahigh field systems and applications at 7 T and beyond: Progress, pitfalls, and potential. *Magn Reson Med* **67**, 317-321, doi:10.1002/mrm.23151 (2012).

38 Vaughan et al., T. Whole-body imaging at 7T: preliminary results. *Magn Reson Med* **61**, 244-248 (2009).

39 Vaughan et al., T. 9.4T human MRI: preliminary results. *Magn Reson Med* **56**, 1274-1282, doi:10.1002/mrm.21073 (2006).

40 Kang, C., MK. Woo, SM. Hong, YB. Kim, and ZH. Cho. Intracranial microvascular imaging at 7 T MRI with transceiver RF coils. *Magn Reson Imag* **32**, 1133-1138 (2014).

41 Koopmans, P. J., M. Barth, S. Orzada, & D. G. Norris. Multi-echo fMRI of the cortical laminae in humans at 7 T. *Neuroimage* **56**, 1276-1285, doi:10.1016/j.neuroimage.2011.02.042 (2011).

42 Moser, E., Stahlberg, F., M. E. Ladd, & Trattnig, S. 7-T MR—from research to clinical applications? *NMR Biomed* **25**, 695-716 (2012).

43 Cao, Z., Park, J., ZH. Cho, & Collins, C. M. Numerical evaluation of image homogeneity, signal-to-noise ratio, and specific absorption rate for human brain imaging at 1.5, 3, 7, 10.5, and 14T in an 8-channel transmit/receive array. *J Magn Reson Med* **41**, 1432-1439 (2015).

44 Erturk et al., M. A. Toward imaging the body at 10.5 tesla. *Magn Reson Med* **77**, 434-443, doi:10.1002/mrm.26487 (2017).

45 Vaughan et al., J. T. 7T vs. 4T: RF power, homogeneity, and signal-to-noise comparison in head images. *Magn Reson Med* **46**, 24-30 (2001).

46 Ogawa et al., S. Functional brain mapping by blood oxygenation level-dependent contrast magnetic resonance imaging. A comparison of signal characteristics with a biophysical model. *Biophysical journal* **64**, 803-812 (1993).

47 He et al., X. First in-vivo human imaging at 10.5 T: Imaging the body at 447 MHz. *Magn Reson Med* (2019).

48 Sadeghi-Tarakameh et al., A. In vivo human head MRI at 10.5 T: A radiofrequency safety study and preliminary imaging results. *Magn Reson Med* **84**, 484-496 (2020).

49 Ertürk, M. A., A. JE. Raaijmakers, G. Adriany, K. Uğurbil, and G. J. Metzger,. A 16-channel combined loop-dipole transceiver array for 7 T esla body MRI. *Magn Reson Med* **77**, 884-894 (2017).

50 Metzger, G. J., C. Snyder, C. Akgun, T. Vaughan, K. Ugurbil, and PF. Van de Moortele. Local B1+ shimming for prostate imaging with transceiver arrays at 7T based on subject-dependent transmit phase measurements. *Magn Reson Med* **59**, 396-409 (2008).

51 Avdievich et al., N. I. Evaluation of transmit efficiency and SAR for a tight fit transceiver human head phased array at 9.4 T. *Nmr in Biomedicine* **30**, e3680, doi:ARTN e3680 10.1002/nbm.3680 (2017).

52 Shajan, G., M. Kozlov, J. Hoffmann, R. Turner, K. Scheffler, and R. Pohmann. A 16-channel dual-row transmit array in combination with a 31-element receive array for human brain imaging at 9.4 T. *Magn Reson Med* **71**, 870-879 (2014).

53 Adriany et al., G. A 32-channel lattice transmission line array for parallel transmit and receive MRI at 7 tesla. *Magn Reson Med* **63**, 1478-1485 (2010).

54 Adriany et al., G. Transmit and receive transmission line arrays for 7 Tesla parallel imaging. *Magn Reson Med* **53**, 434-445, doi:10.1002/mrm.20321 (2005).

55 Raaijmakers et al., A. Design of a radiative surface coil array element at 7 T: the single-side adapted dipole antenna. *Magn Reson Med* **66**, 1488-1497 (2011).
56 Hong, S. M., J. H. Park, M. K. Woo, Y. B. Kim, and Z. H. Cho. New design concept of monopole antenna array for UHF 7T MRI. *Magn Reson Med* **71**, 1944-1952, doi:10.1002/mrm.24844 (2014).
57 Kang, C.-K., H.-K. Kim, Y.-D. Son, Yeong-Bae, L. & Woo, M.-K. in *U.S. Patent No. 10,488,474. 26 Nov. 2019* (2019).
58 Oezerdem et al., C. 16-channel bow tie antenna transceiver array for cardiac MR at 7.0 tesla. *Magn Reson Med* **75**, 2553-2565 (2016).
59 Lattanzi, R., G. C. Wiggins, B. Zhang, Q. Duan, R. Brown, and D. K. Sodickson. Approaching ultimate intrinsic signal-to-noise ratio with loop and dipole antennas. *Magn Reson Med* **79**, 1789-1803, doi:10.1002/mrm.26803 (2018).
60 Pfrommer, A. & Henning, A. The ultimate intrinsic signal-to-noise ratio of loop-and dipole-like current patterns in a realistic human head model. *Magn Reson Med* **80**, 2122-2138 (2018).
61 Clément, J. D., Gruetter, R. & Ipek, Ö. A human cerebral and cerebellar 8-channel transceive RF dipole coil array at 7T. *Magnetic resonance in medicine* **81**, 1447-1458 (2019).
62 Wiggins, G. C., Zhang, B., Lattanzi, R., Chen, G. & Sodickson, D. The electric dipole array: an attempt to match the ideal current pattern for central SNR at 7 Tesla. *Proceedings of the 20th scientific meeting, International Society for Magnetic Resonance in Medicine, Melbourne, Australia* **541** (2012).
63 Eryaman et al., Y. SAR reduction in 7T C-spine imaging using a “dark modes” transmit array strategy. *Magn Reson Med* **73**, 1533-1539 (2015).
64 Raaijmakers et al., A. J. The fractionated dipole antenna: A new antenna for body imaging at 7 T esla. *Magn Reson Med* **75**, 1366-1374 (2016).
65 Brink, W. M., Wu, Z. & Webb, A. G. A simple head-sized phantom for realistic static and radiofrequency characterization at high fields. *Magn Reson Med* **80**, 1738-1745 (2018).
66 Jesmanowicz, A. J., S. Hyde, W. Froncisz, and B. J. Kneeland. Noise correlation. *Magn Reson Med* **20**, 36-47, doi:10.1002/mrm.1910200105 (1991).
67 Yarnykh, V. L. Actual flip-angle imaging in the pulsed steady state: a method for rapid three-dimensional mapping of the transmitted radiofrequency field. *Magn Reson Med* **57**, 192-200 (2007).
68 Collins, C. M. & Smith, M. B. Signal-to-noise ratio and absorbed power as functions of main magnetic field strength, and definition of “90°” RF pulse for the head in the birdcage coil. *Magnetic Resonance in Medicine: An Official Journal of the International Society for Magnetic Resonance in Medicine* **45**, 684-691 (2001).
69 Collins, C. M. & Smith, M. B. Calculations of B1 distribution, SNR, and SAR for a surface coil adjacent to an anatomically-accurate human body model. *Magn Reson Med* **45**, 692-699 (2001).
70 Kellman, P. & McVeigh, E. R. Image reconstruction in SNR units: a general method for SNR measurement. *Magn Reson Med* **54**, 1439-1447 (2005).
71 Woo et al., M. K. in *IEEE-ICEAA* 1649-1652 (IEEE ICEAA, 2017).
72 Christ et al., A. The Virtual Family—development of surface-based anatomical models of two adults and two children for dosimetric simulations. *Physics in Medicine & Biology* **55**, N23 (2009).
73 Corea et al., J. R. Screen-printed flexible MRI receive coils. *Nature communications* **7**, 1-7 (2016).

74 Guérin et al., B. The ultimate signal-to-noise ratio in realistic body models. *Magn Reson Med* **78**, 1969-1980 (2017).
75 Ugurbil, K. Magnetic resonance imaging at ultrahigh fields. *IEEE Trans Biomed Eng* **61**, 1364-1379, doi:10.1109/TBME.2014.2313619 (2014).
76 Ugurbil, K. Imaging at ultrahigh magnetic fields: History, challenges, and solutions. *Neuroimage* **168**, 7-32, doi:10.1016/j.neuroimage.2017.07.007 (2018).
77 Vaughan et al. , J. T. 7T vs. 4T: RF power, homogeneity, and signal-to-noise comparison in head images. *Magn Reson Med* **46**, 24-30, doi:10.1002/mrm.1156 (2001).
78 Duyn, J. H., P. van Gelderen, T. Q. Li, J. A. de Zwart, A. P. Koretsky, and M. Fukunaga. High-field MRI of brain cortical substructure based on signal phase. *Proc Natl Acad Sci U S A* **104**, 11796-11801, doi:10.1073/pnas.0610821104 (2007).
79 Lee et al., J. H. High contrast and fast three-dimensional magnetic resonance imaging at high fields. *Magn Reson Med* **34**, 308-312 (1995).
80 He et al., X. First in-vivo human imaging at 10.5 T: Imaging the body at 447 MHz. *Magn Reson Med* **DOI: 10.1002/mrm.28131** (2019).
81 Yang et al., Q. X. Analysis of wave behavior in lossy dielectric samples at high field. *Magn Reson Med* **47**, 982-989, doi:10.1002/mrm.10137 (2002).
82 Cao, Z., J. Park, Z. H. Cho, and C. M. Collins. Numerical evaluation of image homogeneity, signal-to-noise ratio, and specific absorption rate for human brain imaging at 1.5, 3, 7, 10.5, and 14T in an 8-channel transmit/receive array. *J Magn Reson Imaging* **41**, 1432-1439 (2015).
83 Van de Moortele et al., P. F. B1 destructive interferences and spatial phase patterns at 7 T with a head transceiver array coil. *Magn Reson Med* **54**, 1503-1518 (2005).
84 Wiesinger, F., P. F. Van de Moortele, G. Adriany, N. De Zanche, K. Ugurbil, and K. P. Pruessmann Parallel imaging performance as a function of field strength—an experimental investigation using electrodynamic scaling. *Magn Reson Med* **52**, 953-964 (2004).
85 Wiggins, G. C., B. Zhang, R. Lattanzi, G. Chen, and D. Sodickson. in *Proc. 20th Annu. Meeting ISMRM, Melbourne, Australia* Vol. 20 541 (2012).
86 Ertürk et al., M. A. A 16-channel combined loop-dipole transceiver array for 7 tesla body MRI. *Magn Reson Med* **77**, 884-894 (2017).
87 Wenz, D. & Gruetter, R. in *Proc. 29th Annu. Meeting. ISMRM* Vol. 4086 28 (Virtual meeting, 2020).
88 Avdievich et al., N. I. Evaluation of transmit efficiency and SAR for a tight fit transceiver human head phased array at 9.4 T. *NMR Biomed* **30**, e3680, doi:10.1002/nbm.3680 (2017).
89 Adriany et al., G. A geometrically adjustable 16-channel transmit/receive transmission line array for improved RF efficiency and parallel imaging performance at 7 Tesla. *Magn Reson Med* **59**, 590-597 (2008).
90 Clément, J., Gruetter, R. & Ipek, Ö. A combined 32-channel receive-loops/8-channel transmit-dipoles coil array for whole-brain MR imaging at 7T. *Magn Reson Med* **82**, 1229-1241 (2019).
91 Clément, J. D., Gruetter, R. & Ipek, Ö. A human cerebral and cerebellar 8-channel transceive RF dipole coil array at 7T. *Magn Reson Med* **81**, 1447-1458 (2019).
92 Connell, I. R. & Menon, R. S. Shape Optimization of an Electric Dipole Array for 7 Tesla Neuroimaging. *IEEE Trans Med Imaging* **38**, 2177-2187, doi:10.1109/TMI.2019.2906507 (2019).

93 Mak, A. C., Rowell, C. R. & Murch, R. D. Isolation enhancement between two closely packed antennas. *IEEE Trans Antennas and Propagation* **56**, 3411-3419 (2008).
94 Lee, R. F., Giaquinto, R. O. & Hardy, C. J. Coupling and decoupling theory and its application to the MRI phased array. *Magn Reson Med* **48**, 203-213, doi:10.1002/mrm.10186 (2002).
95 Woo et al., M. K. Extended Monopole antenna Array with individual Shield (EMAS) coil: An improved monopole antenna design for brain imaging at 7 tesla MRI. *Magn Reson Med* **75**, 2566-2572, doi:10.1002/mrm.25837 (2016).
96 Hill, D. & Wait, J. Coupling between a Radiating Coaxial Cable and a Dipole Antenna. *Ieee T Commun* **23**, 1354-1357, doi:Doi 10.1109/Tcom.1975.1092736 (1975).
97 Liu, L., Cheung, S. & Weng, Y. in *Ultra Wideband—Current Status and Future Trends* (InTech, 2012).
98 Wait, J. R. & Hill, D. A. Electromagnetic-Fields of a Dielectric Coated Coaxial Cable with an Interrupted Shield - Quasi-Static Approach. *IEEE Trans Antennas and Propagation* **23**, 679-682, doi:Doi 10.1109/Tap.1975.1141154 (1975).
99 Peterson, D. M., B. L. Beck, Duensing, C. R., Fitzsimmons, J. R. Common mode signal rejection methods for MRI: Reduction of cable shield currents for high static magnetic field systems. *Concept Magn Reson B* **19b**, 1-8, doi:10.1002/cmr.b.10090 (2003).
100 Seeber, D. A., Jevtic, I. & Menon, A. Floating shield current suppression trap. *Concept Magn Reson B* **21b**, 26-31, doi:10.1002/cmr.b.20008 (2004).
101 Kissick, W., WJ. Ingram, Vanderau, J. & Jennings, R. Antenna System Guide NIJ Guide 202–00. *NCJ* **20531** (2001).
102 Pozar, D. M. *Microwave engineering*. Vol. 4 136 (John Wiley & Sons, 2009).
103 Weeks, W. L. *Antenna engineering*. (McGraw-Hill, 1968).
104 King, R. Asymmetrically Driven Antennas and the Sleeve Dipole. *P Ire* **38**, 1154-1164, doi:Doi 10.1109/Jrproc.1950.233110 (1950).
105 Lagore, R., DelaBarre, L., Tian, J, Adriany, G, Eryaman, Y & Vaughan, J. in *Proc. 24th Annu. Meeting ISMRM, Singapore, Singapore* 2138 (2016).
106 Beck, B., KA. Jenkins, Rocca, J. & Fitzsimmons, J. Tissue-equivalent phantoms for high frequencies. *Concept Magn Reson B* **20**, 30-33 (2004).
107 Yarnykh, V. L. Actual flip-angle imaging in the pulsed steady state: a method for rapid three-dimensional mapping of the transmitted radiofrequency field. *Magn Reson Med* **57**, 192-200, doi:10.1002/mrm.21120 (2007).
108 Hartwig et al., V. B1+/actual flip angle and reception sensitivity mapping methods: simulation and comparison. *Magn Reson Med* **29**, 717-722 (2011).
109 Collins, C. M. & Smith, M. B. Signal-to-noise ratio and absorbed power as functions of main magnetic field strength, and definition of "90°" RF pulse for the head in the birdcage coil. *Magn Reson Med* **45**, 684-691 (2001).
110 Hirata, A. & Fujiwara, O. The correlation between mass-averaged SAR and temperature elevation in the human head model exposed to RF near-fields from 1 to 6 GHz. *Physics in Medicine & Biology* **54**, 7227 (2009).
111 McIntosh, R. L., Anderson, V. & McKenzie, R. J. The use of temperature as a metric for the assessment of RF safety. *Radiation Protection in Australasia, vol. 25, pp. 9-21, Nov 27-29 2008.* (2008).
112 Razmadze, A., L. Shoshiashvili, D. Kakulia, R. Zaridze, G. Bit-Babik, and A. Faraone. Influence of specific absorption rate averaging schemes on correlation between mass-averaged specific absorption rate and temperature rise. *Electromagnetics* **29**, 77-90 (2009).

113 Zivkovic, I., de Castro, C. A. & Webb, A. Design and characterization of an eight-element passively fed meander-dipole array with improved specific absorption rate efficiency for 7 T body imaging. *NMR Biomed* **32**, e4106 (2019).
114 Steensma et al., B. Introduction of the snake antenna array: Geometry optimization of a sinusoidal dipole antenna for 10.5 T body imaging with lower peak SAR. *Magn Reson Med* (2020).
115 Barberi, E. A., J. S. Gati, B. K. Rutt, and R. S. Menon. A transmit-only/receive-only (TORO) RF system for high-field MRI/MRS applications. *Magn Reson Med* **43**, 284-289 (2000).